MATERIALS MODIFICATION STRATEGIES TO IMPROVE PRASEODYMIUM- DOPED VISIBLE-TO-ULTRAVIOLET UPCONVERSION SYSTEMS FOR ENVIRONMENTAL APPLICATIONS

A Dissertation
Presented to
The Academic Faculty

By

Stephanie Lien Chinnapongse Cates

In Partial Fulfillment
Of the Requirements for the Degree
Doctor of Philosophy in Environmental Engineering

Georgia Institute of Technology

May, 2015

MATERIALS MODIFICATION STRATEGIES TO IMPROVE PRASEODYMIUM- DOPED VISIBLE-TO-ULTRAVIOLET UPCONVERSION SYSTEMS FOR ENVIRONMENTAL APPLICATIONS

Approved by:

Dr. Jaehong Kim, Advisor
School of Civil and Environmental Engineering
Georgia Institute of Technology
School of
School of Chemical and Environmental Engineering
Yale University

Dr. John Crittenden
School of Civil and Environmental Engineering
Georgia Institute of Technology

Dr. Angus Wilkinson
School of Chemistry and Biochemistry
Georgia Institute of Technology

Dr. Ching-Hua Huang
School of Civil and Environmental Engineering
Georgia Institute of Technology

Dr. Sotira Yiacoumi
School of Civil and Environmental Engineering
Georgia Institute of Technology

Date Approved: April 3rd, 2015

ACKNOWLEDGMENTS

I wish to thank my family, especially my parents, who have loved and supported me through everything. Thank you for raising two girls to believe that careers in science and engineering were worthy of dreaming about, and for providing the tools and encouragement to get us there. I would not be where I am today without your strength and prayers. You will always be my inspiration.

Thank you to my advisor, Jaehong Kim, who was not only an incredible mentor and teacher but also a caring and generous friend. Thank you for believing in this project and for always rooting for our success. Your guidance, patience, and sense of humor through it all have been such a blessing to me. I am so grateful to have had this opportunity.

Thank you to my Georgia Tech committee—Angus Wilkinson, Ching-Hua Huang, John Crittenden, and Sotira Yiacoumi—for the time you've invested in this project, and for your continued support even when we left Atlanta. It has been a pleasure sharing this work with you, and your insight has helped us to solve some of our most frustrating problems.

To my friends, lab mates, and all of the department staff at Georgia Tech, Yale, and Clemson, thank you for every favor, word of encouragement, and friendly gesture. I have so many wonderful memories and continue to be inspired by your hard work and kindness. A special thanks to Hyoung-Il, Chuanhao, Kyoung-Eun, and Min for your significant contributions to this project, and to my Pribes and Promers family at Georgia Tech, who made even the most daunting tasks enjoyable.

Finally, I wish to thank Ezra Cates, without whom this work would not have been possible. Thank you for laying the foundations for this project, and for your continued contributions even to this day. Thank you for the countless times you have helped me, challenged me, and lifted me up. And thank you for taking on the monumental task of being at once my colleague, mentor, friend, and husband. Watching you work gives me this amazing optimism about what lies ahead for this field. It has been such a privilege.

TABLE OF CONTENTS

LIST OF TABLES

LIST OF FIGURES

LIST OF SYMBOLS AND ABBREVIATIONS

AM1.5 – "Air mass 1.5", Optical path length 1.5 times vertical depth of Earth's atmosphere.

ATCC – American type culture collection

CB – Conduction band

CDC – U.S. Centers for Disease Control and Prevention

cfu – Colony-forming units

DPSS – Diode-pumped solid state (laser)

$\mathbf{E_{bg}}$ - Band gap energy

ESA – Excited state absorption

ETU – Energy transfer upconversion

FRET – Förster resonance energy transfer (FRET can also stand for fluorescence resonance energy transfer, another term for the same process)

HAADF – High-angle annular dark field (detector)

ICP-MS – Inductively coupled plasma mass spectroscopy

IR – Infrared radiation

$\mathbf{Ln^{3+}}$ –Lanthanide ion

NIR – Near infrared radiation

P25 – Commercial nano-sized TiO_2, mixture of anatase and rutile phases

PBS – Phosphate-buffered saline

PLS – Photoluminescence spectroscopy

PMT – Photomultiplier tube

POM – Polyoxometalate

ROS – Reactive oxygen species

SEM – Scanning electron microscopy

SODIS – Solar water disinfection

TEM – Transmission electron microscopy

TEOS – Tetraethoxysilane, a.k.a. tetraethyl orthosilicate

TSB – Tryptic soy broth

TTA – Triplet-triplet annihilation

UC – Upconversion

UCP – Upconversion phosphor

USP – Ultrasonic spray pyrolysis

UVA/UVB/UVC – Ultraviolet radiation subcategories

$\boldsymbol{V_O^{\cdot\cdot}}$ – Oxygen vacancy

VB – Valence band

VOC – Volatile organic compound

XRD – X-ray diffraction

SUMMARY

As the need for sustainable energy gains global recognition, there has been a growing demand for technologies that harness the power of the sun—a clean, affordable, and essentially inexhaustible source of energy. While photovoltaic solar panels, solar water heaters, or even sun-feeding algae reactors may come to mind, other materials can also utilize solar energy to perform useful processes. Among these are photocatalysts such as TiO_2, which can absorb UV to catalyze the degradation of organic pollutants. Another class of materials known as upconversion (UC) phosphors can be used to convert light from the sun to light of a higher energy; the potential to use these materials to convert solar energy to germicidal UVC—a key component in a number of environmental treatment technologies—became the foundation of our recent work, and the work described herein.

Upconversion is a photoluminescence process exhibited by engineered materials, whereby materials can absorb low energy photons and combine their energies to emit a smaller number of higher energy, shorter wavelength photons. In 2011, our group showcased a first-generation UC phosphor optimized to convert low-power visible light to UVC, and demonstrated its ability to kill surface microorganisms when irradiated with a household fluorescent bulb.[1] With improved efficiency and design, this antimicrobial surface material could be used to kill bacteria and viruses wherever visible light is present—whether in a hospital to combat hospital acquired infections, or in the developing world, to decontaminate drinking water using sunlight. It was clear, however, that substantial gains in performance were necessary before the material could be realistically applied.

The initial goals of this work were to improve the efficiency and mechanical properties of these visible-to-UVC phosphor materials. To create a more robust material, the original phosphor powder, praseodymium-doped yttrium oxyorthosilicate ($Y_2SiO_5:Pr^{3+}$), was used to make upconversion ceramics. The ceramics were not only more structurally desirable for antimicrobial surface applications compared to the first-generation thin films, but they also exhibited significantly higher optical efficiency, and 3x faster microbial inactivation rates were achieved under low-power visible light. It was later observed that the optical enhancements achieved by $Y_2SiO_5:Pr^{3+}$ ceramics could be manifested in other ceramics, as well, suggesting this was a useful tool to optimize UC.

Numerous strategies were employed to further improve UC efficiency, each with varying effectiveness. New synthesis methods and codopant ions resulted in materials that had interesting properties, but none had significantly higher UVC emission. A recently published technique known as dye-sensitized upconversion appeared the most promising, but the optimal dye match for our phosphors was not easily found. Important lessons could be derived from each method, however, which proved useful in understanding the relationships between bulk material modification and UC efficiency.

Finally, while experimenting with doping Pr^{3+} into different crystal hosts, new materials emerged that could more efficiently convert visible light to UV, but at lower wavelengths than $Y_2SiO_5:Pr^{3+}$. Praseodymium-doped yttrium aluminum garnet ($YAG:Pr^{3+}$) phosphors were found to emit much more total UV than $Y_2SiO_5:Pr^{3+}$ and were optimized for UVB-UVA emission. While not germicidal, these wavelengths could be absorbed by wide bandgap semiconductors like TiO_2 for sunlight-driven photocatalysis, which could be used to degrade organic contaminants in water or air. With this in mind, a

proof of concept for UC-activated photocatalysis was achieved using commercial P25 under LED irradiation, thus introducing another useful application for visible-to-UV UC materials.

CHAPTER 1

INTRODUCTION

1.1. OBJECTIVES

The focus of this research was to optimize visible-to-UV upconversion (UC) materials for potential application to light-activated environmental treatment technologies. This work built upon our group's earlier UC research, in which a proof of concept was presented for a visible-light-activated antimicrobial surface material. The material was shown to emit UVC and successfully inactivate surface bacteria under excitation from a household fluorescent bulb. While this was a remarkable concept, the UC efficiency and rates of inactivation were notably low, and real world application would require significantly improved performance. With this in mind, the objectives of the present work included:

- To develop visible-to-UVC upconversion phosphors with higher UC efficiency than first-generation materials, using material and/or chemical modifications
- To engineer an upconversion surface that possesses the durability and structural characteristics that would be desired for antimicrobial surface application
- To broaden the applicability of visible-to-UV phosphors, to include other environmental treatment processes that could be activated by visible light
- To assess the potential effectiveness and real world application of these phosphors, for use under broadband, low intensity irradiation (e.g. solar)

- To gain further understanding of how the properties of UC can be affected, and by extension improved, in these and similar upconversion materials

1.2. HYPOTHESES

A review the available upconversion literature and our previous work suggested four ways to improve the performance of the visible-to-UV phosphors, which lead to these central hypotheses:

1) *Upconversion ceramics:* Upconversion ceramics will have the durability and robustness desired for an antimicrobial surface material. They will also have larger crystallites than powders, which should increase the upconversion efficiency.
2) *Dye-sensitized upconversion:* Coating phosphors with a dye that possesses the appropriate spectral overlap will enhance the effective quantum yield and upconversion efficiency of the phosphor by acting as an antenna for incoming light.
3) *Upconversion-activated photocatalysis:* Visible-to-UV upconversion phosphors, when combined with high band gap photocatalysts like TiO_2, will enable the photodegradation of organic contaminants under low-intensity visible light.
4) *New host materials:* Doping Pr^{3+} into a host crystal with a lower phonon cutoff energy than Y_2SiO_5 should result in higher intensity UV emission.

CHAPTER 2

BACKGROUND

2.1. Upconversion

Most of the photoluminescence processes we are likely to encounter obey Stokes law, in that absorption of excitation light occurs, a portion of the energy is lost as heat, and the emitted photon is always of lower energy and longer wavelength, as shown in Figure 2.1a. The opposite process of anti-Stokes emission can be achieved by using optical materials in several different ways, including second harmonic generation and two-photon absorption–both of which require excitation by high-intensity, coherent laser beams to be observed.[2] To amplify sources such as sunlight or ambient light, a more efficient process that can utilize incoherent low power excitation is required.

Upconversion (UC) is another example of a nonlinear, anti-Stokes optical process. While similar in effect to second harmonic generation and two-photon absorption, the mechanisms of UC are fundamentally different, and the process does not require high-intensity laser excitation.[2, 3] Advances in the synthesis, laser characterization, and understanding of UC materials have led to numerous applications over the past few decades, including anti-counterfeiting devices,[4] advanced solar cell prototypes,[5-9] bioimaging,[10, 11] and photodynamic therapy.[12, 13] While IR-to-visible and visible-to-visible upconversion have been extensively studied for these applications, research on visible-to-UV upconversion for environmental applications has only recently been introduced.

Inorganic UC materials, though less optically efficient than their organic counterparts, are more practical for environmental applications due to their nontoxicity,

chemical resistance, and long-term stability in air and water.[9] Organic UC materials employ a different strategy for frequency amplification which utilizes organic and metallo-organic compounds to achieve UC via the triplet-triplet annihilation mechanism (TTA); further discussion about these materials and mechanisms can be found in the literature.[14, 15] Figure 2.1 illustrates the main UC mechanisms in inorganic phosphors, depicted using energy level diagrams. Here the horizontal lines represent different excited states of a luminescent molecule or species, such as a dye molecule or in our case, a phosphor ion. The number and placement (i.e. energies) of these states are specific to each fluorophore and can be determined or estimated empirically. The shaded bands shown at higher energies represent a large number of overlapping excited states; exciting a molecule into this region will result in the emission of the lowest energy in that band. The bottom lines labeled E_g represent the ground state energies, i.e. the state of the fluorophore when it is not excited.

Figure 2.1a depicts the Stokes emission exhibited by all phosphors, as described previously, in which a photon is absorbed and a photon of lower energy is emitted. In UC phosphors (UCPs), Stokes emission is partially replaced by anti-Stokes emission, whereby a stepwise absorption of two or more photons results in the emission of a single photon of higher energy. For inorganic phosphors, this typically occurs by either of two mechanisms: excited state absorption (ESA; Fig. 2.1b) or energy transfer upconversion (ETU; Fig. 2.1c). In ESA, an ion absorbs one photon to reach an intermediate excited state (E_1) and then immediately absorbs another photon to reach a higher excited state (E_2). For ETU, two neighboring ions (on the order of 10^1 Å apart[16]) are each excited by a single photon, and one reaches the higher energy excited state after resonant energy transfer from the other.

With either mechanism, subsequent relaxation of an electron from the higher excited state (E_2) will release a photon with higher energy than the original photons; a combination of the two excitation energies.

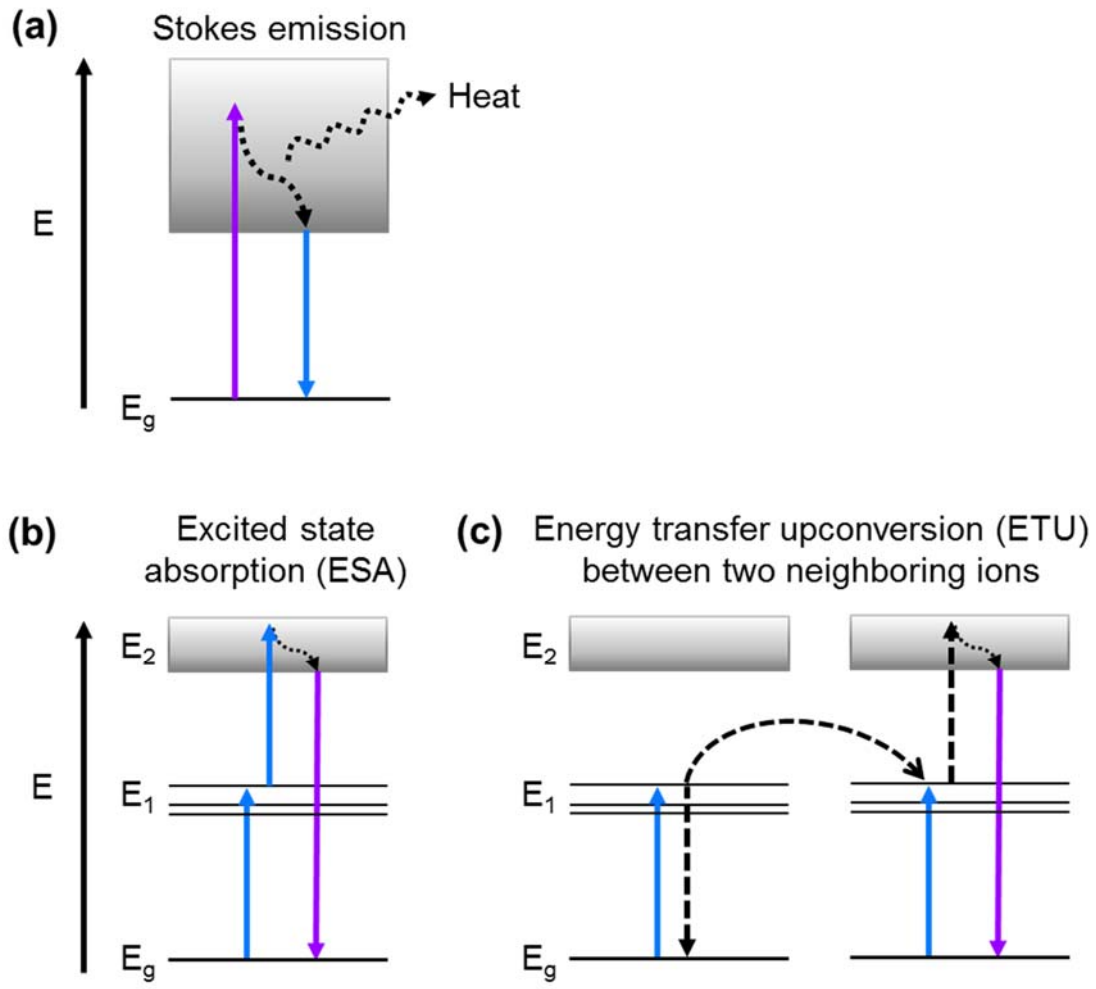

Figure 2.1: Energy level diagrams depicting the general processes of (a) Stokes emission, (b) excited state absorption, and c) energy transfer upconversion. E_g = ground level energy; E1, E2 = higher energy levels, or excited states. Blue arrows show high energy photon absorption/emission, purple arrows show low energy photon absorption/emission, and dashed arrows show nonradiative transitions.

For excitation to the higher excited state (and thus, UC) to occur with any significant probability, the intermediate excited states need sufficiently long lifetimes—on the order of 10^{-6}-10^{-3} s,[2, 3] compared to the ~10^{-9} s lifetimes exhibited by typical luminescent ions. This is a unique property of most trivalent rare earth ions, known as the lanthanides (Ln^{3+}). Inorganic UC phosphors are composed of a crystalline insulator, called the host crystal, doped with Ln^{3+} activator ions. Lanthanide ions possess rich energy level structures suitable for sequential excitation and long-lived excited states, originating from the shielding effect of the 5s and 5p electrons on the 4f valence suborbital.[2, 3] While the optimal amount of doping will depend on the material, low concentrations of ~0.1-10 mol.% are common, as higher concentrations can result in concentration quenching effects.[2, 16]

2.2. Motivation for upconversion antimicrobial surfaces

Infectious diseases are persistent and costly problems worldwide, consistently ranking among the leading causes of death according to the World Health Organization.[17] One of the most common methods of disease transfer is by human contact with a contaminated inanimate object, or fomite. This is a particularly significant problem in hospitals, where in the US alone, an estimated 2 million people contract a hospital acquired infection (HAI) each year.[18, 19] While the most common source of HAI's is thought to be endogenous bacteria in the patient (that is, pre-existing infectious bacteria that had not yet manifested), it is estimated that 20-40% of HAI's result from either direct contact with a patient or indirect contact through contaminated surfaces.[20] To control the latter, hospital surfaces are usually treated using labor-intensive application of chemical disinfectants,

methods which are costly and subject to a wide range of error. It has thus been recognized as advantageous, both economically and for human health, to develop sustainable alternatives.

Of these new technologies, self-disinfecting surface materials have been at the forefront due to their simplistic concept and minimal labor requirements. Materials that have demonstrated antimicrobial surface activity include certain quaternary ammonium silanes, titanium dioxide (TiO_2) or silver nanoparticles (AgNPs), and metallic copper. Copper is currently the only EPA certified material for antimicrobial surfaces.[21] It is well documented, however, that numerous microbial species will develop resistance to copper.[21] The other materials mentioned lack evidence of robustness and long-lasting antimicrobial activity. Polycationic chains such as quaternary ammonium silanes cannot withstand harsh chemical cleaning, and the active portion is a surface monolayer that is subject to removal by abrasion. TiO_2 surfaces require UVA excitation, so TiO_2 alone is not useful indoors; doped TiO_2 can absorb a greater portion of visible light, but photocatalytic efficiency is typically sacrificed. All of the materials listed above rely on direct contact with microorganisms for inactivation to occur, and thus must be free of surface dust and debris to be effective.[19, 22] It was of interest, then, to develop an antimicrobial material that did not require chemical or exhaustible inactivation mechanisms, and would also not be affected by the evolution of infectious bacteria.

Luminescent UC materials that converted visible light to UVC emerged as a possible alternative. UVC photons are heavily absorbed by DNA and RNA, causing the formation of covalent linkages between nucleic acid components to form a variety of detrimental photoproducts; if left unrepaired, these mutations prevent transcription and can

lead to cell death. UVC is regarded as a highly effective biocidal agent, and UVC lamps are commonly used for disinfection purposes, including the disinfection of hospital tools and surfaces.

Additionally, since visible-to-UVC UC materials could be activated by visible light from the sun, they could potentially provide antimicrobial activity to drinking vessels in developing countries, where the transmission of disease through contaminated water is of great concern. In fact, similar solar-activated water disinfection methods have already been employed in certain areas—a technique known as solar water disinfection, or SODIS—wherein water is placed in clear bottles and left out in the sun for hours, eventually disinfected by a combination of solar UV and heat.[23, 24] Alternatively, vessels which absorb visible light (which is much more prevalent in solar irradiation than UV) and emit UVC could potentially be faster and more effective at providing clean drinking water, without imparting undesirable effects such as taste or odor.

2.3. Previous work

Recently our group introduced a phosphor material, yttrium oxyorthosilicate doped with praseodymium ($Y_2SiO_5:Pr^{3+}$), optimized to convert visible light to germicidal UVC using upconversion.[1] These UCPs are nontoxic and can be activated by low-power visible light, such as solar or indoor lighting. Bacteria need only be in close proximity with the phosphor surface—not necessarily direct contact—to be inactivated, yet the UV dose is safe for humans at any distance. Figure 2.2 depicts the concept of this UC material, showing how a coating of UCPs would function as an antimicrobial surface.

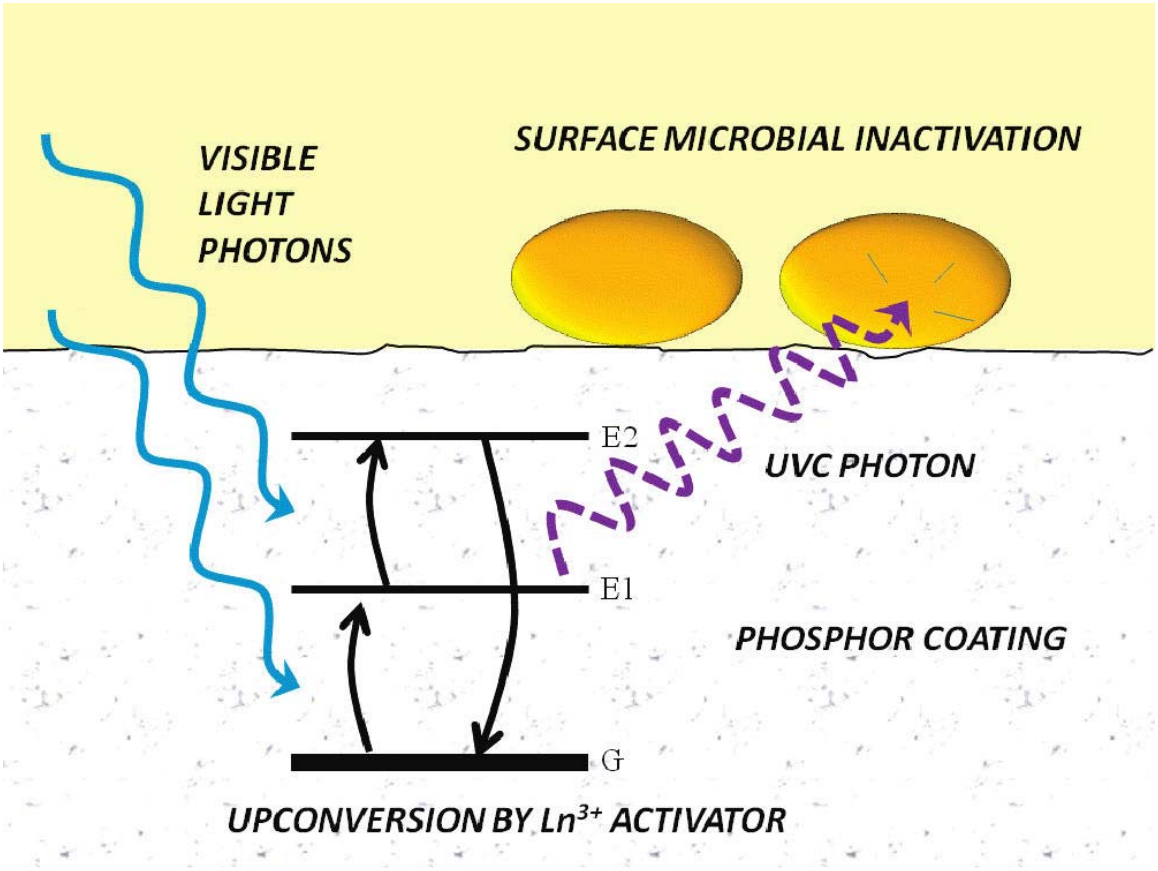

Figure 2.2: Schematic of light-activated antimicrobial surface concept, utilizing inorganic Ln^{3+}-based upconversion phosphors. Reprinted with permission from Cates, E. L., M. Cho, et al. (2011). *Environ. Sci. Technol* 45(8): 3680-3686. Copyright 2011, American Chemical Society.

The UCPs were synthesized as powders and also as films, deposited onto silica slides using a dip-coating method. Significant enhancements in upconversion efficiency were achieved by codoping $Y_2SiO_5:Pr^{3+}$ with gadolinium (Gd^{3+}) and lithium (Li^{+}), and the resulting materials successfully killed bacteria under excitation from a conventional white fluorescent bulb. Microbial inactivation kinetics were obtained using *Bacillus subtilis* spores (Fig. 2.3), and biofilm experiments with confocal imaging showed successful inhibition of *Pseudomonas aeruginosa* biofilms (Fig. 2.4). This was the first (and remains the only) report of a self-activating surface material whose antimicrobial mechanism was the generation of UVC, and also the first demonstration of antimicrobial activity by UCP materials (there has since been a report of HeLa cell death from a visible-to-UVB UC phosphor under laser irradiation, but this was for application to localized, site-specific cell degradation in biological systems[25]). In addition, this was the first demonstration of visible-to-UVC UC under low intensity irradiation (previous studies used only laser excitation); its success thus introduced the possibility of a wide range of low-power light applications.[1]

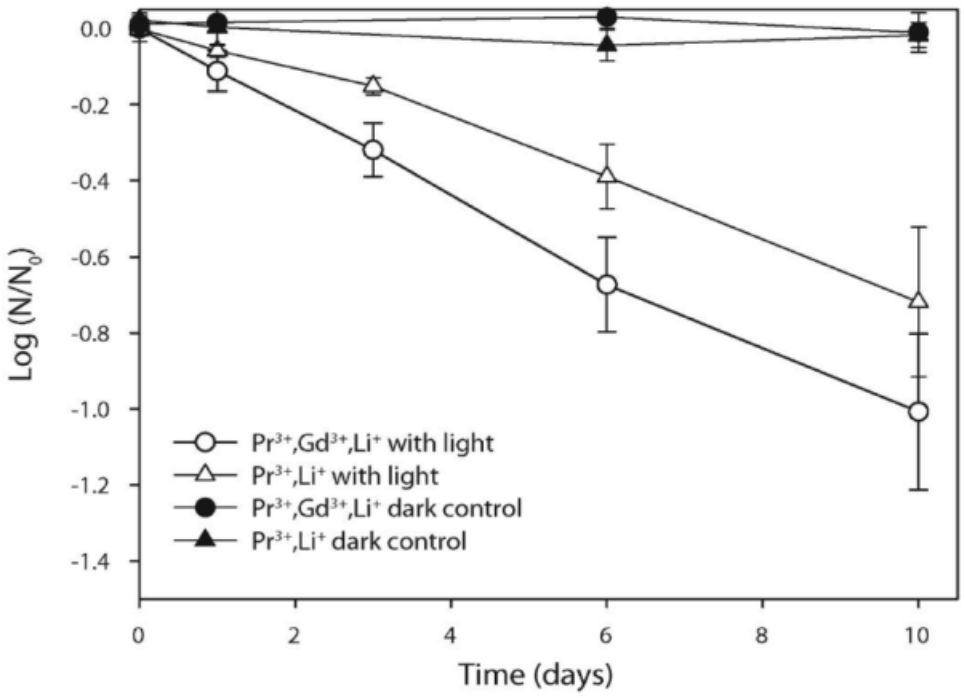

Figure 2.3: Inactivation kinetics of Y_2SiO_5 phosphors with different doping schemes, exposed to "daylight" fluorescent lighting and dark controls. Undoped surfaces showed no inactivation under visible light after 10 days (data not shown). Reprinted with permission from Cates, E. L., M. Cho, et al. (2011). *Environ. Sci. Technol* 45(8): 3680-3686. Copyright 2011, American Chemical Society.

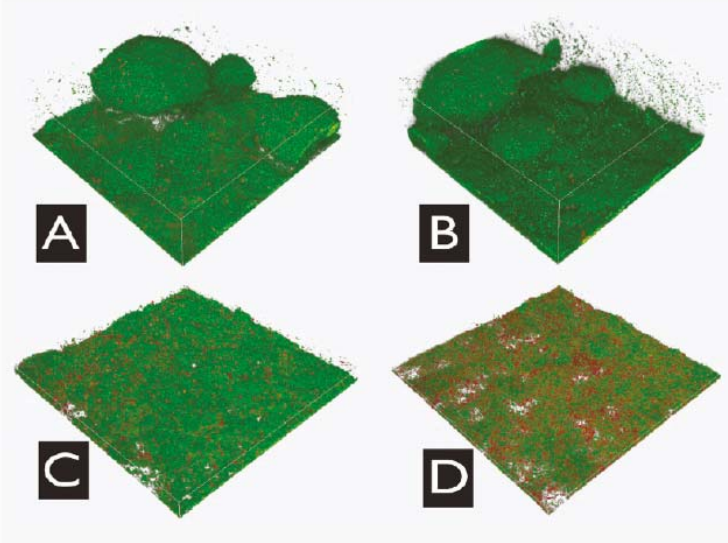

Figure 2.4: 3-D confocal scanning laser micrographs of *P. aeruginosa* biofilms on (A) a surface coated with undoped material under a "daylight" fluorescent lamp, (B) a $Y_2SiO_5:Pr^{3+},Gd^{3+},Li^+$ coated surface in dark conditions, (C) $Y_2SiO_5:Pr^{3+},Gd^{3+},Li^+$ coated surface under visible light, and (D) a $Y_2SiO_5:Pr^{3+},Gd^{3+},Li^+$ coated surface under visible light. A and B (controls) have biofilms and are completely green, indicating all active cells; C and D have no biofilm and are partially covered with inactive cells, stained red. Reprinted with permission from Cates, E. L., M. Cho, et al. (2011). *Environ. Sci. Technol* 45(8): 3680-3686. Copyright 2011, American Chemical Society.

The primary—and major—drawback to the $Y_2SiO_5:Pr^{3+}$ antimicrobial surface material was its low upconversion efficiency, i.e. the percentage of excitation photons that were absorbed and utilized for UC, which then resulted in the emission of UV photons. The calculated efficiency for dip-coated films, based on spore inactivation experiments, was 0.0009%, indicating relatively ineffective utilization of the available light to kill the surface microorganisms. It should be noted that this efficiency was based on low-intensity fluorescent bulb excitation (in fact the lowest reported intensity for the measurement of UC efficiency, 0.002 W/cm^2), and was thus significantly lower than what would be expected under laser excitation, due to the nonlinear excitation dependence of UC. For comparison, one of the most heavily researched inorganic UC materials—$NaYF_4:Er^{3+},Yb^{3+}$, which converts NIR to visible light—has been reported to have a conversion efficiency of 5.5% under 20 W/cm^2 excitation[26] and 0.05% under 1.2 W/cm^2 excitation,[27] and these are generally regarded to be the most efficient amongst Ln^{3+}-UC materials (note, these efficiencies were calculated using the ratio of incident excitation and emitted power intensities, whereas the efficiency for $Y_2SiO5:Pr^{3+}$ was calculated using the ratio of incident excitation and emitted photons, due to the inability to measure such low intensity emission). For the microbial inactivation experiments conducted using dip-coated $Y_2SiO_5:Pr^{3+}$ films, 10 days of light exposure were necessary to achieve 1 log inactivation of spores (90%). To be useful in practical applications such as hospital surfaces, we expect that an efficiency increase of 1 or 2 orders of magnitude would be needed. A more effective way to apply the phosphors was also required, since dip-coated layers were thin, prone to cracking, and easily loosed from the silica substrate. Thus, our initial goals were to create an upconversion material with better structural durability and higher UC efficiency.

CHAPTER 3

UPCONVERSION CERAMICS FOR SELF-DISINFECTING SURFACES

3.1. Introduction

In light of the biocidal nature of UVC radiation and resultant utility in environmental technology, we recently developed an upconversion material optimized to convert low-power visible light into germicidal UVC.[1, 28, 29] The nontoxic phosphors were produced by doping an yttrium oxyorthosilicate (Y_2SiO_5) host with 1.2 mol.% of praseodymium (Pr^{3+}). The energy level diagram in Fig. 3.1c shows the established energy transfer upconversion mechanism between neighboring Pr^{3+} ions, whereby population of ^3P_J states via blue photon absorption and the subsequent energy transfer between ions can promote an electron to the 4f5d energy band, resulting in the emission of UVB- and UVC-range photons.[29-31] It was demonstrated that a thin coating of this material—produced by dip-coating glass coupons in a Y_2SiO_5:Pr^{3+} precursor sol—was capable of emitting UVC photons even under low-intensity visible irradiation; this was evidenced by the inactivation of *Bacillus subtilis* spores and inhibition of *Pseudomonas aeruginosa* biofilms on Y_2SiO_5:Pr^{3+} surfaces upon exposure to a household fluorescent lamp.[1]

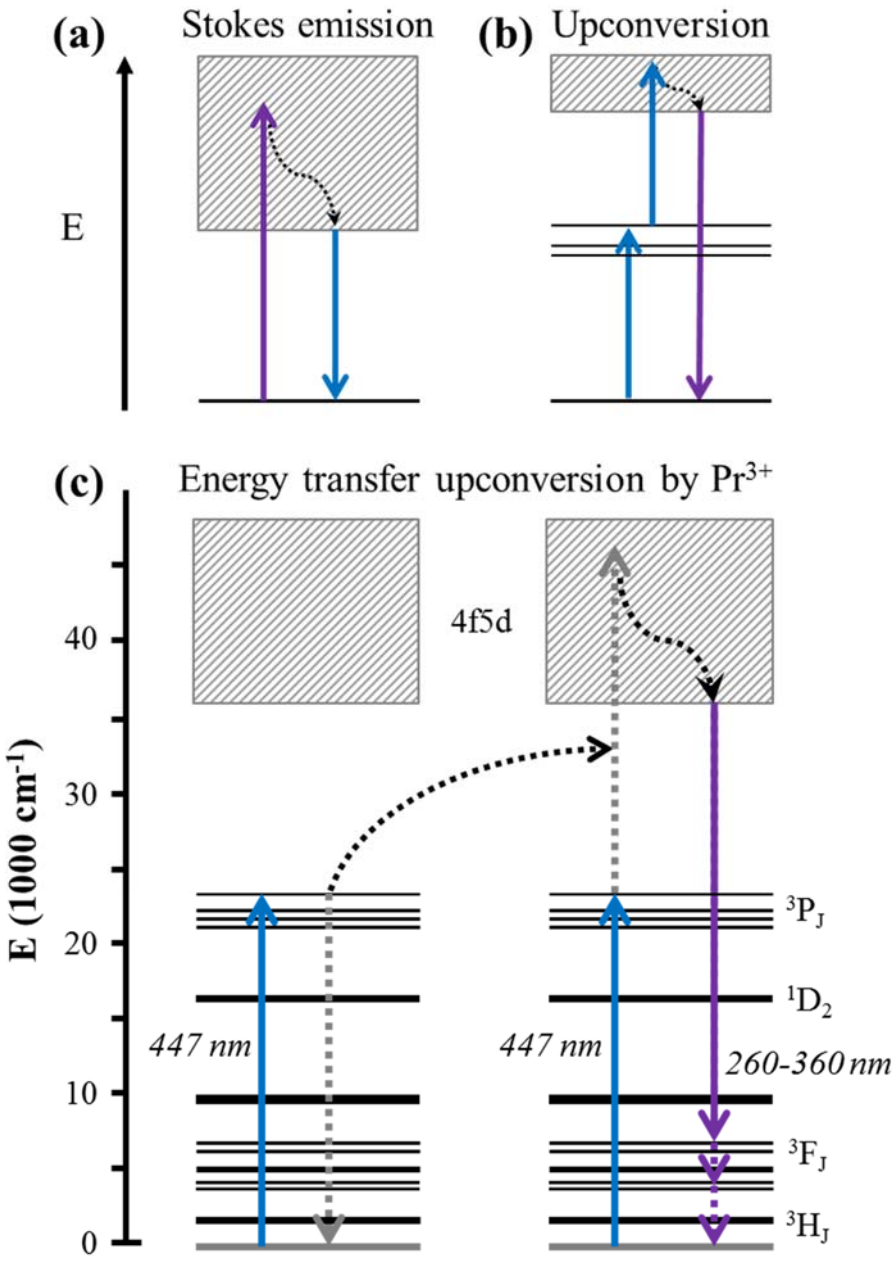

Figure 3.1: Representative energy level diagrams depicting (a) Stokes emission, compared to (b) ESA upconversion; and (c) to-scale, simplified energy level diagram depicting ETU by Pr^{3+} ions, whereby absorption of blue light can result in UVB-UVC emission (note: exact placement of the 4f5d band will depend on host material). Solid lines represent absorbed or emitted photons, and dotted lines represent non-radiative transitions. Reprinted with permission from Cates, S. L., E. L. Cates, et al. (2014). *Environ. Sci. Technol* 48(4): 2290-2297. Copyright 2014, American Chemical Society.[32]

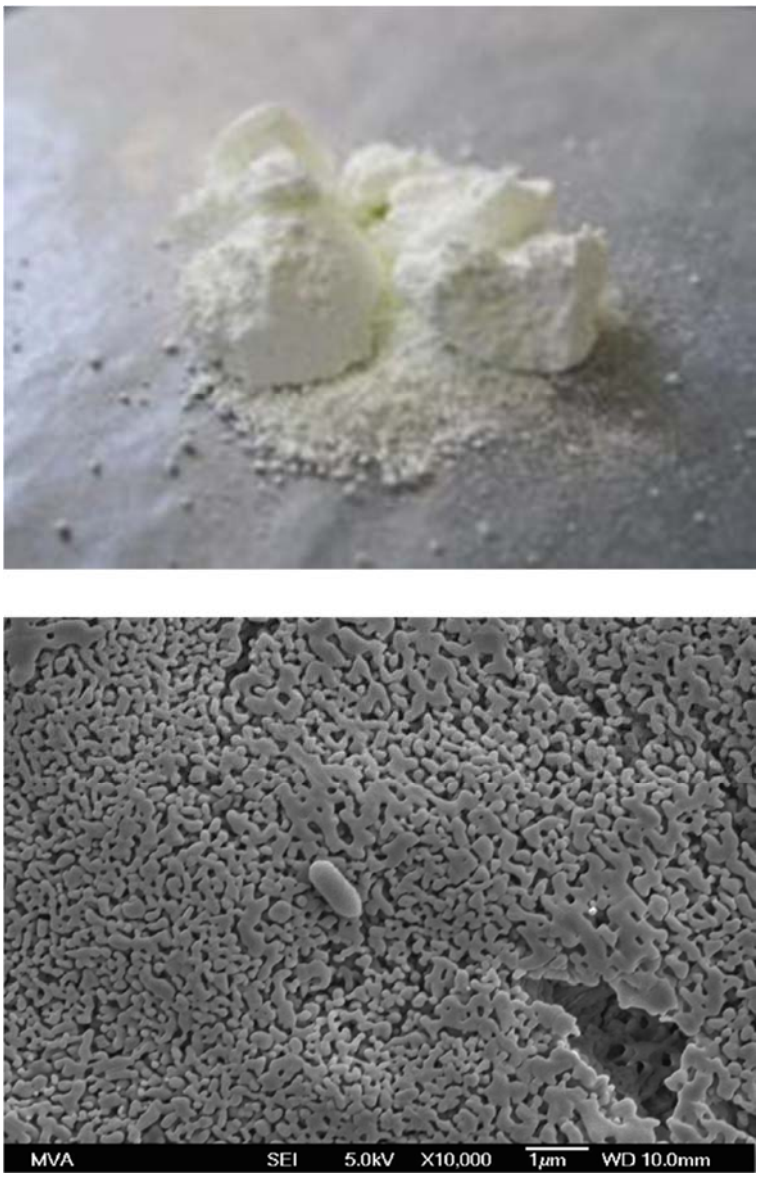

Fig. 3.2: As-prepared sol-gel $Y_2SiO_5:Pr^{3+}$ powder (top) and SEM image of dip-coated $Y_2SiO_5:Pr^{3+}$ film surface, showing *B. subtilis* spore at center for size comparison (bottom). For the dip-coated film, small crystallites and a thin, easily ruptured surface layer are apparent.

While the polycrystalline UCP coatings developed in the aforementioned work offered a convenient proof-of-concept, the samples were fragile, and it was clear that different material forms could better benefit surface applications. Furthermore, the coated films appeared translucent, implying inadequate thickness and inefficient use of excitation light due to transmission losses.[1] Images of the as-prepared powders and thin films are shown in Fig. 3.2. Herein, we investigate the implications of employing the same Y_2SiO_5 $^{3+}$ UC system in the form of a ceramic, rather than a powder or dip-coated film.

The synthesis of ceramic materials typically begins with high-pressure compaction of a powder or slurry into a compressed form, called a green body. The green bodies are then sintered at high temperatures (this will vary depending on material but is usually > 1000 ºC), during which time multiple processes occur, depicted in Fig. 3.3: individual powder particles in close contact begin to fuse together, creating larger crystallites (or grains; pieces of material exhibiting the same crystal phase and orientation) in a phenomenon known as coarsening, and densification occurs as pore spaces diminish and are replaced by grain boundaries. Further grain growth is driven by the high energy at these boundaries. The resulting ceramics will have lower volume, higher density, and greater mechanical strength than the green body. Ceramic properties will vary depending on the properties of the initial powder, pressure used to form the green body, as well as sintering temperature, time, and atmosphere.

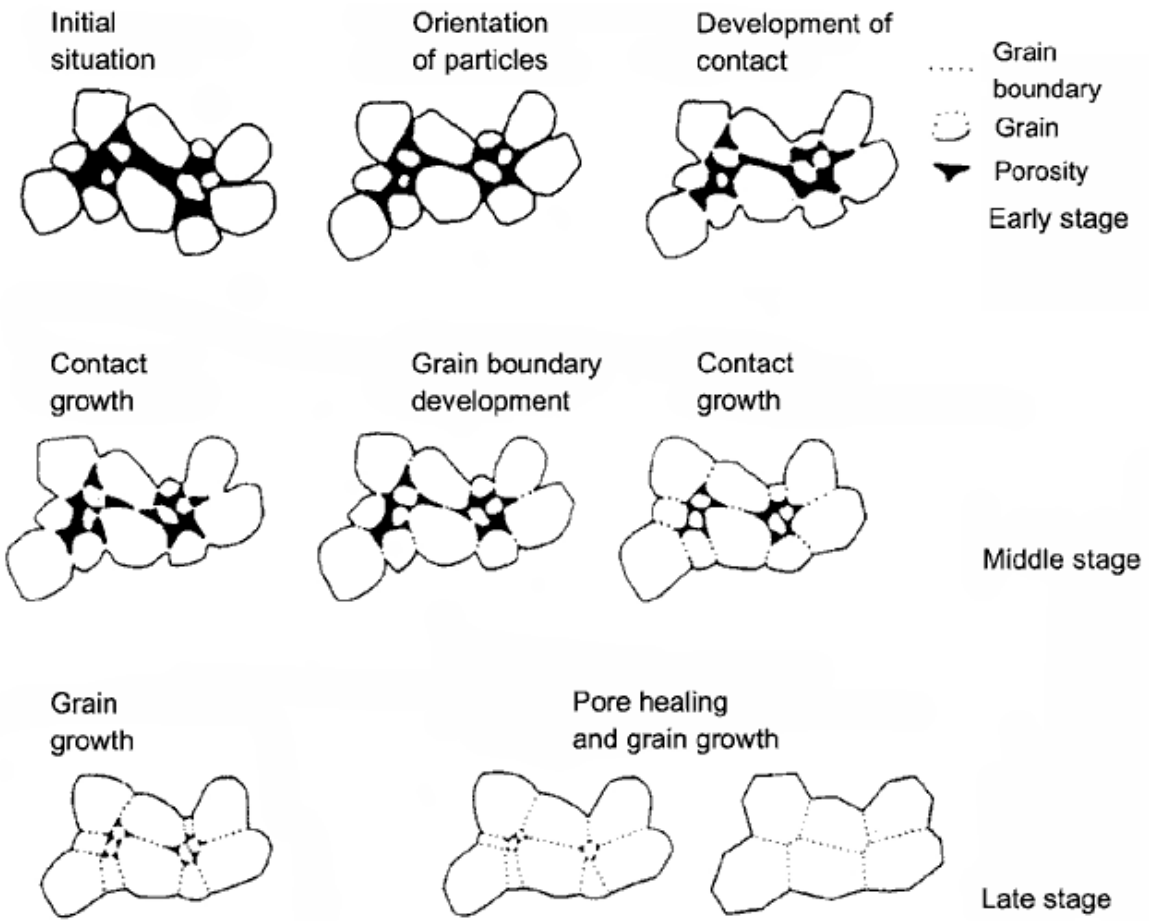

Figure 3.3: Schematic of the ceramic sintering process. The initial situation represents powder particles that have been molded into a green body and are thus tightly packed. (Source: http://www.keramverband.de/brevier_engl/4/1/4_1_4.htm)

The application of UC ceramics has typically been restricted to laser systems, as replacements for costly single crystals,[33, 34] but the structural characteristics of ceramics are also ideal for self-disinfecting surfaces. Ceramic materials are easy to clean, resistant to wear and harsh chemicals, and are already frequently used in a range of environments. Unlike embedding phosphors in a resin or polymer, ceramics also ensure the highest density of active phosphors within a given material mass, without the UV absorption losses that might accompany the use of a polymeric binder. Here we discuss the successful synthesis of Y_2SiO_5-based upconversion ceramics and demonstrate their superior optical and biocidal properties compared to previously-reported antimicrobial upconversion surfaces.

3.2. Experimental

Phosphor Synthesis. Powder Y_2SiO_5 doped with 1.2 mol.% Pr^{3+} and 10 mol.% Li^+ (i.e. phosphors prepared assuming the composition of $Y_{1.909}Pr_{0.024}Li_{0.2}SiO_{(5-y)}$, which will be referred to herein as $Y_2SiO_5:Pr^{3+}$; Li^+ is omitted from this nomenclature because it is added for enhanced crystallinity and material formation, but is not itself optically active) was prepared using a sol-gel decomposition synthesis, as described in our previous work.[1] Phosphor powders were used both for comparison to ceramic and dip-coated samples and also as precursors to make ceramics. In brief, stoichiometric amounts of aqueous $Y(NO_3)_3$, $Pr(NO_3)_3 \bullet 6H_2O$, and $LiNO_3$ were combined, omitting appropriate amounts of $Y(NO_3)_3$ to accommodate dopant substitution, following the stoichiometry $Y_{(2-x-y)}Pr_xLi_ySiO_{(5-y)}$. The nitrates were dried and re-dissolved in water and ethanol before adding a stoichiometric (Si basis) amount of TEOS. This solution was heated to form a gel and then dried in an

oven at 104 °C. The resulting pale-yellow xerogel was ground into a powder and calcined in a furnace at 1000 °C for 3 h in air. Powders were cooled at room temperature and ground before use. It should be noted that, while the original work[1] achieved slightly higher microbial inactivation using Gd^{3+}-codoped samples (possibly due to slight germicidal activity by upconverted UVB emission, which was higher for Gd^{3+} samples), the UVC emission for these samples under PLS was consistently lower than phosphors doped with just Pr^{3+} and Li^{+}, so we chose to focus only on the optimization of the $Y_2SiO_5:Pr^{3+},Li^{+}$ phosphor system.

When designing the ceramic synthesis, conditions were adjusted to achieve materials that were favorable both optically (as determined by photoluminescence spectroscopy) and physically. The latter attribute was characterized by touch; to be considered for use, the pellets had to feel smooth, durable (resist cracking or breaking under normal handling conditions), and could not shed material when rubbed. In the optimized synthesis, powders were first prepared using the above sol-gel method, except the ground xerogels were calcined for 2 hours at 600 °C instead of 3 hours at 1000 °C, to prevent crystallization of Y_2SiO_5 prior to pressing. The resulting precursor powders were then ground and uniaxially pressed at 100 MPa to produce compacted powder pellets (green bodies), using a 13 mm cylindrical steel die. Green bodies were placed in alumina boats and sintered in a tube furnace at 1300 °C for 3 h in air to produce ceramic pellets. The furnace was allowed to cool naturally. Initial powder masses were controlled such that final pellet thicknesses were 1.2 mm. To compare the ceramics to the UCP powder, $Y_2SiO_5:Pr^{3+}$ powders were compacted into pellets using the same pressing method, but the sintering step was omitted. Pellet densities were estimated by measuring the mass and dimensions

of each sample, then comparing the calculated densities to the theoretical density (4.44 g/cm^3)[35] of Y_2SiO_5 in the X2 monoclinic phase (X2-Y_2SiO_5).

Because full volatilization of Li^+ was expected at the high temperatures used for ceramic annealing, it was not treated as a substitutional defect when making sol-gel powders for ceramics, and no $Y(NO_3)_3$ was subtracted from the reactant stoichiometry to accommodate lithium addition. However, ICP-MS analysis of ceramics made with 10 mol.% Li^+ later revealed that only partial volatilization of Li^+ occurred, and it was determined that the final Li^+ content for these ceramics was approximately 2.9 mol.%. The ICP-MS analysis was performed by a certified commercial laboratory.

Dip-coated films of Y_2SiO_5:Pr^{3+} were also prepared for comparison, using the same dip-coating method as in previous work.[1] This involved manual dipping of roughened silica glass squares, 10 mm across, into an aged Y_2SiO_5:Pr(1.2%),Li(10%) precursor sol solution. The squares were dried and annealed at 1000 °C for 1 h, in air, to produce thin polycrystalline films.

Characterization. Photoluminescence spectroscopy (PLS) was conducted using a 447 nm diode-pumped solid-state (DPSS) laser (OEM Lasers) set at 100 mW. The emission signal was processed using phase-sensitive detection, as described previously.[1] For a depiction of the laser setup and components used for PLS, see Appendix A. Spectra were averaged for a minimum of 6 samples per type, and background correction was applied by subtracting the approximately linear background noise from the measurement range of 220-400 nm. Luminescence decay profiles were obtained using an optical parametric oscillator (OPO) pumped with the 355 nm mixed harmonic output of a Q-switched Nd:YAG laser (Continuum Lasers). The final laser pulse was approximately 4 mJ with a 4 ns duration.

The phase purity of ceramic pellets was examined by powder x-ray diffraction (XRD) using a Panalytical X'pert Pro diffractometer with X'celerator detector. Scanning electron microscopy (SEM) was performed using a Hitachi SU-70 SEM, at 10 kV, on chromium sputter-coated samples.

Microbial Inactivation. *Bacillus subtilis* ATCC 6633 spores were prepared and enumerated as in previous work.[36] Ceramic and dip-coated samples were cleaned with water and sterilized by germicidal UVC lamps for several minutes, after which 50 μL of 10^6 cfu/mL spore suspension in 10 mM phosphate buffer saline (PBS) solution was sprayed onto the surface of each sample. To ensure consistency and determine bacteria loading, acrylic coupons with the same cross-sectional area as the samples were first tested as controls, to estimate the volume of inoculum under controlled spraying conditions. Spraying was performed using an atomizer that was held 10 cm above each sample, with spray directed downward and perpendicular to the sample surface. After drying in air on a clean bench, samples were placed in open Petri dishes and covered by a glass UV filter (cutoff <400 nm). Dishes were immediately placed in a collimated beam apparatus equipped with an Osram Dulux S 9W fluorescent bulb, which was turned on for at least 30 minutes prior to each experiment to obtain constant light intensity. A fan was used to prevent the sample area from heating above room temperature. After exposure for a predetermined time period, samples were transferred to a beaker containing 10 mL of 0.05% TWEEN 80 in PBS. The solution was sonicated for 1 min, agitated for 1 min using a vortex mixer, then pipetted for 1 min; these recovery steps were repeated 3 times to fully recover spores from the samples. Released spores were assayed using the spread plate method. Recovery of spores on control sprayed surfaces was over 95% using this method.

Three samples of each type were assayed for every time increment, with data points representing the averages of three like samples.

The collimated beam apparatus exposed samples to a blue light intensity of approximately 1.65 mW/cm^2, measured using a radiometer fitted with a "blue light safety detector" (Solar Light Company, Inc., sensitivity range 400-520 nm). This intensity was higher than the ambient blue light measured from our laboratory bench top (0.05 mW/cm^2), and lower than the standard AM1.5 blue light intensity from solar irradiation (approximately 3.5 mW/cm^2, calculated from the ASTM G173–03 solar irradiance standard,[37] integrated from 435-490 nm).

The optical efficiency of blue-to-UVC upconversion was estimated using biodosimetry, whereby comparison of the inactivation results to a UVC dose-response curve for *B. subtilis* spores allows estimation of the UVC intensity experienced by the organisms. Dose-response experiments were conducted as in previous work,[1] except that the UVC lamp light was attenuated using thin glass slides to maintain a lower intensity of 0.04 mW/cm^2 on the samples, measured using a PMA 2122 Germicidal UVC detector (Solar Light Company, Inc.). The glass slides were assayed over the course of 4 days in the same manner described above for UCP samples, and bacterial inactivation was plotted against UV dose. After fitting a linear regression to the linear portion of this dose-response curve, *B. subtilis* inactivation data obtained from visible light experiments could be used to estimate the "254 nm equivalent" dose emitted by the UCP samples. The blue light power density experienced by the samples during visible light inactivation was measured using a radiometer, as just described. The upconversion efficiency was then calculated as

the percentage of total available blue light that was converted to UVC (254 nm equivalent, with respect to biocidal action) and emitted upwards from the material surface.

3.3. Results and discussion

Synthetic Condition Optimization. The synthesis method for upconversion ceramics was optimized to achieve both high upconversion emission intensity (measured by comparing UVC emission under 447 nm laser excitation) and desirable structural and handling characteristics. Table 3.1 provides a summary of the different variants tested, highlighting the methods that resulted in the optimal ceramic.

Table 3.1: Summary of variants tested for $Y_2SiO_5:Pr^{3+}$ ceramic optimization; highlighted values resulted in the optimal combination of UVC emission intensity, as measured using PLS under 447 nm excitation, and structural durability, evident during material handling.

PROPERTY	VARIATIONS TESTED		
PHOSPHOR SYNTHESIS METHOD	Combustion	Sol-gel	
CODOPANT	Li^+	Na^+ †	Gd^{3+}, Li^+
LITHIUM CONCENTRATION (mol.%)	10%, substituted for Y	10%	12.5%
CALCINING TEMPERATURE (POWDER)	600°C	1000°C	
UNIAXIAL PRESSURE TO FORM GREEN BODY	40 MPa	100 MPa	200 MPa
BINDER (ADDED TO POWDER BEFORE PRESSING)	Water	PVA	None
SINTERING TEMPERATURE (CERAMIC)	1000°C (doesn't produce ceramic)	1300°C	1500°C

† For a detailed discussion of Na^+ doping, see Chapter 4, Section 1.

As seen in Table 3.1, 10 mol.% Li^+ addition to the $Y_2SiO_5:Pr^{3+}$ sol-gel precursor solution, without subtracting any Y^{3+} to accommodate for substitution, resulted in the highest UC emission. Though the majority of the Li^+ added volatilized during sintering, leaving an effective 2.9% estimated using ICP-MS, the inclusion of Li^+ still markedly improved UVC emission compared to having none at all. Because the crystallites form gradually upon heating (even before the fusing of particles and volatilization of Li^+) and it has been seen that X2 crystallization can occur as low as 1000 °C due to a lithium-induced flux effect, it is likely that Li^+ encouraged X2 phase formation and high crystallinity during ceramic sintering in the same manner as we saw during powder calcination.[29] So, while much Li^+ did volatilize after heating to 1300 °C, the effects prior to that point served to improve UC luminescence of the final ceramic. When the amount of yttrium added was decreased to accommodate Li^+ substitution for Y^{3+}, which was optimal for sol-gel powders, the ceramic UC suffered. This can be understood when considering that the final material will have significantly less Li^+ than initially added, and thus there will not be enough atoms to fill each cation vacancy and crystallinity will suffer. Increasing the amount of Li^+ even further to 12.5 mol.% did not improve the intensity of UC emission (emission was approximately equal to that from 10 mol.% Li^+, as observed using PLS). Gadolinium codoping was also tested ($Y_2SiO_5:Pr^{3+}(1.2\%),Gd^{3+}(1.2\%),Li^+(10\%)$), but the resulting ceramics had only ~75% of the UVC emission intensity of the 10 mol.% Li^+ ceramics.

Calcining sol-gel precursor powders at 600 °C before compaction—rather than 1000 °C, as in powder synthesis—aided in the ultimate densification and uniformity of the ceramic pellets. Ceramics made using powders calcined at 600 °C had consistently greater shrinkage during sintering than those prepared from powders calcined at 1000 °C, despite

using an identical pressing procedure. This phenomenon can be attributed to the fact that crystallization of Y_2SiO_5 does not occur at this lower temperature,[16, 21, 38] so particles calcined at 600 °C likely consist of a highly dispersed, amorphous mixture of Y_2O_3 and SiO_2 phases. We confirmed that green compacts of 600 °C precursor powders were non-luminescent under laser excitation, indicating unreacted material. Increased densification of green bodies due to sintering noncrystallized (as opposed to crystalline) powder compacts has been observed for other types of ceramics in the literature.[39-41] Suggested causes include a higher thermodynamic driving force for noncrystalline particles to fuse together during sintering,[41] and also increased packing density during the pressing stage. The latter can occur due to smaller particle sizes in the powder, as sol-gel powders tend to form larger aggregates upon crystallization.[39]

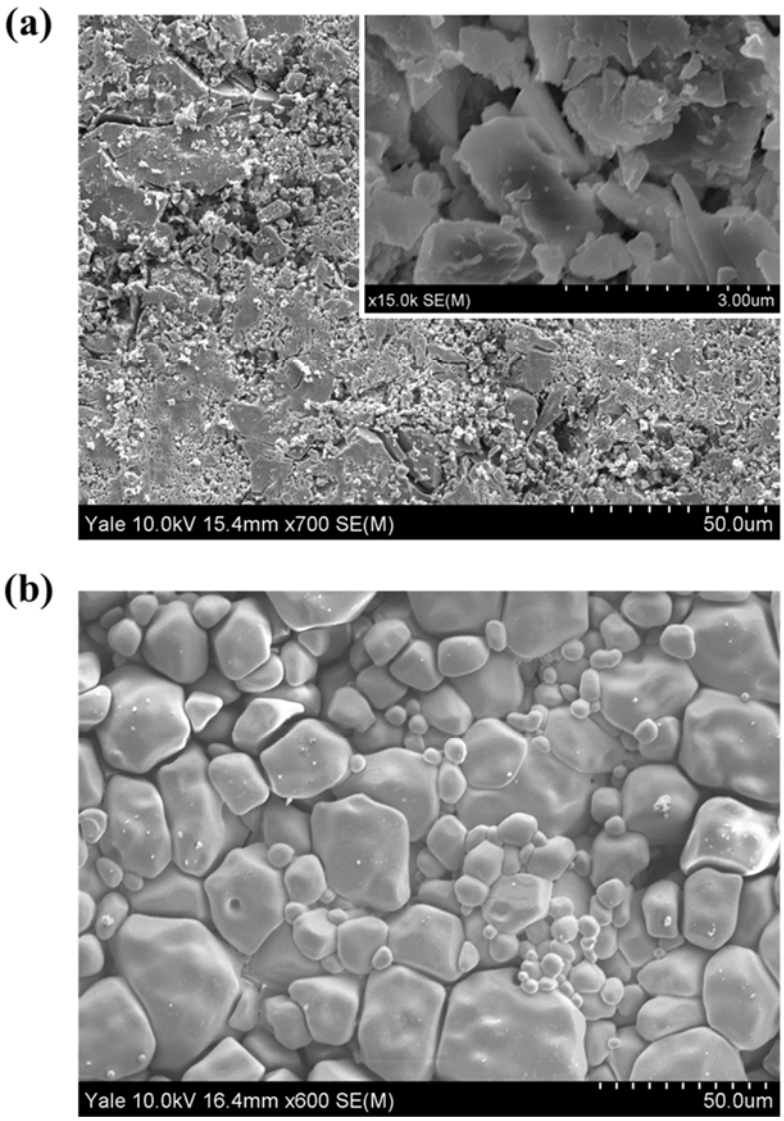

Figure 3.4: SEM micrographs of (a) $Y_2SiO_5:Pr^{3+}$ precursor powder, pressed into a green body pellet, and (b) ceramic $Y_2SiO_5:Pr^{3+}$, obtained after sintering the green body for 3 h at 1300 °C. Both are shown on the same scale for comparison (50 μm scale bar, 5 μm between ticks); inset for (a) shows a magnified view of precursor material (3 μm scale bar, 0.3 μm between ticks). Reprinted with permission from Cates, S. L., E. L. Cates, et al. (2014). *Environ. Sci. Technol* 48(4): 2290-2297. Copyright 2014, American Chemical Society.

The highest pressure at which the green body pellets could be produced consistently was found to be 100 MPa; pellets formed at lower pressures were more often subject to fracture, while higher pressures often induced capping. Pellet densities increased significantly upon sintering, from the green density of ~61 % to a ceramic density of ~93 %. A corresponding reduction in porosity was visible in SEM images, wherein dark (pore) space was clearly more prominent on the green body surfaces (Fig. 3.4a) than on the ceramics (Fig. 3.4b). SEM also revealed a dramatic increase in particle sizes for the ceramics, indicating successful particle fusing during the sintering process. Ceramic grains ranged from a few μm to upwards of 50 μm. To compare the ceramic microstructure with the UCP powder and dip-coated films, we refer the reader to SEM micrographs of identical materials shown in previous work;[1, 29] we observed that dip-coated films comprised irregularly shaped, nanocrystalline grains,[1] while powder crystallites ranged from tens of nanometers to ~1.5 μm in size.[29]

Optical Properties. Photoluminescence spectroscopy was used to measure the relative luminescence intensities of each sample under 447 nm laser excitation. Photons of this wavelength can populate the ^3P_J intermediate states in Pr^{3+} and be converted to UVC radiation through the ETU mechanism shown in Fig. 3.1b, or similarly through an ESA mechanism.[29-31] In general, ETU is two orders of magnitude more efficient than ESA,[2] and is assumed to be dominant at the laser power densities employed. All powder and ceramic samples exhibited the characteristic UC emission spectra for X2-Y_2SiO_5:Pr, featuring a minor shoulder in the UVB range and a primary UVC peak centered at 278 nm, resulting from 4f5d→^3H_J/^3F_J transitions (Fig. 3.5). Samples were compared to designated control samples to ensure that the UVC peak intensity was consistent.

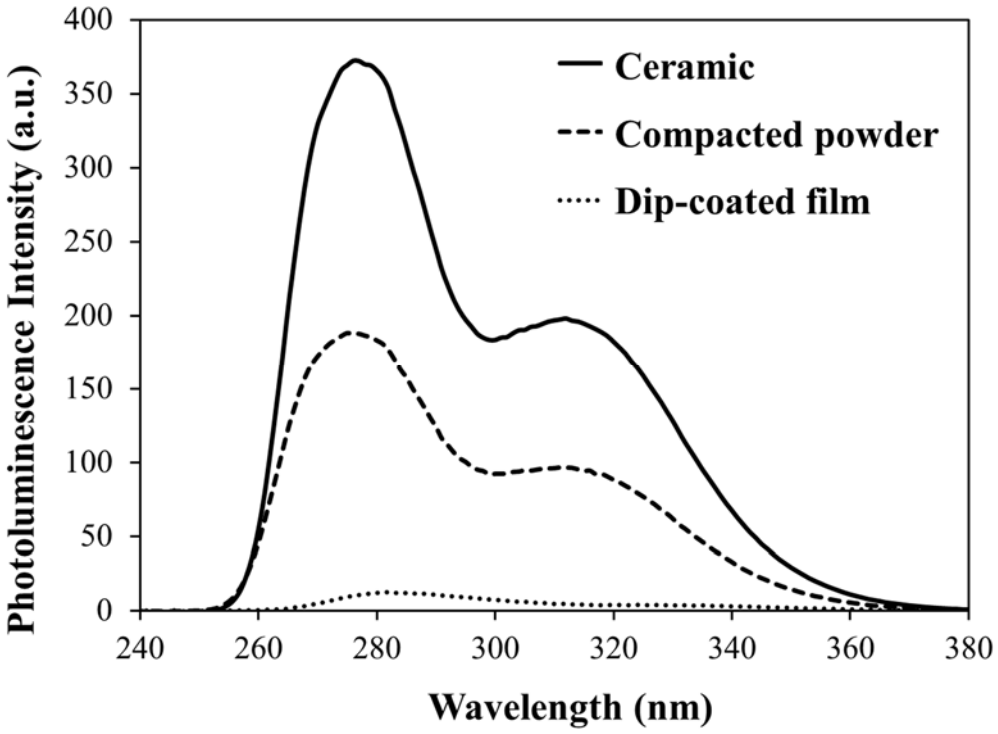

Figure 3.5: PLS showing the relative intensities of UC emission for ceramic, compacted powder, and dip-coated $Y_2SiO_5:Pr^{3+}$ under 447 nm laser excitation. Upconversion luminescence peaks at 278 nm (UVC) for both the ceramic and powder, characteristic of X2-$Y_2SiO_5:Pr^{3+}$, while dip-coated films exhibited an emission peak at 281 nm, characteristic of X1-$Y_2SiO_5:Pr^{3+}$. Standard deviations calculated at the peak positions were not large enough to be discerned on this scale, and are not shown. Reprinted with permission from Cates, S. L., E. L. Cates, et al. (2014). *Environ. Sci. Technol* 48(4): 2290-2297. Copyright 2014, American Chemical Society.

Since measured UC intensities were found to increase with increasing sample thickness, pellet thicknesses were controlled by weighing a fixed mass of powder before pressing each sample. This provided consistent UC intensities for each sample. Figure 3.6 depicts the variance in peak intensity for ceramics from the same batch synthesis but with different thicknesses. It appears that material within a given depth from the ceramic surface (at this laser excitation, approximately 1.6 mm) can contribute to the measured UV emission, but beyond this depth the emission is immeasurable, and thus extra thickness does not further increase observed emission. This can be extended to our understanding of the UC materials under lower intensity irradiation, suggesting that increased thickness can improve antimicrobial efficacy up to a certain point. This also confirms that even phosphors far beneath the topmost layer of material can be irradiated and successfully emit UV outward, which could be used to kill microorganisms. The “active layer” that could contribute to surface inactivation would presumably be much thinner under normal light intensities compared to the laser experiments described here, but again we see an advantage of the UVC inactivation mechanism compared to other antimicrobial surfaces that require direct contact between the material and microorganism.

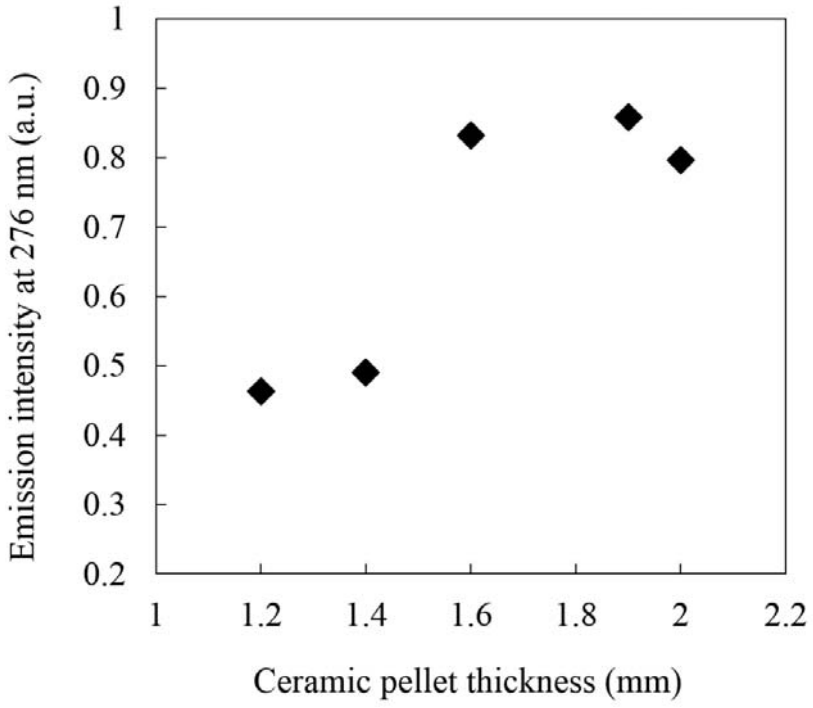

Figure 3.6: Variation of upconverted UV peak intensity (λ_{ex} = 447 nm) with ceramic pellet thickness. All pellets are $Y_2SiO_5:Pr^{3+}$.

A direct PLS comparison of the $Y_2SiO_5:Pr^{3+}$ ceramic to the first generation $Y_2SiO_5:Pr^{3+}$ dip-coated films showed a significant improvement in upconversion intensity under laser excitation. Ceramics exhibited 34 times higher UVC emission intensity, integrated over the biocidal wavelength range (220-290 nm, as estimated from the action spectrum of *B. subtilis* inactivation under UV irradiation)[42]. This can be attributed in large to the increased thickness of the ceramics (1.2 mm compared to 100-200 μm for the dip-coated films), and higher density of the ceramic samples. The latter assertion is visibly apparent when comparing the ceramic SEM to the $Y_2SiO_5:Pr^{3+}$ dip-coated film SEM image in Fig. 3.2, which showed significant porosity.

Although the compacted powders (calcined at 1000 °C) are impractical as a surface material and were not used for microbial experiments, they were used as the benchmark material for optical characterization. Prior to this study, these powders were the most UC-efficient and well characterized form of $Y_2SiO_5:Pr^{3+}$.[1] As depicted in Fig. 3.5, the UVC upconversion intensity for ceramics was approximately two times higher than for compacted powders. The green bodies used for ceramics were identical in size to the compacted powder pellets, so after sintering, the ceramics were slightly thinner but also denser than the powder counterparts. The large increase in UC intensity suggested that factors other than material thickness and density were encouraging UC. This result could be explained by the increased crystallite sizes observed under SEM. Since energy transfer from lanthanide activators to surface impurities with high-energy vibrational modes is a major source of efficiency loss in UCPs, larger crystallites are known to result in higher efficiencies, as a greater portion of activator centers are located within the particle and separated from the surface environment.[3, 29, 43, 44]

Cross relaxation rates and intermediate state lifetimes were measured to further investigate the mechanisms behind the enhanced UC efficiency of ceramics, compared to the UCP powders. Typically, mechanisms that depopulate the intermediate ^3P_J states will hinder UC efficiency, so one might expect lower cross relaxation and likewise longer ^3P_J lifetimes for more efficient materials. As depicted in Fig. 3.7b, cross relaxation between Pr^{3+} ions involves phonon-assisted energy transfer from an ion excited to the $^3P_0$ state, resulting in light emission from the $^1D_2$ state, non-radiative decay, and ultimately a decrease in UC probability.[45, 46] The relative rates of cross relaxation could thus be probed by measuring the Stokes emission spectra (portion shown in Fig. 3.7a) and noting that an increase in $^1D_2$-originated emission indicates more prevalent cross relaxation. Following the reasoning described in previous work,[29] the ratio of $^1D_2 \rightarrow {}^3H_4$ emission (integrated from 603-613 nm) to $^3P_0 \rightarrow {}^3H_5$ emission (integrated from 547-557 nm) was chosen to compare the cross relaxation rates for the two sample types. Interestingly, ceramic samples exhibited a slightly higher ratio than powders (Fig. 3.7a), suggesting that the enhanced UC in ceramics was not due to a reduction in cross relaxation. In fact, a greater degree of cross relaxation in the ceramics was not unexpected. The higher annealing temperature and duration, coupled with evaporative loss of most of the Li^+ additive, should result in the Pr^{3+} ions diffusing to a thermodynamically-preferred clustered distribution. In the clusters, inter-ion separation is lower, enhancing the rate of cross relaxation. This phenomenon is established in the literature[47] and, additionally, evidence exists showing that the ability of the Li^+ codopant to enhance UC in the powder phosphor is partially attributed to dispersal of such clusters.[29, 48, 49]

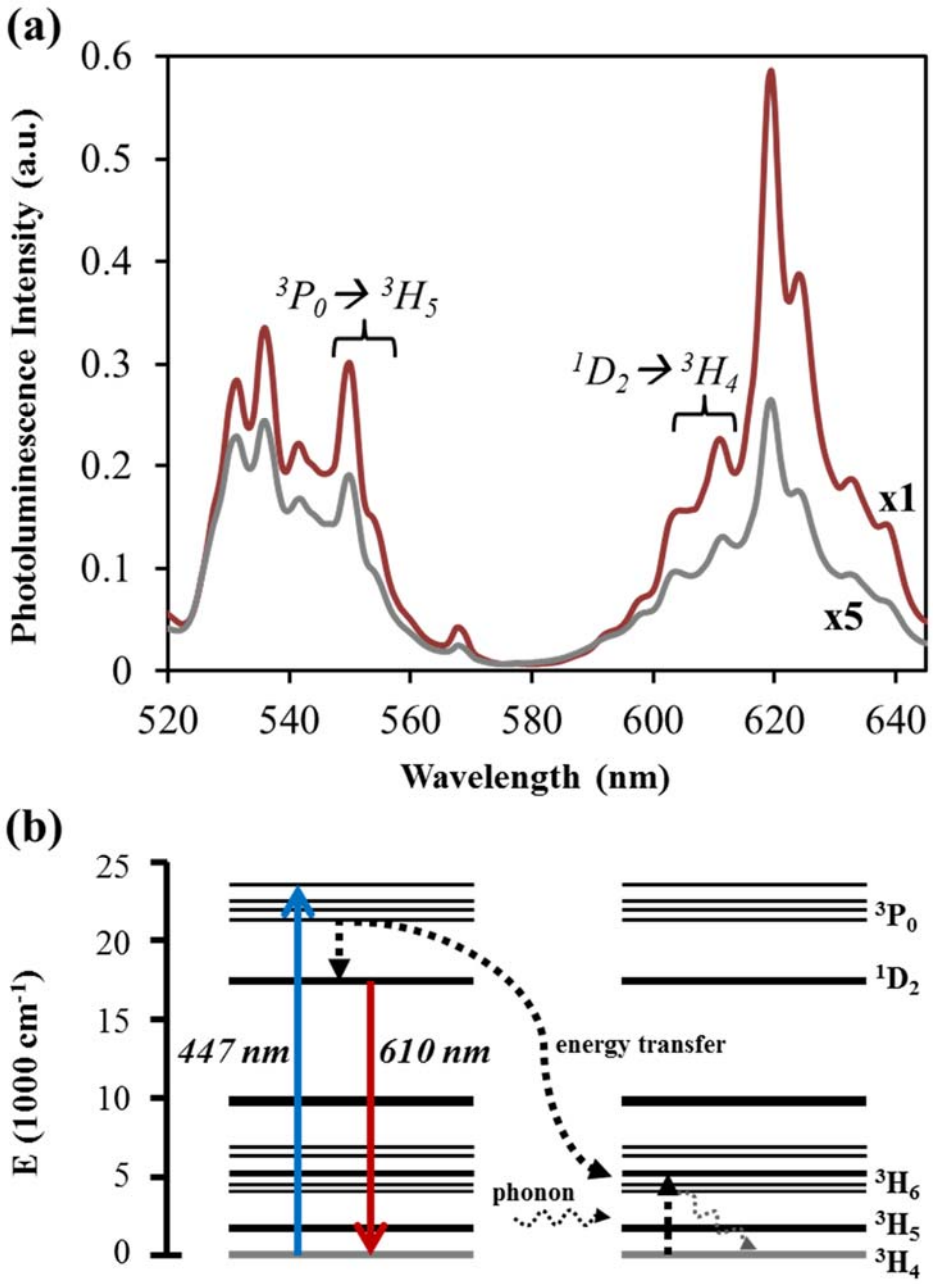

Figure 3.7: (a) Stokes emission spectra for ceramics (red), compared to compacted powders (gray). Absolute emission was adjusted to place both data sets on the same scale, for visual comparison. Cross-relaxation rates were estimated using the ratio of $^1D_2 \rightarrow {}^3H_4$ emission (integrated from 603-613 nm) to $^3P_0 \rightarrow {}^3H_5$ emission (integrated from 547-557 nm). (b) Energy level diagrams depicting phonon-assisted cross relaxation between two Pr^{3+} ions, which results in ~610 nm ($^1D_2 \rightarrow {}^3H_4$) emission. Solid arrows represent absorbed or emitted photons, and dotted arrows represent non-radiative transitions. Reprinted with permission from Cates, S. L., E. L. Cates, et al. (2014). *Environ. Sci. Technol* 48(4): 2290-2297. Copyright 2014, American Chemical Society.

Nevertheless, luminescence decay measurements of $^3P_0$ fluorescence shown in Fig. 3.8 followed the trend of upconversion intensity in that ceramics had slightly longer intermediate state lifetimes. This relationship is expected since the nonlinear statistical dependence of UC emission on excitation intensity is intimately affected by intermediate state decay kinetics.[2] The calculated room-temperature $^3P_0$ lifetimes for powders and ceramics were 2.75 μs, and 3.32 μs, respectively. Luminescence decay profiles followed a roughly double-exponential pattern (transitioning from faster exponential decay between ~0-1.5 μs to slower decay from ~2-7 μs), and lifetimes were estimated from the latter portion. This range of values is generally consistent with our previous measurement of 2.25 μs for the powder phosphor, using a different instrument.[28] These results further suggested that the larger crystallite sizes in the ceramics were partially responsible for enhancing the ^3P_J lifetimes and UC efficiency; indeed, the enhancement was large enough that even with greater cross-relaxation, significant improvement in UC was still observed.

Luminescence curve shape and peak positions were the same for the compacted powder and ceramic samples, while dip-coated films exhibited slightly red-shifted peaks, characteristic of a different Y_2SiO_5 polymorph (Fig. 3.5). This crystal system exhibits two phases known as X1 (space group P21/c) and X2 (I2/a), with the former being metastable and forming at temperatures below ~1250 °C and the latter occurring at higher annealing temperature.[29, 50] Previous work has also confirmed that Li^+ addition induces formation of the X2 phase at lower temperatures.[1, 29] Praseodymium doped into the respective phases show different 4f5d band energies due to the nephelauxetic effect; thus, each polymorph exhibits a distinctive Pr^{3+} UV emission signal.[1] Herein, UCP powders and ceramics exhibited the X2 structure, evidenced by the UC emission and confirmed by XRD (Fig.

3.9). The dip-coated films, however, were found to be of the X1 structure, in disagreement with previous assumptions;[1] this result occurred despite identical composition and annealing conditions to the powder UCP, and the reason for the phase difference is unknown. This could provide a minor contribution to the differences in antimicrobial efficacy described below, as the X1-phase UCP has a slightly different UC excitation spectrum and its emission has less overlap with the *B. subtilis* UVC action spectrum.[29, 42]

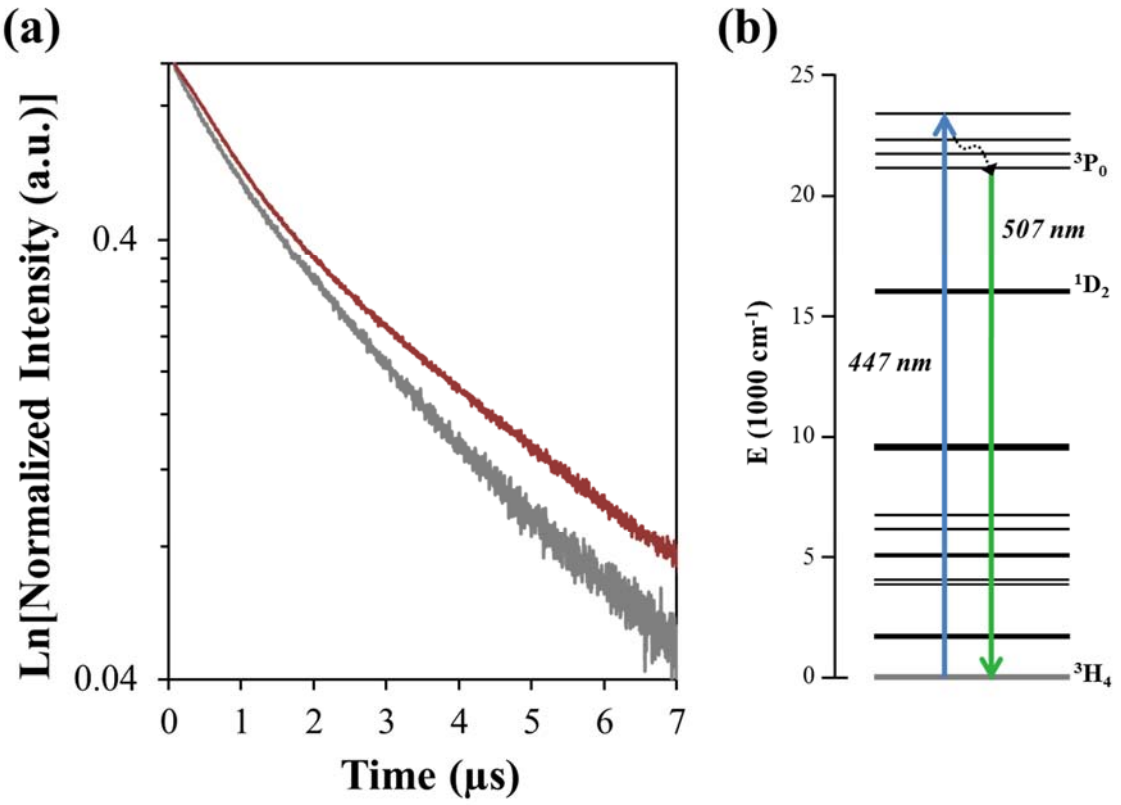

Figure 3.8: (a) Natural log of luminescence decay profiles for the 507 nm ($^3P_0 \rightarrow {}^3H_4$) fluorescence from ceramics (red) and compacted powders (gray), measured under 447 nm pulsed laser excitation. (b) Depiction of $^3P_0 \rightarrow {}^3H_4$ fluorescence mechanism in Pr^{3+}; solid blue line represents 447 nm absorption, black dotted line represents non-radiative relaxation, and solid green line represents 507 nm emission. Reprinted with permission from Cates, S. L., E. L. Cates, et al. (2014). *Environ. Sci. Technol* 48(4): 2290-2297. Copyright 2014, American Chemical Society.

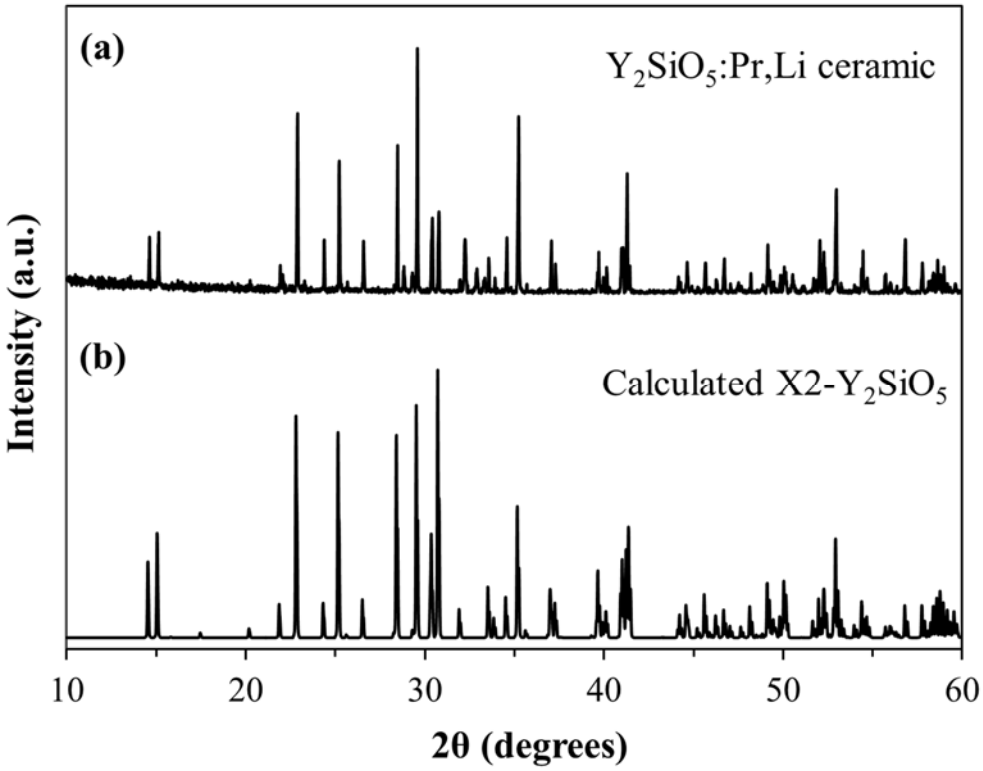

Figure 3.9: XRD pattern of the 1300 °C-Y_2SiO_5:Pr^{3+} ceramic, with 10 mol.% lithium additive. Peaks are characteristic of the X2 phase of Y_2SiO_5, which is shown below for comparison. Reprinted with permission from Cates, S. L., E. L. Cates, et al. (2014). *Environ. Sci. Technol* 48(4): 2290-2297. Copyright 2014, American Chemical Society.

Surface Microbial Inactivation. Improvements in UC efficiency were also apparent under low-power visible excitation, as evidenced by the inactivation of *B. subtilis* spores on UC surfaces under a commercial "cool white" fluorescent bulb (Fig 3.10a). Rates of spore inactivation (log_{10} inactivation per day) were estimated by fitting regression lines to the approximately linear portion of the inactivation data, from 4 to 8 days of light exposure. The $Y_2SiO_5:Pr^{3+}$ ceramic surfaces exhibited 3.9 times greater inactivation rate compared to the dip-coated $Y_2SiO_5:Pr^{3+}$ films. The ceramics achieved 1.6-log inactivation of spores after 8 days of visible light exposure. Since the inactivation curves showed a lag period and did not become linear until halfway through the experiment, and the dose-response of the organism was not linear, the ratio of log inactivation between the ceramic and dip-coated materials varied with inactivation time. Ceramic $Y_2SiO_5:Pr^{3+}$ samples in dark conditions showed near-zero inactivation of the spores throughout the sampling period, as expected, since the materials have no known chemical antimicrobial effect.[1]

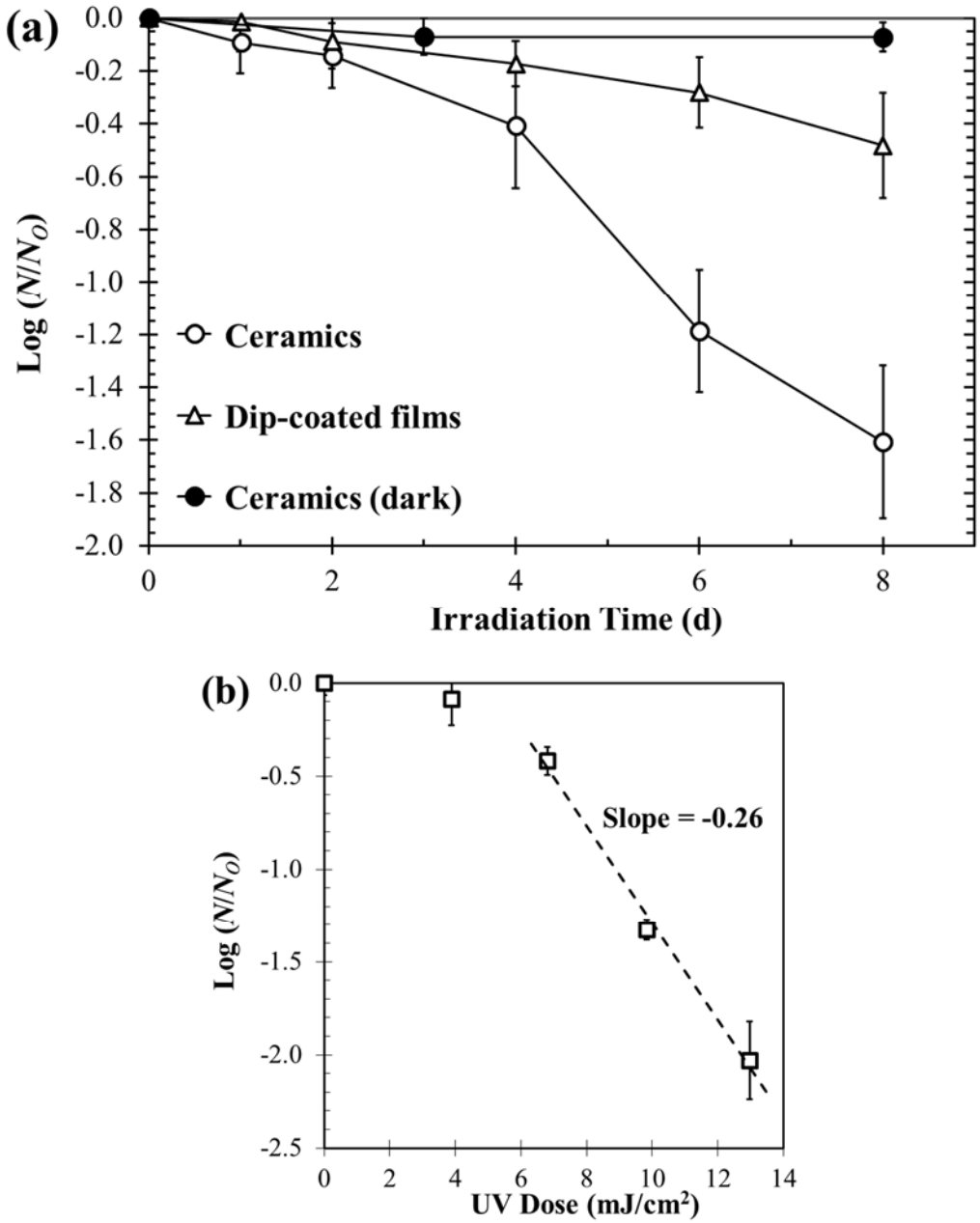

Figure 3.10: (a) Inactivation of *B. subtilis* spores on ceramic and dip-coated film surfaces, over 8 days of exposure to visible fluorescent light. Ceramic samples that were not exposed to light were tested as controls. (b) UVC dose-response curve showing *B. subtilis* spore inactivation under low-intensity (0.04 mW/cm^2) UVC irradiation. A linear regression (dashed line) was plotted for the latter portion and used to calculate upconversion efficiencies. Reprinted with permission from Cates, S. L., E. L. Cates, et al. (2014). *Environ. Sci. Technol* 48(4): 2290-2297. Copyright 2014, American Chemical Society.

These inactivation results confirmed that UC by the ceramic phosphors was more efficient than the previously reported film coatings; however, the enhancement observed under fluorescent lamp excitation was significantly less than the 34-fold enhancement under laser excitation, measured by PLS. We attribute this disparity to the significant difference in thickness between the two types of UC surfaces. Ceramics were approximately 5 times thicker than the dip-coated films, and comprised dense, optically active material. The laser used for PLS subjected samples to a light intensity on the order of thousands of mW/cm^2, which was strong enough to visibly penetrate the sample thicknesses to a considerable extent; a red glow from the $^1D_2 \rightarrow {}^3H_4$ emission could be seen even on the backside of the opaque pellets, viewed through blue laser safety glasses. Thus, it is reasonable to assume that material beneath the sample surfaces encountered sufficient residual light intensity to achieve UC and emit a measurable contribution of UV back through the material and outwards from the surface. Under the much weaker light intensity of the fluorescent bulbs, a much thinner portion of each sample will experience sufficient blue light intensity to emit significant UVC. In effect, though actual thicknesses differed widely between the ceramics and dip-coated films, the "active layer thickness" was likely more similar under the fluorescent lamp condition. This likely explains why ceramics exhibited much higher upconversion than the films with PLS, while microbial inactivation was enhanced to a lesser degree. Nevertheless, the observed 3.9-fold improvement in inactivation rate by the ceramic materials represented a major improvement in UC antimicrobial performance.

It is important to keep in mind that while multiple days of light exposure were required to achieve these inactivation levels, bacterial spores have much lower UVC

susceptibility than active and vegetative cells.[51, 52] *Bacillus subtilis* spores were chosen for inactivation experiments due to their resilience, to ensure that visible light, heat, and natural bacteria mortality could be ruled out as causes of inactivation, given the relatively long time scale of the experiments. More ubiquitous vegetative bacteria such as *E. coli* are known to exhibit up to 10 times faster inactivation under concentrated UVC radiation, when compared to spores.[51, 53, 54]

Upconversion Efficiency. Upconversion efficiencies were estimated using biodosimetry, wherein the inactivation of *B. subtilis* spores were measured under controlled UVC doses from a UVC lamp. Unlike our efficiency calculations in previous work, which utilized a similar method, the dose response curve was obtained using much lower UVC intensity (0.04 mW/cm^2, compared to 0.3 mW/cm^2 in previous work).[1] This was chosen to better mimic the low intensity UVC that is emitted by the UCPs under fluorescent light. We found that the rate of *B. subtilis* spore inactivation was higher using a lower UVC intensity for a longer amount of time, as opposed to exposing the spores to the same UVC dose but with higher intensity for a shorter time (Fig. 3.10b). It appeared, then, that a slight over-calculation of UC efficiency may have been made previously.[1] It is worthwhile to note that the biodosimetry data both here and in our past work were collected using spores that were deposited and dried onto sample surfaces; UV dose-response curves for *B. subtilis* found in the literature were measured using spores irradiated in liquid suspensions,[55] which should exhibit slower inactivation kinetics.

Using the low-intensity UV dose-response curve, the UC efficiency of the $Y_2SiO_5:Pr^{3+}$ ceramics was calculated as 0.0019 %, whereas $Y_2SiO_5:Pr^{3+}$ dip-coated films had an efficiency of approximately 0.0012 %. The corresponding UV doses delivered by

the ceramics after 4 and 8 days were estimated to be 6.8 mJ/cm^2 and 11.2 mJ/cm^2, respectively. For details of this calculation, see Appendix A. Since biodosimetry experiments were conducted using a 254 nm lamp, these values assume that the average UVC dose emitted by the phosphors was equal to the dose of 254 nm radiation required to achieve the same inactivation of *B. subtilis* spores. Though UVC emission spectra for the UCPs peak at 278 nm rather than 254 nm, the documented action spectra for this *B. subtilis* strain suggest that the spores would respond similarly to the two wavelengths.[42]

3.5. Conclusion

While we recognize that further material development and optical efficiency gains are required for commercial viability of UC antimicrobial surfaces, this work is an example of the continuing progress being made toward this and other target applications. By designing materials with desirable physical properties for surface application, the upconversion efficiency and resulting antimicrobial activity of these UCPs were noticeably improved, representing the best inactivation rates to date for UC-based disinfection. Upconversion ceramics are a physically and chemically robust choice for antimicrobial surfaces, and are presumed to be non-toxic, non-leaching, and resistant to chemical cleaning. The parent compound used here, X2-Y_2SiO_5, is well known to possess exceptional chemical and mechanical stability and is even being pursued for use as high-temperature environmental barrier coatings.[56-58] In addition to prevention of fomitic disease transfer, visible-to-UVC ceramic coatings might eventually be applied to water disinfection, and could potentially provide a solar-powered, odor-free technology for potable water in developing countries.[9] The ease of adapting ceramic materials to various

shapes and surfaces is well known, including large-scale coating processes, such as thermal spray coating and magnetron sputtering. Figure 3.11 depicts the ceramic materials produced in this work, which could be molded into pellets or larger tiles.

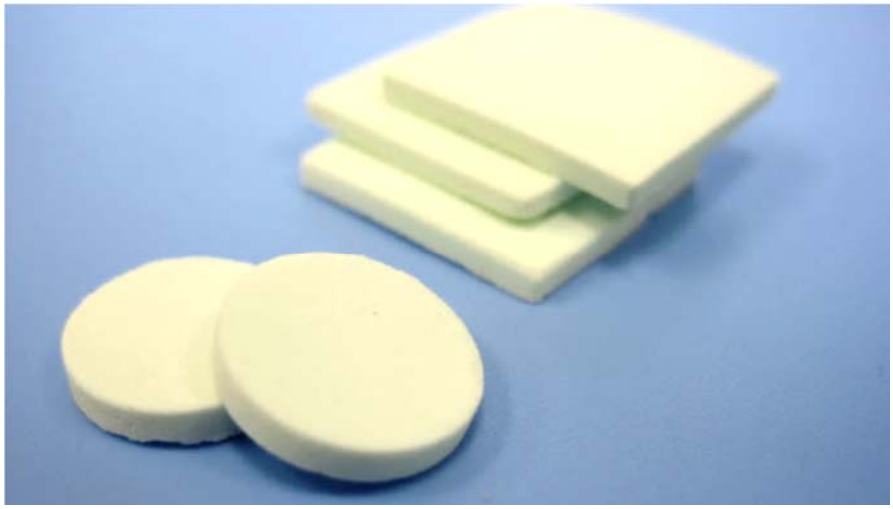

Figure 3.11: Photograph of $Y_2SiO_5:Pr^{3+}$ upconversion ceramic pellets and tiles.

Finally, virtually any type of UC phosphor system can be translated to ceramic form to achieve a solid, useable surface, without introducing new materials or altering phosphor composition. Future advances in phosphor composition may thus easily be incorporated into such a platform.

3.5. ACKNOWLEDGMENTS

This work was supported by The National Science Foundation (CBET #1033866) and the Korea Institute for Advancement of Technology (2011-GU-400115-001).

CHAPTER 4

STRATEGIES TO IMPROVE UPCONVERSION EFFICIENCY

4.1. Introduction

There exist countless studies on ways to improve luminescence efficiency—with regards to both upconversion and, more frequently, Stokes emission—from which we can gain insight into how we might improve the upconversion efficiency of Pr^{3+}-based phosphor materials. The previous chapter highlighted increased efficiency for UC ceramics compared to powder or thin-film types, though perhaps the more significant development was the introduction of an upconversion material that exhibited the structural characteristics required for surface application whilst maintaining its optical effectiveness. The 34-fold improvement in UVC emission under laser excitation was both intentional and encouraging, but the subsequent 3-fold improvement in spore inactivation under low-power lighting still fell short of our target—a more practically useful 10-fold improvement. In this chapter, we highlight the different methods we attempted to further enhance the efficiency of visible-to-UVC upconversion.

4.2. Sodium-doped ceramics

In our earlier work, the addition of lithium as a codopant in Y_2SiO_5:Pr powders was shown to increase the observed UC emission under 488 nm laser excitation by 9 times.[29] Though the valencies of Li^+ and Y^{3+} are mismatched by a 2+ charge, it was hypothesized and later experimentally confirmed that the main form of Li^+ incorporation into the host crystal was substitution for Y^{3+} ions, rather than as interstitial atoms. To balance the charge

mismatch, oxygen vacancies are formed, which appear to decrease the lattice parameters and encourage the denser polymorph of Y_2SiO_5 known as X2. The optimal Li^+ concentration for UVC UC was determined to be 10 mol.% (i.e. 1 out of every 10 mol of Y^{3+} are substituted by a mol of Li^+). The improvement in UC was attributed to crystallite enlargement via a flux effect, the encouragement of X2-Y_2SiO_5 polymorph at the 1000 °C calcining temperature, and a reduction of Pr^{3+} clustering.

Due to the anticipation of Li^+ evaporation when sintering the Y_2SiO_5:Pr^{3+} ceramics at 1300 °C, we speculated if another codopant could impart enhanced UC similarly to Li^+ and would not volatilize at this temperature, thus potentially being more effective for ceramics. Sodium ions (Na^+) have the same valency as Li^+ and are close enough in size (within 15%) to Y^{3+} such that substitution should occur.[59] However, Na^+ ions have larger ionic radii than Y^{3+}, whereas Li^+ ions are smaller than Y^{3+} (see Fig. 4.1 for all ionic radii); because of this, the use of Na^+ as a codopant could result in lattice distortion of different character and magnitude, even if the percentage and site distribution of Y^{3+} substitutions were equal.

Experimental. To test the effects of Na^+ doping, $NaNO_3$ (Sigma) was used to dope Na^+ into the Y_2SiO_5 host at 5 mol.%, 7 mol.%, 10 mol.% and 12 mol.% concentration, following the same sol-gel synthesis used for the Y_2SiO_5:Pr^{3+} powders (i.e. using $NaNO_3$ in place of $LiNO_3$; see Chapter 3). Sol-gel powders were annealed at 600 °C, uniaxially pressed at 100 MPa to form 10 mm pellets, and then sintered at 1300 °C in air to form ceramics. Powder mass was controlled prior to pressing to achieve a final ceramic thickness of approximately 1.2 mm, the same thickness as Y_2SiO_5:Pr^{3+} ceramics. Photoluminescence

spectroscopy was performed as previously described to obtain upconversion and Stokes emission spectra (see Chapter 3).

Results. The resulting ceramics varied unpredictably both in appearance and optical behavior. Pellets doped with 10 mol.% Na^+ were curved, with the upper concave sides typically light green in the center (typical for Pr^{3+}-doped materials) with an orange/brown outer area, and the bottom convex sides appearing yellow. The coloring was inconsistent between samples, however, and some batches appeared off-white or even had small white spots inexplicably located on the surface. Interestingly, the convex portion of the green-containing samples typically exhibited higher UVC upconversion than Li^+-doped ceramics and had the same luminescence curve, characteristic of X2-Y_2SiO_5:Pr^{3+} (shown in Fig. 4.2 (a)). The UC spectra of the same Y_2SiO_5:Pr^{3+},Na^+ pellets tested on the yellowed, concave side also resembled X2-Y_2SiO_5:Pr^{3+} but were considerably lower in intensity than Li^+-doped Y_2SiO_5:Pr^{3+}. When comparing the visible Stokes emission of Y_2SiO_5:Pr^{3+},Li^+ to the green portion of Y_2SiO_5:Pr^{3+},Na^+, shown in Fig. 4.2 (b), Li^+-doped phosphors were slightly brighter. This indicated that the Li^+ ceramics weren't necessarily inferior in terms of crystallinity and overall luminescence, but Stokes emission was more preferred over anti-Stokes (UC), possibly due to shorter excited state lifetimes. Pellets doped with 12.5 mol.% Na^+ appeared white and had lower UC emission than 10 mol.%-doped samples (not shown).

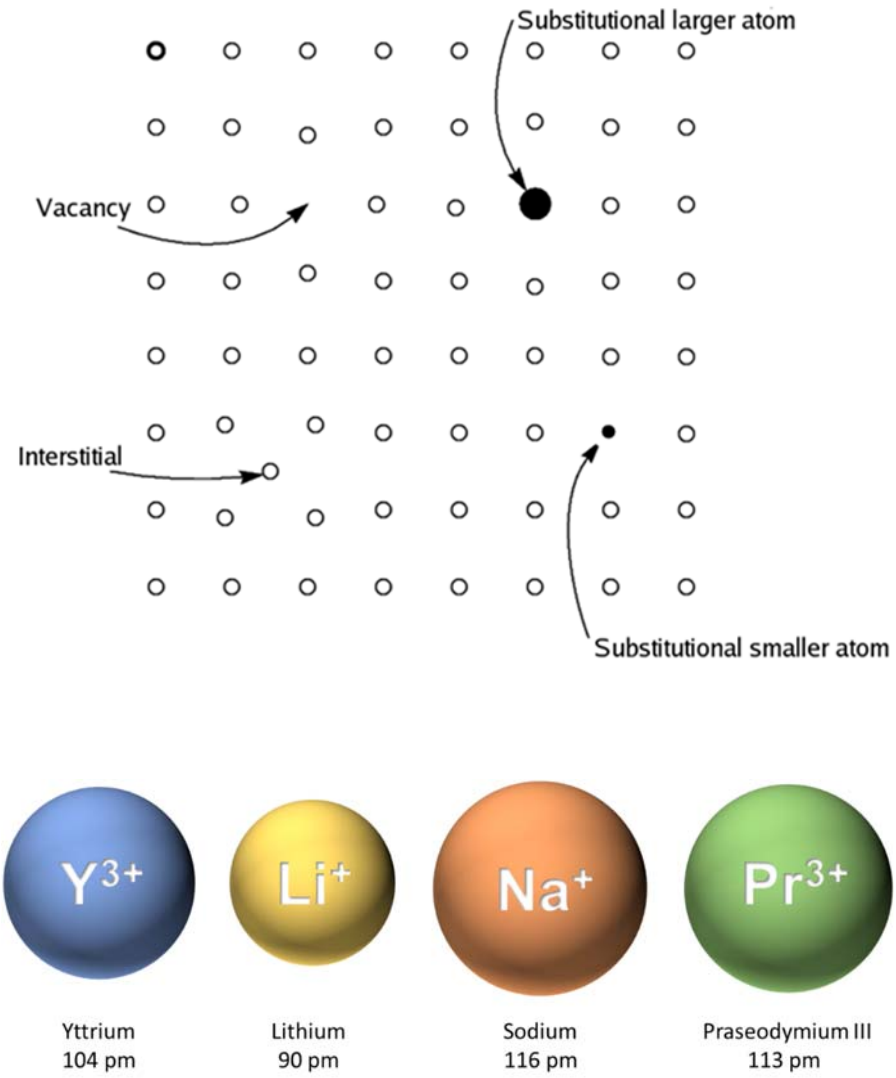

Figure 4.1: Top: Simplified diagram representing one plane of a crystal lattice (consisting of open circle atoms in repeating straight rows), showing how a lattice can be affected by different types of defects. When doping Y_2SiO_5 with Li^+, Y^{3+} is substituted by a smaller atom; with Pr^{3+} and Na^+, Y^{3+} is substituted by a larger atom. The aliovalent substitutions must be charge compensated, which has been shown to lead to O^{2-} vacancies ($\boldsymbol{V_O^{\cdot\cdot}}$).[29] (Image source: Public domain) Bottom: Schematic comparing the ionic radius of Y^{3+} to the radii of the substitutional dopant ions used in this work. Values from Shannon et al.[59]

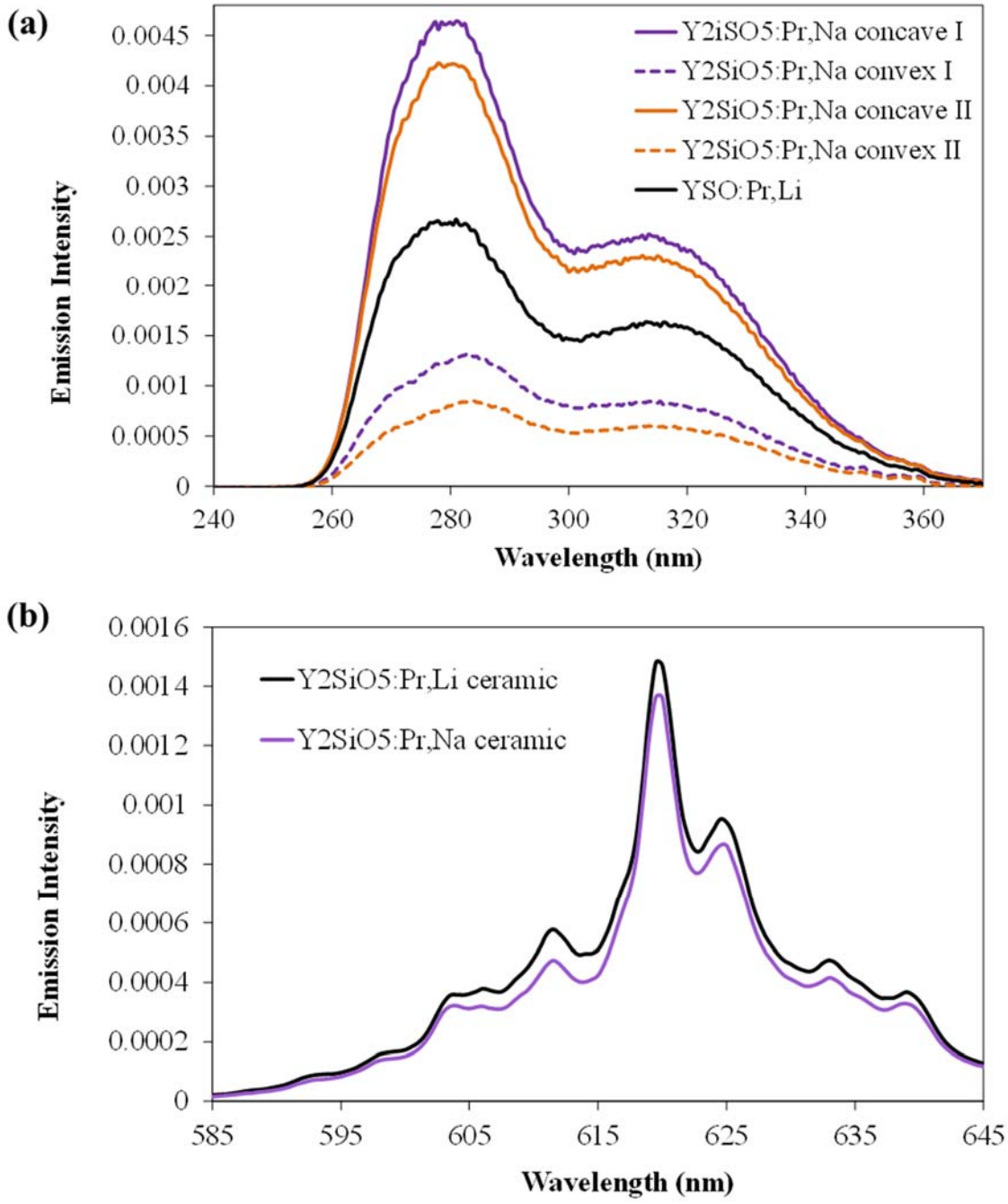

Figure 4.2: Photoluminescence spectroscopy depicting (a) UV upconversion spectra and (b) Stokes (visible emission) spectra, for $Y_2SiO_5:Pr^{3+}$ ceramics doped with 10 mol.% Na^+ compared to similarly prepared $Y_2SiO_5:Pr^{3+}$ ceramics doped with 10 mol.% Li^+. Laser excitation $\lambda = 447$ nm, power = 100 mW.

A possible explanation for the inhomogeneity of $Y_2SiO_5:Pr^{3+},Na^+$ ceramics could be ineffective incorporation of Na^+ into the host crystal. Due to their larger ionic radii, Na^+ may require higher energy to diffuse within the crystallites. Energy dispersive x-ray spectroscopy (EDX) analyzing each region (i.e. concave vs. convex side of each sample, differently colored areas) could be used to distinguish an imbalanced distribution of dopants. Sodium ions also have nearly identical radii to Pr^{3+}, and could thus be subject to similar clustering behavior that has been described for Pr^{3+} in this host material[29, 45]; they also might be less effective in dispersing those clusters, as it was suggested that the small size of Li^+ allows more space in the lattice for larger ions like Pr^{3+} to comfortably position in the proper sites. The cause for higher UC in certain areas of the Na^+-doped ceramics is unknown, though perhaps we do see improvement similar to Li^+ doping. Further analysis and varying of test conditions could likely determine what phases are appearing and how the homogeneity and phase purity of the pellets could be improved. If pellets could be made that were fully of the green phase we observed in some of the samples, which may require different sintering atmosphere or conditions, ceramic UC efficiency could be successfully enhanced.

Unfortunately, the inconsistencies in phase purity and luminescence made these samples difficult to understand and thus, difficult to optimize. Additionally, Na^+-doped powders were notoriously difficult to press into pellets. Green bodies often crumbled or cracked to the touch, even after optimizing applied pressure. Polymeric binders (PVA/H_2O) were used to aid green body formation, but the resulting pellets were covered in undesirable lumps and divots after burnout. The pellets which were pressed successfully were

especially brittle and fragile, making them undesirable for surface application. Therefore, despite the potential for higher UC, Na^+-doped ceramics were not pursued further.

4.3. Alternate phosphor syntheses

Sol-gel synthesis was chosen due to its straightforward procedure, relatively low heating requirements compared to solid state reactions, and the reliable homogeneity of the product; it is known, however, that sol-gel products typically suffer from widely dispersed particle size and a lack of controlled morphology. Other synthesis methods could perhaps result in phosphors with greater upconversion efficiency, higher crystallinity, monodispersity, and/or spherical morphology, which could be useful for coating and chemical modification.

Experimental. *COMBUSTION SYNTHESIS.* To synthesize $Y_2SiO_5:Pr^{3+}$ powders using a combustion method, aqueous solutions of $Y(NO_3)_3$, $Pr(NO_3)_3$, and $LiNO_3$ were first prepared using Y_2O_3 (Rare Earth Elements), $Pr(NO_3)\cdot 6H_2O$, (Sigma Aldrich) and $LiNO_3$ (Sigma Aldrich). These were combined according to the stoichiometry $Y_{(2-x-y)}Pr_xLi_ySiO_{(5-y)}$ and dried in an oven at 104° C. The nitrates were then redissolved in 15 mL of DI water before adding urea or glycine (both from Sigma Aldrich, added using 30% fuel-rich stoichiometry) and a stoichiometric amount of fumed silica (7 nm, Sigma Aldrich). The mixtures were stirred and gelled on a hot plate for 18 h at approximately 60 °C. The soft, slightly translucent gels were transferred to alumina crucibles and placed in a muffle furnace pre-heated to 550 °C. Combustion occurred within the first 10 minutes of heating, after which the crucibles were removed and cooled in air. The powders (expanded and gray for glycine combustion, compacted and off-white for urea) were then ground and annealed

in a tube furnace at 1300 °C for 2 h in air to obtain $Y_2SiO_5:Pr^{3+}$. An optimal doping concentration of 1.2 mol.% Pr^{3+} and 7.2 mol.% Li^+ was determined and used for subsequent experiments.

ULTRASONIC SPRAY PYROLYSIS (USP). A spray pyrolysis method was developed to synthesize spherical $Y_2SiO_5:Pr^{3+}$. Precursor solutions were prepared by mixing aqueous solutions of $Y(NO_3)_3$, $Pr(NO_3)_3$, $LiNO_3$, and TEOS following the stoichiometry $Y_{1.89}Pr_{0.01}Li_{0.10}SiO_{4.9}$, as used in previous work.[1] The solution was diluted to a concentration of 1 mmol/L and 10 mL was placed in the basin of an ultrasonic spray generator (a household humidifier), with vapor outlet fitted to one end of a quartz tube furnace. After preheating the furnace to 600 ºC, the vaporized particles were pumped through the tube, in air, and collected at the outlet on a 0.2 μm filter. The spray generator was set to the lowest setting to increase particle residence time in the furnace. All fittings and connections were carefully wrapped in parafilm to prevent loss of pressure in the system, except for the ends which directly connected to the hot quartz tube, which were secured with clamps. For full schematic of the ultrasonic spray pyrolysis setup, see Fig. 4.3. Filters containing reacted powders were dried to fully recover the powders, which were then calcined at 1000 °C for 3 h in air. Powders were cooled at room temperature and ground before use.

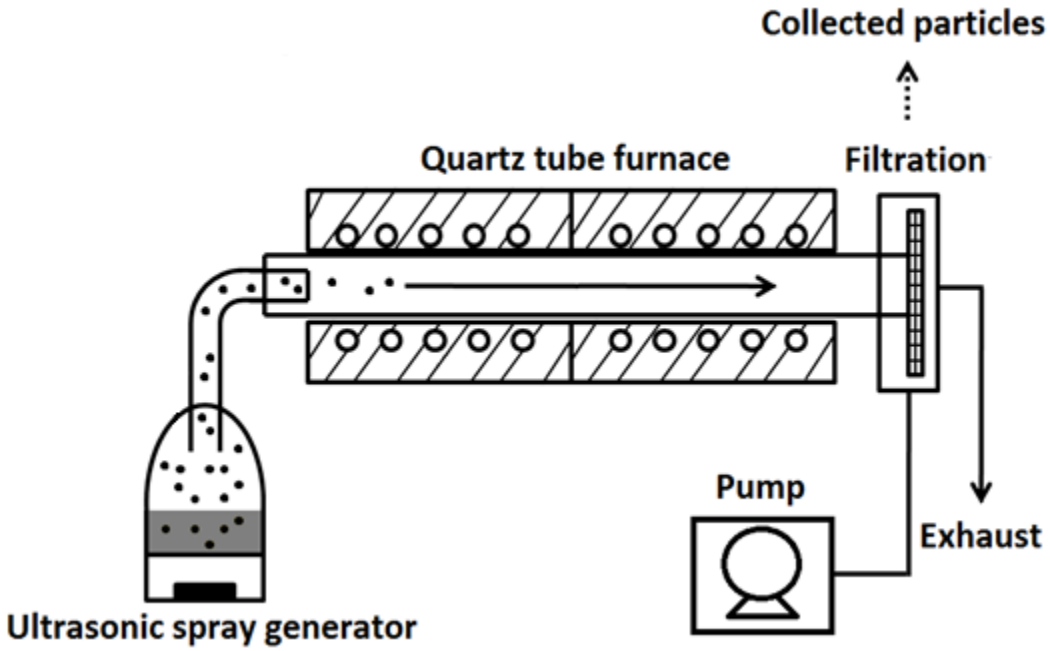

Figure 4.3: Schematic of ultrasonic spray pyrolysis setup. Precursor phosphor solution is placed in the ultrasonic spray generator basin, and a pump pulls the vaporized particles through a preheated tube furnace. Reacted particles are collected on a filter located just past the heated tube.

Results. *COMBUSTION SYNTHESIS.* This method resulted in more discrete particles but lower phase purity compared to sol-gel powders (see XRD in Fig. 4.4, which shows a mixture of X1 and X2 phase Y_2SiO_5). Upconversion emission, as measured using PLS and shown in Fig. 4.5, was consequently much lower than the optimized sol-gel $Y_2SiO_5:Pr^{3+}$. The resulting particles are smaller in size than sol-gel phosphors, however, which could be useful for any application that benefits from higher surface area.

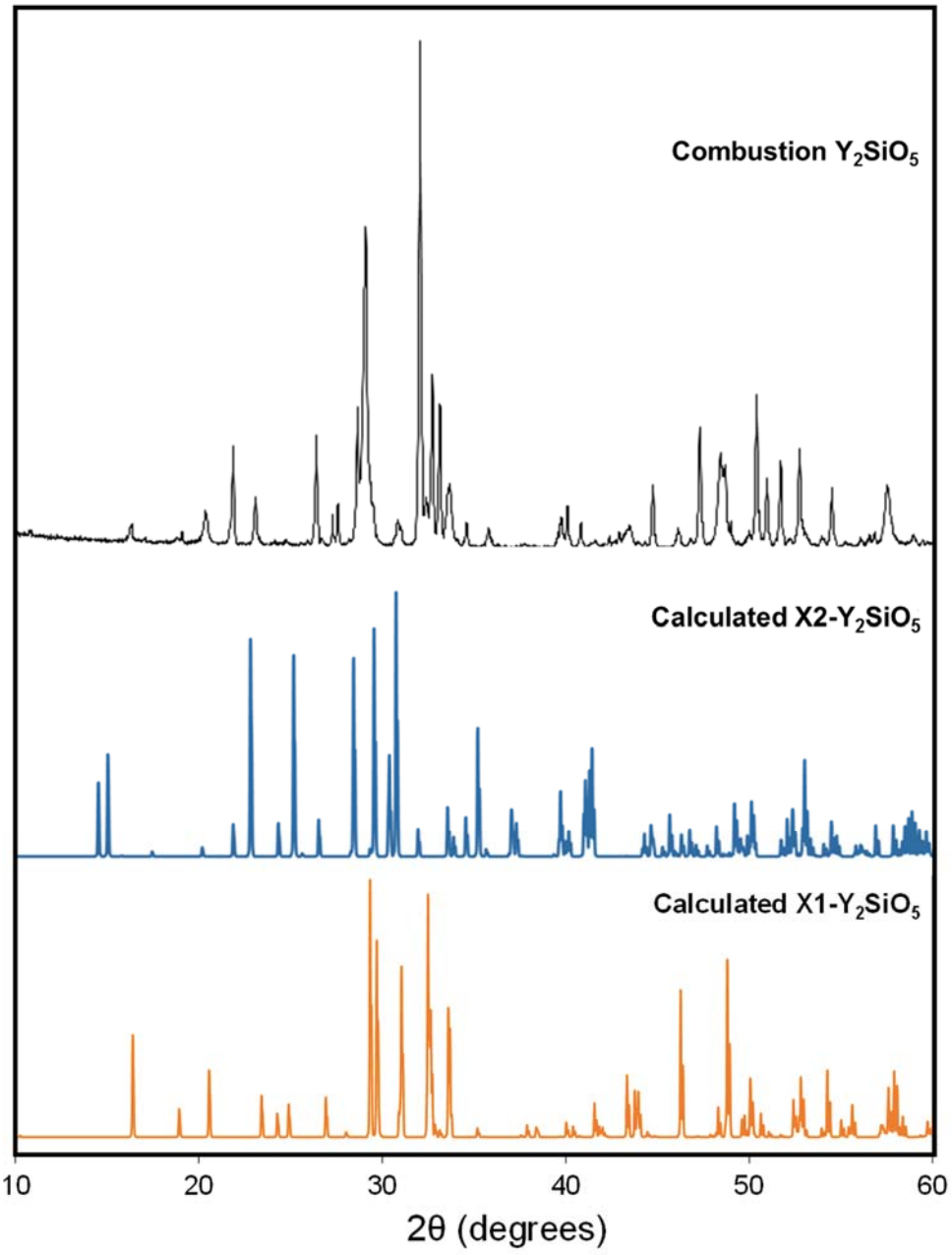

Fig. 4.4: XRD for combustion powders made using glycine fuel; compared to calculated patterns for X1 and X2 Y_2SiO_5.

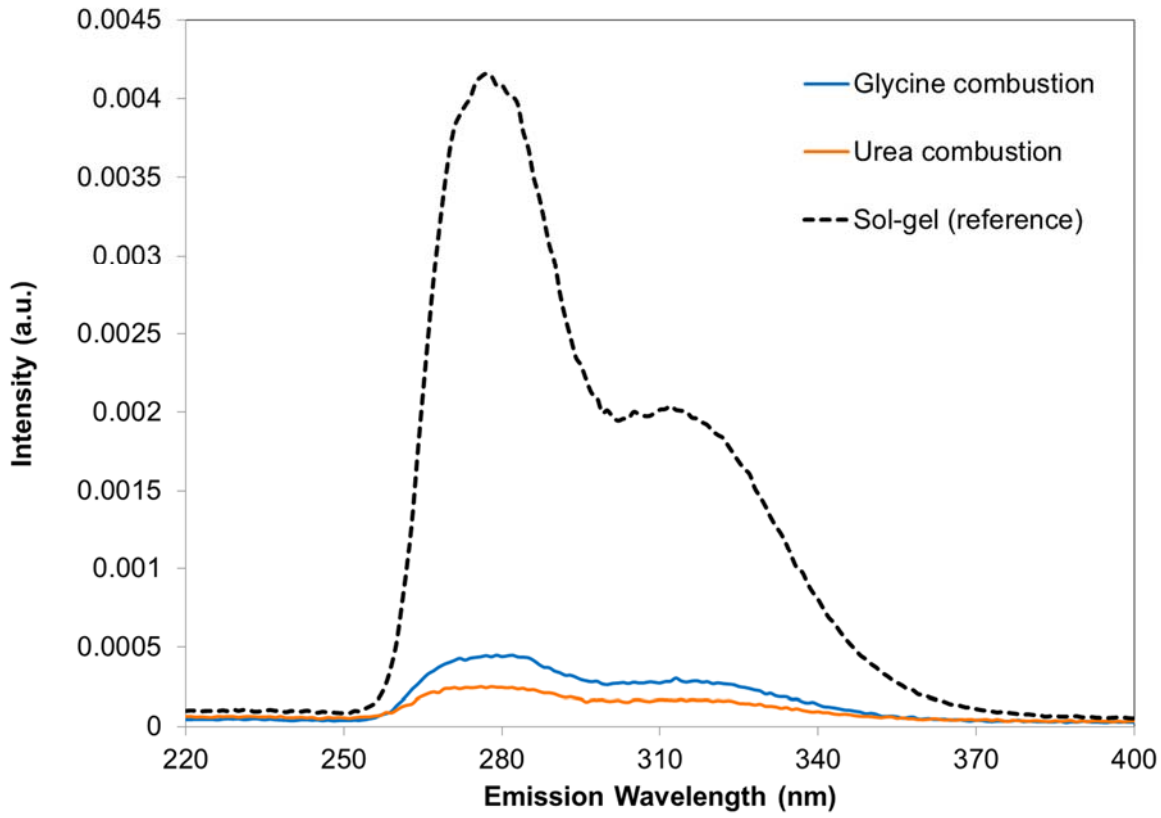

Figure 4.5: PLS showing upconversion emission intensity for combustion $Y_2SiO_5:Pr^{3+}$ phosphors synthesized using glycine and urea fuel, compared to reference powder from sol-gel synthesis.

ULTRASONIC SPRAY PYROLYSIS. An ultrasonic spray pyrolysis (USP) method was developed to achieve spherical particles. Phosphors produced using USP were spherical, with minimal aggregation and a moderate size distribution. Particle sizes ranged from 0.2-2 μm, the smallest of which correspond to the filter size used to collect the particles, which likely aided in narrowing the distribution. $Y_2SiO_5:Pr^{3+}$ particles before and after annealing at 1000 °C are shown in Fig. 4.6.

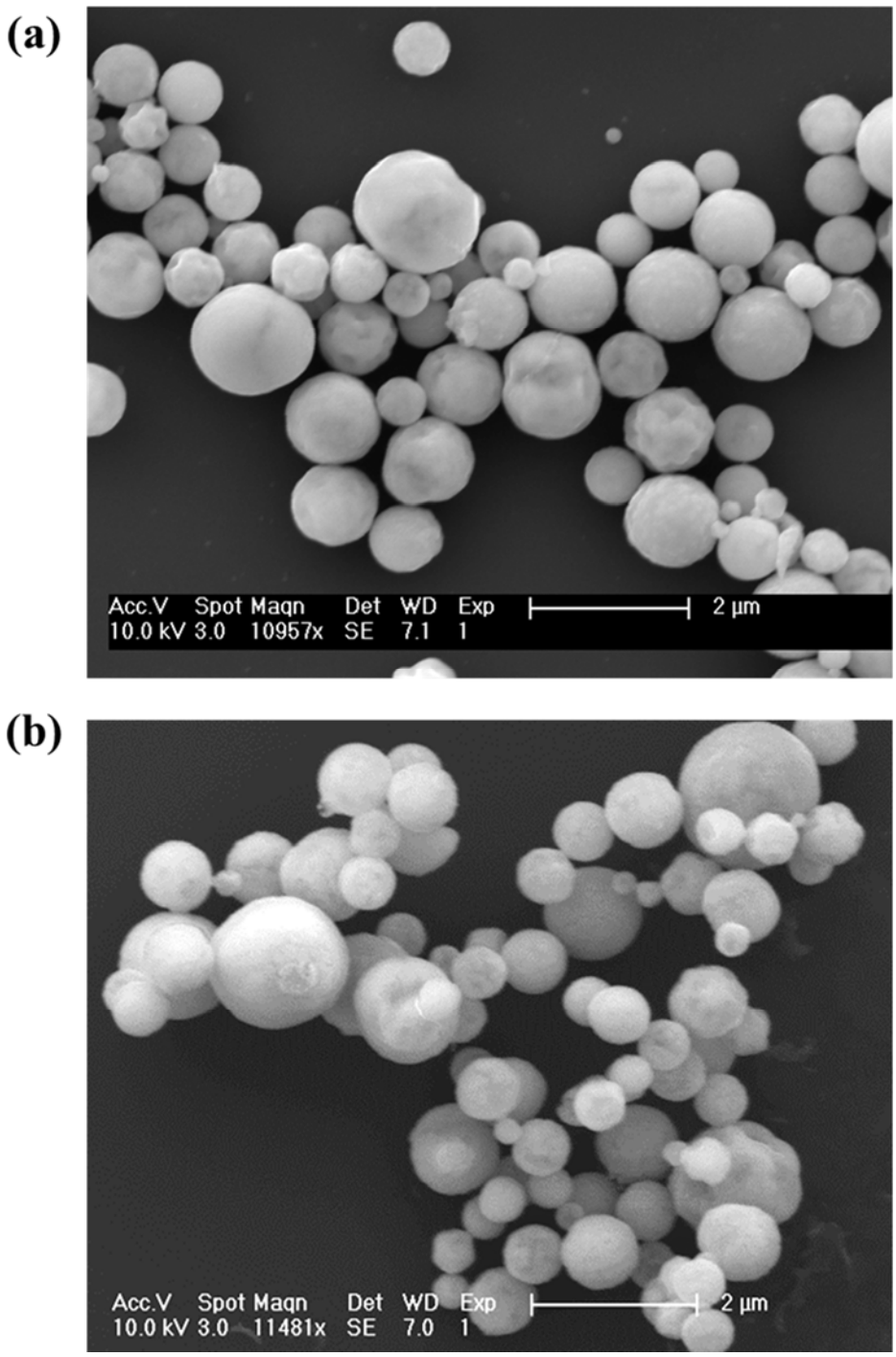

Figure 4.6: SEM images of $Y_2SiO_5:Pr^{3+}$ particles produced using ultrasonic spray pyrolysis, (a) before and (b) after annealing.

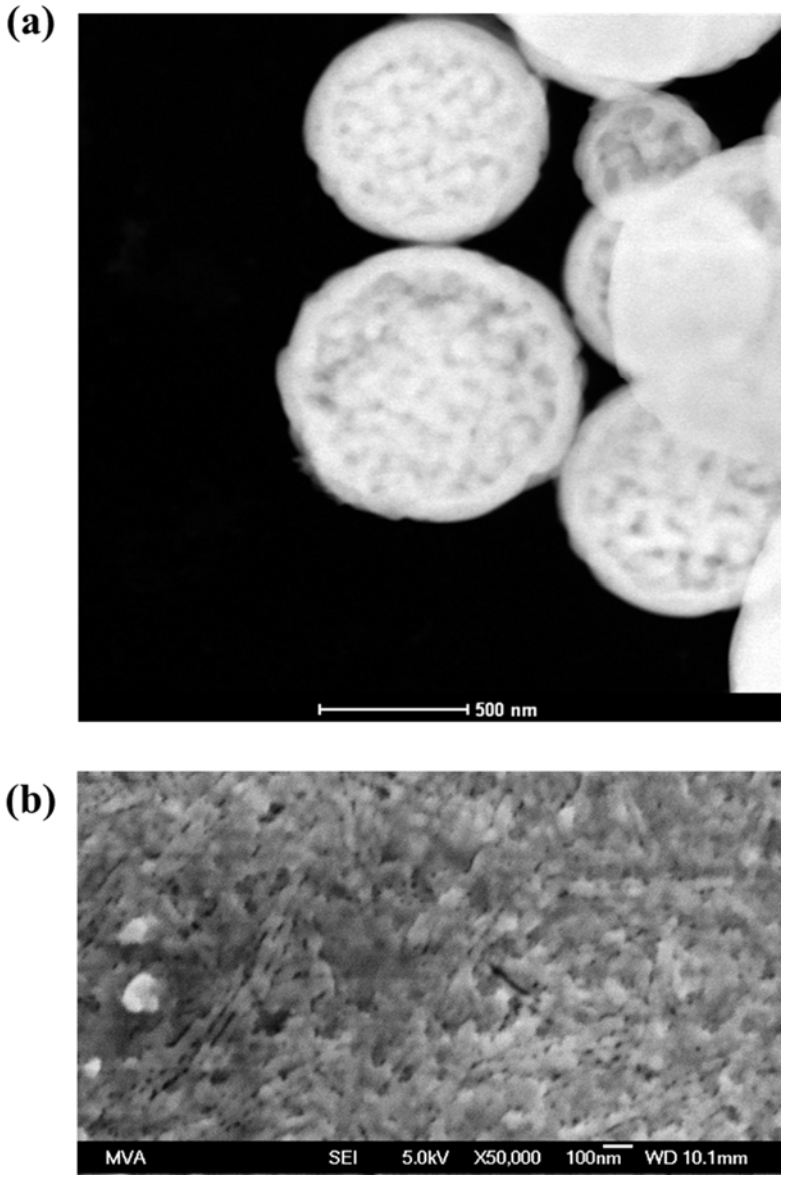

Figure 4.7: (a) TEM HAADF image of X1-Y_2SiO_5:Pr^{3+} from ultrasonic spray pyrolysis, showing spherical particles consisting of smaller crystallites and pores, and (b) SEM image of X1-Y_2SiO_5:Pr^{3+} from sol-gel synthesis, which also indicates small crystallite size.

Interestingly, while both USP and sol-gel precursors contained the same amount of Li^+ additive (which has been shown to lower the calcination temperature for X2-Y_2SiO_5)[29] and were subject to identical calcination treatment, ultrasonic spray pyrolysis produced the X1 polymorph of Y_2SiO_5 (see XRD in Fig. 4.8) while the sol-gel decomposition produced the thermodynamically preferred X2 polymorph (see Chapter 3 for luminescence and XRD characterization). This phase was indicated by red-shifted photoluminescence spectra (Fig. 4.9) and also by the crystallite size; crystallites for USP particles appeared to be much smaller than for sol-gel phosphors, as evident under TEM (Fig. 4.7a), which was characteristic of the X1-Y_2SiO_5 polymorph (Fig. 4.7b). Further annealing at 1300 ºC did transform the material to the X2-Y_2SiO_5:Pr^{3+}, but the resulting emission was much weaker than sol-gel X2-Y_2SiO_5:Pr^{3+} (see Fig 4.9). The overall intensity of UV emission for X1 USP particles was comparable to the sol-gel phosphors; see Chapter 5 for PLS (Fig. 5.6) and further discussion.

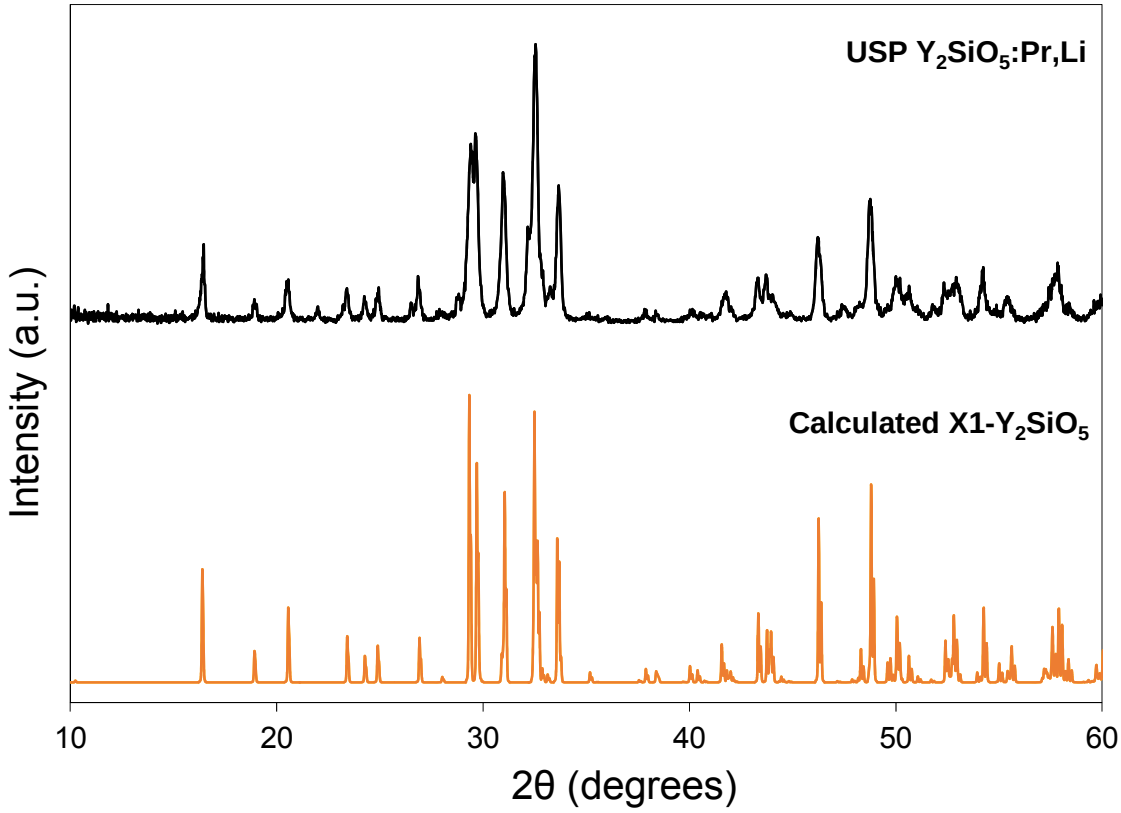

Figure 4.8: X-ray diffraction pattern for $Y_2SiO_5:Pr^{3+}$ powders prepared using ultrasonic spray pyrolysis, showing preferred crystallization into the X1-Y_2SiO_5 polymorph.

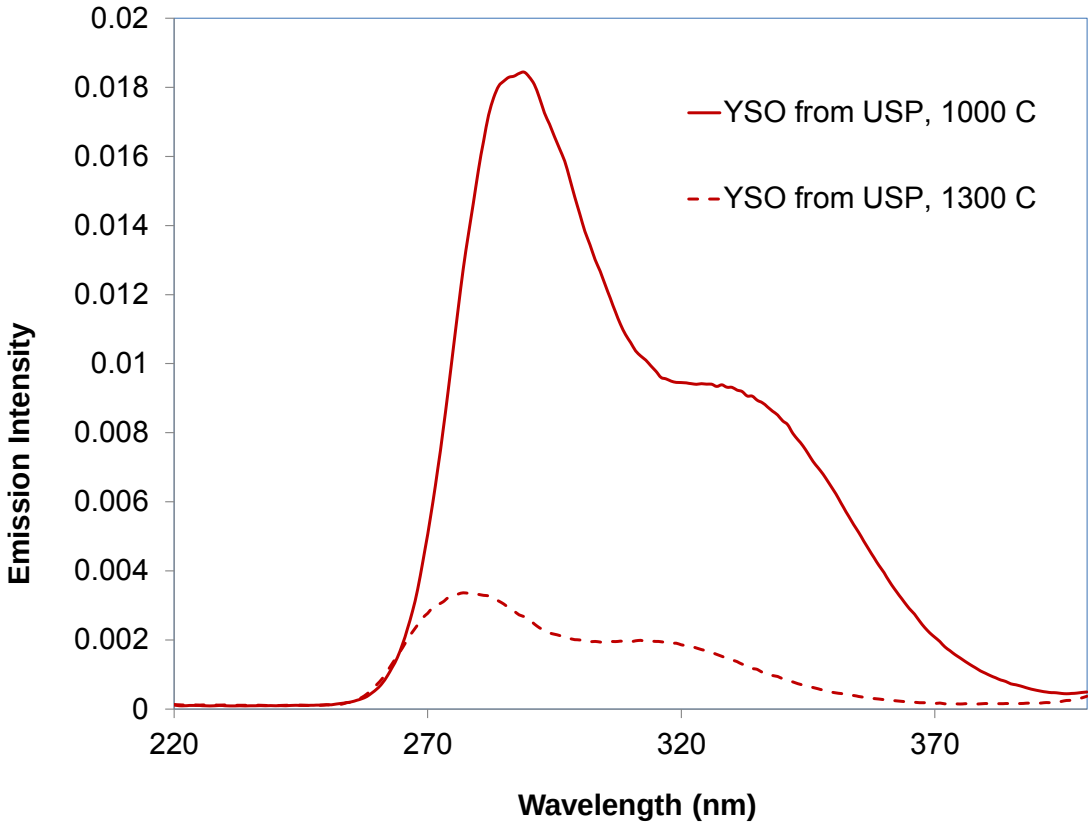

Figure 4.9: Photoluminescence spectroscopy depicting UC emission from USP $Y_2SiO_5:Pr^{3+}$ before and after annealing at 1300°C.

One of the primary advantages of USP is the ability to control particle size and morphology, enabling better optimization of their properties for a specific application. Though particle sizes remained dispersed here, a narrow distribution could be obtained by filtering the particles further or by using a more sophisticated experimental setup with higher reaction temperature and controlled system pressure (our instrumental setup consisted of plastic connectors which could not withstand furnace temperatures > 600 °C, which has been shown to produce more uniform and crystalline materials;[60] in addition, there existed points of pressure leakage, particularly at the ends of the heated elements, which were subject to temperatures too high for our sealant material to be used). The resulting spherical particles would be better suited for modifications or applications which involve functionalizing and/or coating the phosphors, since the thickness and concentration of these coatings could be better controlled on homogeneously spherical surfaces. With further optimization of optical properties, perhaps by using higher reaction temperatures or producing more dense spheres (see discussion in Chapter 5), USP $Y_2SiO_5:Pr^{3+}$ could thereby have many benefits over sol-gel phosphors for environmental application.

4.4. Dye sensitized upconversion

In 2012, it was reported that coating phosphors with dye to achieve Förster resonance energy transfer (FRET) had effectively increased the absorptivity of NIR-to-visible upconversion particles by several orders of magnitude.[5] The effect was termed dye sensitized upconversion. While this magnitude of improvement is unlikely with micron sized phosphors, which are necessary for visible-to-UVC application, it nonetheless introduced a promising tool to achieve much higher UC under low-intensity light conditions.

Dye sensitization relies on close proximity between a dye molecule and an UC particle; if the dye absorbs strongly at the excitation wavelength and emits light within the excitation range of the nearby UC particle, the dye can act as a sensitizer in the UC process. This increases the amount and also the range of light absorbed by the phosphor. It is well known that upconversion materials typically suffer from low absorption coefficients.[2] In addition, most of the energy that is absorbed is lost either to non-radiative relaxation processes or Stokes emission, meaning only a small portion of incoming light can participate in upconversion.

Figure 4.10 shows schematically how energy is transferred between a donor and acceptor chromophore in FRET. The dye molecule, or donor, acts like an antenna to absorb incoming light (blue arrow). Rather than emit this energy via fluorescence (green arrow), this energy can be transferred to a neighboring phosphor molecule, which is the acceptor. The acceptor then becomes excited and can undergo the same luminescence processes as if it had just absorbed a photon of that energy (black dotted arrow).

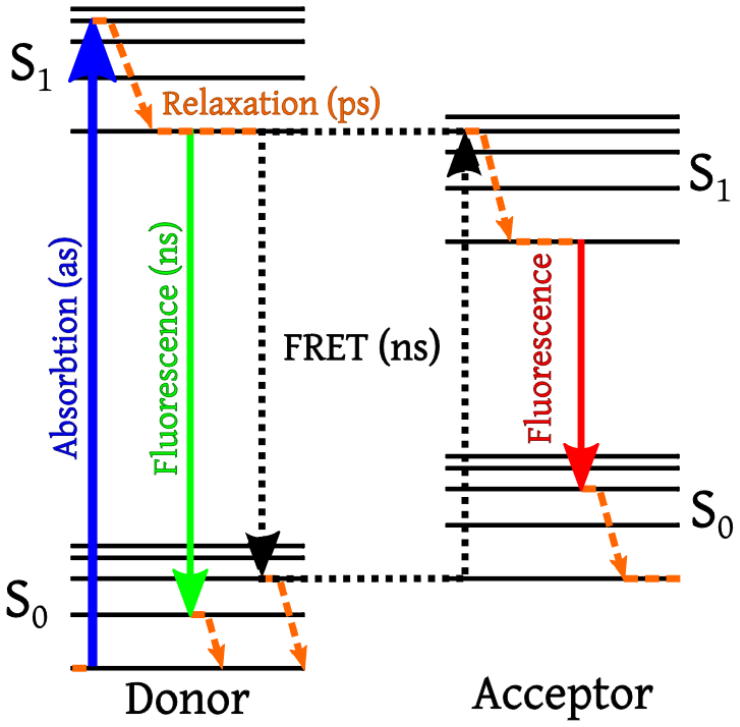

Figure 4.10: Energy level diagrams depicting Förster resonance energy transfer between a donor and acceptor chromophore. Source: Alex M. Mooney

To choose the appropriate dye to act as a donor for our phosphors, we must consider the requirements for successful FRET:

- ***Minimum distance between donor and acceptor.*** The donor and acceptor must be in close proximity; the optimal distance depends on the specific species being used, but is typically less than 10 nm.[61]
- ***Adequate spectral overlap.*** The emission of the donor must coincide with the absorption of the acceptor (i.e. the excitation spectrum of our phosphor, shown in Fig. 4.11). The overlap should not be so great, however, that reverse FRET (transfer of energy back to the donor) becomes probable.
- ***Approximately parallel dipole moments.*** In contrast to Dexter electron transfer, where an electron is being transferred from donor to acceptor, FRET involves energy transfer through dipole-dipole coupling. The orientations of the donor and acceptor, however, are often unknown.[62]

If the minimum requirements of FRET are met, the distance between donor and acceptor become most important. Förster derived the following relationship describing the efficiency of FRET (E_{FRET}):[63]

$$E_{FRET} = R_0^6/(R_0^6+r^6)$$

Where r is the separation distance between the donor and acceptor, and R_0^6 is the Förster radius at which 50% efficiency is achieved. From this we see that E_{FRET} is proportional to r^{-6}, meaning the efficiency will decrease at a steep exponential rate as the donor/acceptor separation is increased. Zou et al. reported that only chemically attaching dye to their phosphors resulted in FRET; simply mixing the two together did not result in the close

proximity and strict control of r that was necessary for successful FRET.[61] Other factors to consider for an optimal system include:

- ***Appropriate amount of dye.*** Too high of a concentration can lead to self-quenching between dye molecules. Excess dye can also absorb light but not have a nearby phosphor to transfer that energy to.
- ***Minimal absorption by donor of emission from acceptor.*** For visible-to-UVC phosphors, our main concern is that the dye does not absorb the UVC emitted (for X2:Y_2SiO_5:Pr^{3+} the UC emission peak is ~276 nm). Since our phosphors absorb most efficiently in blue-violet wavelengths, this requires that the dye has a narrow spectral shift.

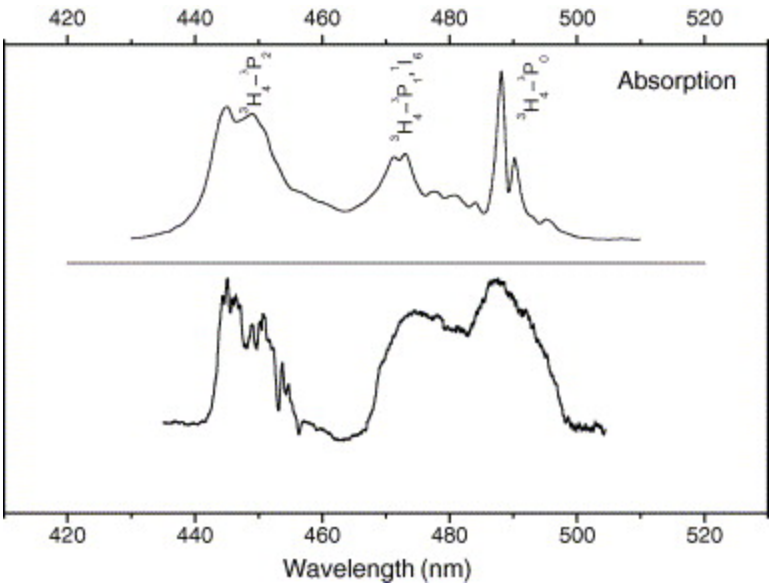

Figure 4.11: Absorption (top) and excitation (bottom) spectra for single crystal X2: Y_2SiO_5:Pr(1%), obtained by Hu et al.[31] Excitation spectra were collected by measuring UC emission at 280 nm. Excitation spectra are measured by detecting the intensity of a fixed emission wavelength over a range of irradiation energies; here, each region of the excitation spectra represents a different Pr^{3+} transition (labeled). From this we can see which excitation energies (i.e. which donor molecule emission energies) are most readily absorbed by Pr^{3+} and are most useful for UC.

Experimental. Three dyes were selected for dye sensitization of $Y_2SiO_5:Pr^{3+}$: coumarin 343 (Sigma Aldrich), 7-hydroxy-4-methylcoumarin (coumarin 4; Sigma Aldrich), and Pacific Blue™ (Invitrogen), based on the requirements described above. Absorption and emission spectra for each dye were measured using UV-Vis spectroscopy and spectrofluorimetry, respectively, the latter using 447 nm excitation (chosen to equal the λ_{ex} used to excite Y_2SiO_5:Pr in PLS). Approximate peak absorption ($\lambda_{abs,max}$) and emission ($\lambda_{em,max}$) values are listed in Table 4.1.

Table 4.1: Chemical structures and peak absorption (within visible) and emission (λ_{ex} = 447 nm) values for the 3 dyes used, as measured using aqueous dye solutions, pH = 7.

Dye	Chemical structure	$\lambda_{abs,max}$	$\lambda_{em,max}$
Coumarin 343	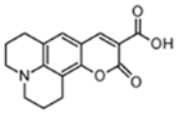	446 nm	490 nm
Coumarin 4	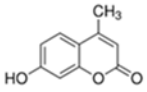	370 nm	448 nm
Pacific Blue™	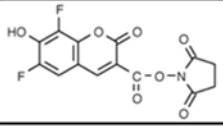	338 nm	458 nm

Phosphor synthesis. Y_2SiO_5 powders doped with 10 mol.% Pr^{3+} and 7.2 mol.% Li^+ were synthesized using a combustion method. Aqueous solutions of $Y(NO_3)_3$, $Pr(NO_3)_3$, and $LiNO_3$ were first prepared using Y_2O_3 (Rare Earth Elements), $Pr(NO_3)\cdot 6H_2O$, (Sigma Aldrich) and $LiNO_3$ (Sigma Aldrich). These were combined according to the stoichiometry $Y_{(2-x-y)}Pr_xLi_ySiO_{(5-y)}$ and dried in an oven at 104° C. The nitrates were then redissolved in 15 mL of DI water before adding urea (Sigma Aldrich, added using 30% fuel-rich stoichiometry) and a stoichiometric amount of fumed silica (7 nm, Sigma Aldrich). The mixtures were stirred and gelled on a hot plate for 18 h at approximately 60 °C. The soft, slightly translucent gels were transferred to alumina crucibles and placed in a muffle furnace pre-heated to 550 °C. Combustion occurred within the first 10 minutes of heating, after which the crucibles were removed and cooled in air. The compacted, off-white powders were then ground and annealed in a tube furnace at 1350 °C for 2 h in air to obtain $Y_2SiO_5:Pr^{3+}$.

Silylation. Phosphor particle surfaces were functionalized with amine groups using a straightforward silylation method. Powders were dispersed in ethanol, then APTES was added. The mixture was stirred over low heat for 10 minutes before stopping the reaction with the addition of acetic acid. The mixture was centrifuged and washed three times in ethanol to recover powders.

Dye coating. Functionalized phosphor powders were dispersed in ethanol before adding desired amount of dye powder. Mixtures were stirred at room temperature overnight for adsorption of dyes to phosphors to occur. Solutions were then centrifuged and washed three times in ethanol to recover dye-coated powders.

Materials characterization. $Y_2SiO_5:Pr^{3+}$ phosphors were characterized using XRD and photoluminescence spectroscopy, confirming X2 phase and characteristic upconversion emission curve, respectively. Dynamic light scattering was used to estimate an average particle size of 1.25 μm, though particle sizes were dispersed from 0.25 to 3.75 μm. Emission spectra for dyes suspended in ethanol were recorded using a spectrofluorimeter and then compared to dye-coated phosphors in ethanol, to confirm dye attachment to phosphors. Upconversion luminescence was measured using photoluminescence spectroscopy, as described previously. Both Stokes emission and upconverted emission were measured for dye-coated and uncoated phosphors.

Results. Photoluminescence spectroscopy was conducted using a 447 nm laser to observe the effects of dye coating on upconversion emission. Unfortunately, no enhancement in UC emission was observed for $Y_2SiO_5:Pr^{3+}$ phosphors coated with coumarin 343 or Pacific Blue™, despite the apparent spectral match for these dyes with the phosphors. Both dyes resulted in slightly lower UC emission intensity compared to uncoated phosphors at all laser intensities tested (results for Pacific Blue™ shown in Fig. 4.12), though the difference lessened with lower excitation intensity. Coumarin 343 was expected to enable the highest enhancement due to a much greater absorption coefficient at the excitation wavelength (447 nm) compared to the other dyes. That noted, coumarin 343 emission is centered at approximately the same energy as the lowest Pr^{3+} $^3P_0$ levels, which may lead to inefficient FRET. The absorption spectra of Pacific Blue™ showed only the slightest overlap with 447 nm (most absorption at shorter λ), which could explain the absence of apparent FRET. It is even possible that the absorbance was further blue-shifted when attached to the phosphors, similar to what was reported by Zou et. al. [5]

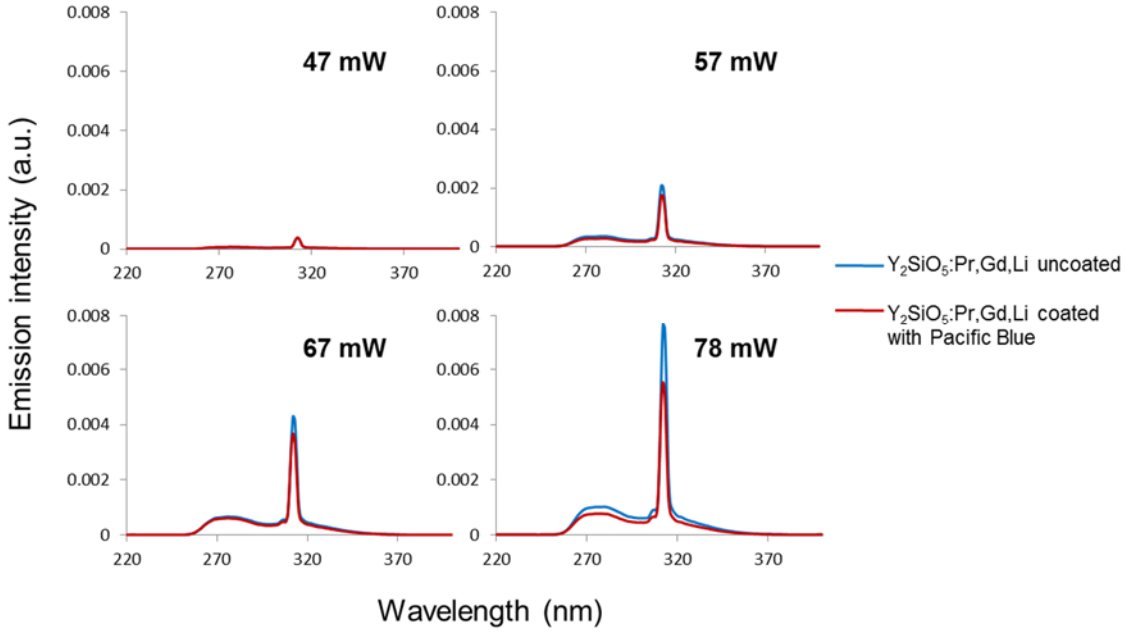

Figure 4.12: Photoluminescence spectroscopy depicting upconverted UVC and UVB emission for Pacific Blue™-coated Y_2SiO_5:Pr,Gd,Li phosphors.

Positive results were observed when coating the phosphors with coumarin 4, which was the only dye that resulted in more intense upconversion luminescence compared to uncoated phosphors (see PLS in Fig. 4.13). Though this dye did not exhibit measurable absorption of 447 nm when tested alone (in H_2O and in EtOH), it appears that some visible absorption occurs when the dye is coated onto our phosphors, apparent by a pale yellow coloring (quantitative absorption data for the as-coated dyes would require diffuse reflectance spectroscopy, which was not available to us during this time). Thus it was possible that the dye was transferring energy via FRET to the phosphors under 447 nm excitation, resulting in the increase in UVC emission seen in PLS. Because the primary absorption peak of coumarin 4 coincides with the UVB emission peak of the phosphor, ~320 nm, there was an accompanying decrease in the UVB emission peak. Of note, these results were seen 4 separate times when coating the phosphors with this dye (sometimes with slightly larger enhancement than seen in Fig. 4.7), which indicates that the slight apparent enhancement in upconverted UVC is indeed due to the presence of dye, rather than random experimental variation.

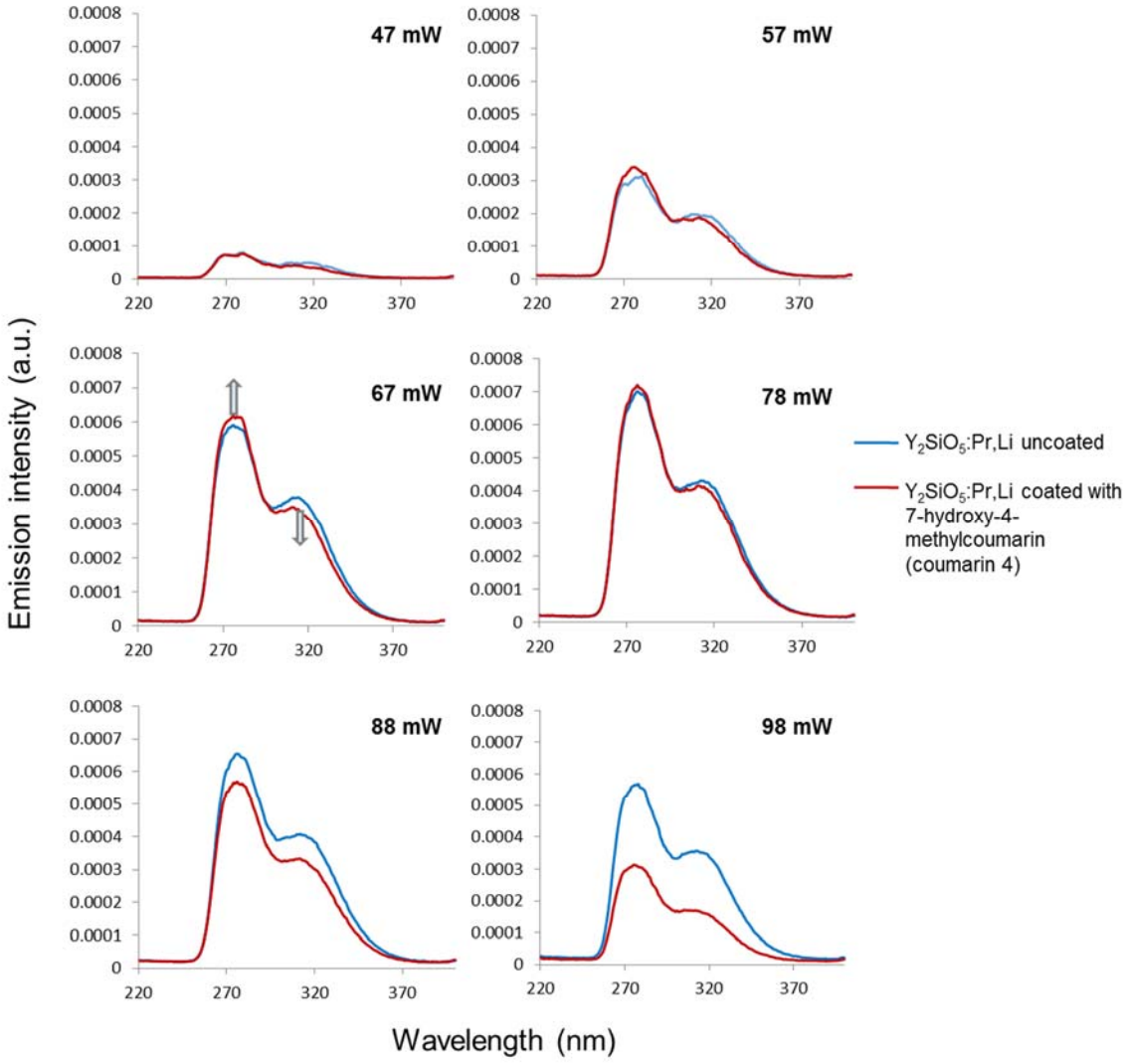

Figure 4.13: Upconverted luminescence from coumarin 4-coated $Y_2SiO_5:Pr^{3+}$ (red) compared to the same phosphor without dye coating (blue), measured under 447 nm laser excitation at different laser power levels.

Emission for coumarin 4-coated and uncoated $Y_2SiO_5:Pr^{3+}$ were measured at 6 different excitation intensities in the range of 47-98 mW. The dye-sensitization enhancement became less significant as the excitation intensity increased, and somewhere above 78 mW the dye-coated phosphors become less efficient than the uncoated phosphors. This could be due to photobleaching of the dye by the more powerful laser light. A suggested mechanism of photobleaching is intersystem crossing of excited fluorophore electrons from the singlet to triplet excited state, from which fluorescence can no longer occur. Thus, electrons are still being absorbed by the dye but cannot contribute to fluorescence or energy transfer to the phosphors, causing a decrease in the phosphor emission by effectively removing a portion of the excitation energy. Though we would expect photobleaching over time for dye-coated phosphors under ambient lighting, the phosphors themselves would still function without dye, and the reaction should be significantly slower than what we would observe under high laser intensity. Indeed, the laser power used by Zou et al. to show enhanced emission was only 2 mW, far below the excitation power required to achieve measurable UVC emission from our samples (47 mW). While IR-to-visible UCPs are typically more efficient than visible-to-UVC materials, the main hindrance to obtaining such low-intensity excitation data is the lack of detection equipment with high sensitivity to UV radiation.

Since the coumarin 4 dye, along with the others tested here, is expected to have some absorption of all UV wavelengths (i.e. UVC included), it is possible that the UC enhancement due to FRET even greater than what was observed with PLS. That is, since the dye is likely absorbing a portion of the UVC emitted by the phosphors, we would expect the amount of UVC actually emitted to be even higher than what was measured, due to

successful FRET. This observation can further be extended to the experiments using coumarin 343 and Pacific Blue; even if FRET were occurring in these samples, it might not be observable due to more prominent absorption of UV by the dyes. While this UV absorbance would be a limitation for dye sensitization of any UV-emitting phosphor, we expect that the enhancement due to successful FRET, achieved using the optimal dye, would outweigh the negative effects of dye absorption.

Despite the modest level of UC improvement achieved by coating the phosphors with coumarin 4 dye, the ability for dye sensitization to be used with visible-to-UV UC materials introduces an exciting possibility of enhanced UC under broadband excitation. While $Y_2SiO_5:Pr^{3+}$ can absorb a range of visible light wavelengths (see this reference[28] for further discussion of polychromatic excitation in $Y_2SiO_5:Pr^{3+}$), which is important when considering the broadband light sources in our target applications, dyes are known to have wider absorption bands and significantly higher absorption coefficients. It is not unimaginable that a dye better matched to these phosphors could lead to UC enhancements of a magnitude or more, especially under low intensity excitation.

Dyes can also be tailored to a certain extent to achieve the optimal spectral match. Ideally for sensitization of $Y_2SiO_5:Pr^{3+}$, a dye would absorb below the energy of emitted UVC and above the $^3P_0$ state of Pr^{3+}, minimizing the absorption of UV and also the reverse FRET from excited ^3P_J states back to the dye. Using the known band energies of Pr^{3+}, the optimal dye would thus have maximum absorption between 410–430 nm and emission between 460–465 nm. None of the dyes we used or have seen in the literature have these exact characteristics, and indeed this ideal dye has an uncommonly narrow spectral shift. We have discovered, however, that the absorption and emission spectra for many marketed

dyes are not fully documented, and certain dyes will exhibit unique absorption and emission behavior when bound to a different material or dispersed in a different solvent. Thus, finding the optimal dye for any phosphor may require a combination of trial and error and/or chemical modification of available dyes.

4.4. Conclusion

Several materials modification strategies were employed to achieve higher upconversion luminescence from $Y_2SiO_5:Pr^{3+}$ phosphors. Sodium doping was used specifically to improve the UC in ceramics, in an effect similar to Li^+ doping, but the inhomogeneity and fragility of the resulting ceramics outweighed the improvements in UVC emission achieved in some samples. New synthesis methods—combustion and ultrasonic spray pyrolysis—did not produce phosphors with higher UC emission than the previously optimized $Y_2SiO_5:Pr^{3+}$ made using sol-gel synthesis. Spray pyrolysis, however, was able to produce spherical particles that could be advantageous for other materials enhancement strategies, such as core-shell systems. Finally, dye sensitization was employed to achieve higher visible light absorption through Förster resonance energy transfer from the dyes to the $Y_2SiO_5:Pr^{3+}$ phosphors. Slight enhancement in upconverted UVC was observed by coating the phosphors with coumarin 4, despite the fact that this dye did not have optimal spectral mismatch with the phosphor. Evidence of successful energy transfer using coumarin 4 suggested that, should the optimal dye be found, dye sensitization could indeed lead to achieve significant UC enhancement with these phosphors.

4.5. Acknowledgments

We would like to thank Dr. Felix Castellano (now at NC State University) and Dr. Vincent Chen and Dr. Tim Parker from Georgia Tech for their advice and assistance for the dye sensitized upconversion project.

CHAPTER 5

UPCONVERSION PHOSPHORS AS SENSITIZERS FOR TiO_2 PHOTOCATALYSIS

5.1. Introduction

Photocatalysts have been studied for environmental applications since the late 1960's, when Fujishima and colleagues described the ability of titanium dioxide (TiO_2) to degrade organic material under UV irradiation.[64, 65] When a photocatalyst absorbs light with an energy equal or greater to its band gap (E_{bg}), an electron can be excited from the valence band to the conduction band, resulting in a free electron in the conduction band and a positively charged hole in the valence band—an electron/hole pair. These electrons and holes can diffuse to the particle surface and react with oxygen or water molecules to form reactive oxygen species, or ROS. With TiO_2, the most prevalent ROS produced are hydroxyl radicals ($\cdot OH$) and superoxide anion radicals ($O_2^{\cdot -}$), which can oxidize organic molecules adsorbed onto the TiO_2 surface to form carbon dioxide and water, as shown in Figure 5.1. Applications for TiO_2 nanoparticles include deodorizing and anti-fouling agents, self-disinfecting or hydrophilic surfaces, and catalysts for the degradation of dyes and other organic pollutants in wastewater treatment. TiO_2 photocatalysis for water treatment is an example of an advanced oxidation technology (AOT).

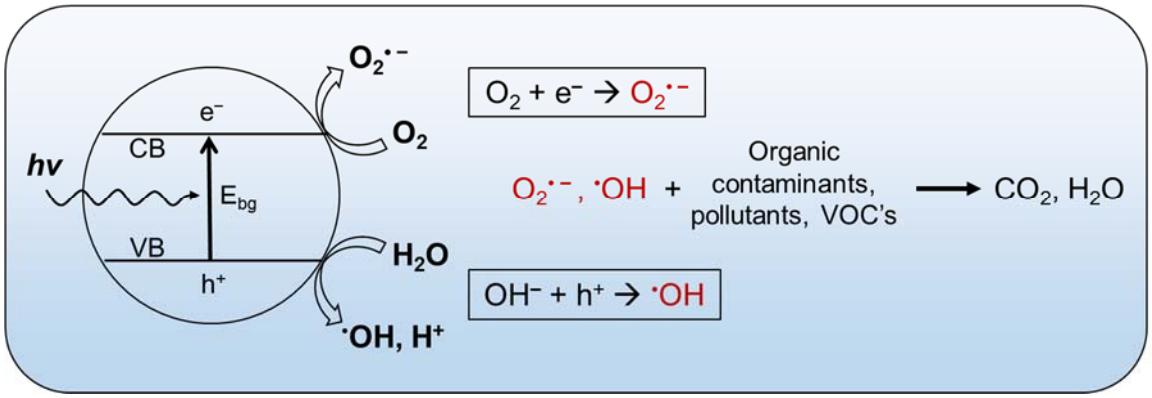

Figure 5.1: Schematic depicting the redox reactions that can occur when a photocatalyst (e.g. TiO_2) absorbs light (E = hv) with $E \geq E_{bg}$. CB = conduction band, VB = valence band. Note that, while the lower oxidation reaction does occur as written, it has been suggested that the main pathway of ·OH production involves the intermediate production of H_2O_2, which can form 2 ·OH upon photoinduced dissociation.

Photocatalytic efficiency is known to be higher in the anatase polymorph of TiO_2 compared to rutile or brookite. The commonly employed Degussa (Evonik) P25, which comprises a mixture of anatase (~80%) and rutile (~20%) phases, is known to be even more efficient; this is often attributed to the rutile phase acting as a heterojunction, slowing down electron-hole recombination. Recombination is one of the main processes that limit the production of ROS.

Due to the wide band gap of TiO_2—3.2 eV (378 nm) for anatase and 3.1 eV (399 nm) for P25[66]—UV excitation is required for photocatalysis. The need for a UV lamp source for treatment applications increases the cost of TiO_2 usage and also limits their applicability, particularly for solar applications. Figure 5.2 depicts the solar energy distribution at the Earth's surface, taken from Air Mass 1.5 (AM-1.5) solar irradiance data.[67] Just 6.6% of the solar irradiation is in the UV range, meaning bare TiO_2 would be quite inefficient under solar excitation.

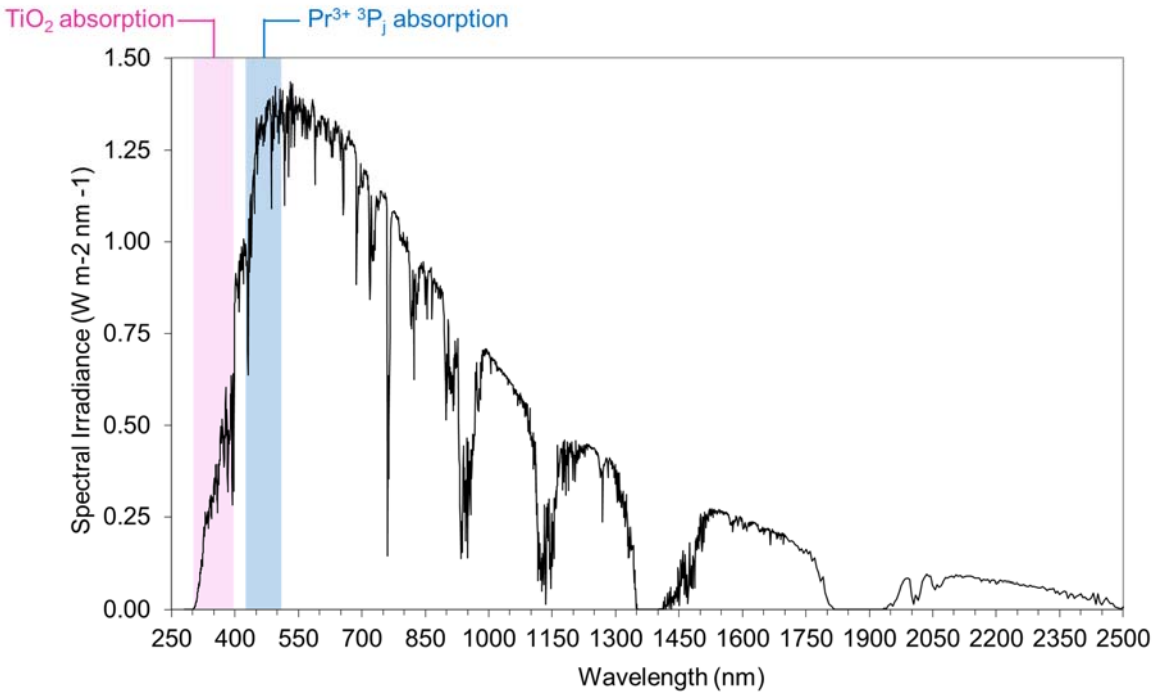

Figure 5.2: AM-1.5 solar irradiance. The range of wavelengths absorbed by unmodified anatase TiO_2 (pink) overlaps with only 6.6 % of the spectrum; the range of ^3P_j absorbance in $Y_2SiO_5:Pr^{3+}$ visible-to-UVC upconversion phosphors (blue) is shown for comparison.

Because of the numerous benefits of solar activation, many techniques have been explored to utilize visible or even IR radiation to excite TiO_2. In practice, this can be accomplished either by narrowing the TiO_2 band gap so it can absorb lower energy photons, or by converting the lower energy photons to higher energy UV. The former is more common and can be achieved by modifying TiO_2, for example doping with nitrogen or other anions such as sulfur or carbon.[65] While doping can lower the TiO_2 band gap energy, this also has the drawback of higher recombination rates and reduced redox potential compared to the undoped TiO_2 under UV excitation. Conversion of excitation light can be achieved using upconversion phosphors (UCPs) that convert NIR or visible light to UV radiation, which can be directly absorbed by unmodified TiO_2. A schematic of this upconversion-activated photocatalysis mechanism is shown in Fig. 5.3, whereby a UCP material excited by low energy light (visible depicted here) can emit UV, which is absorbed by a surrounding layer of TiO_2. The TiO_2 can then catalyze the formation of ROS, which can be used to clean contaminated water, air, or surfaces. Inorganic UCPs in particular could be useful as sensitizers for these applications due to their established chemical and thermal stability.

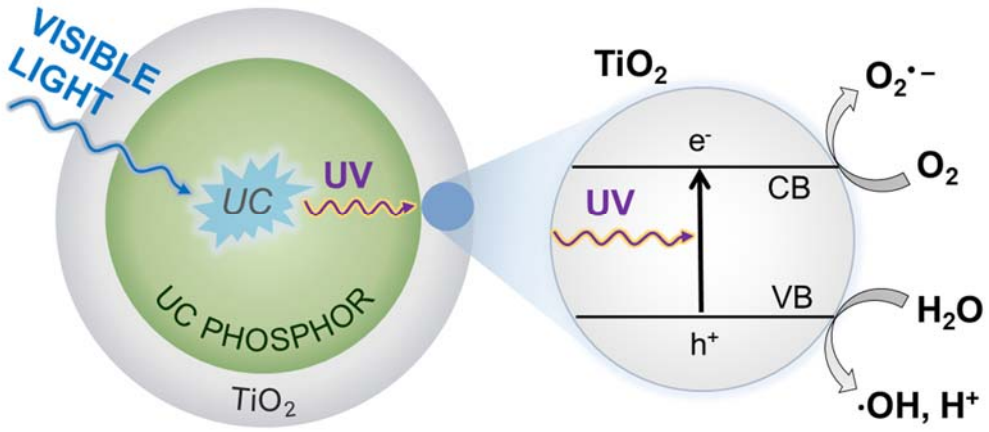

Figure 5.3: Schematic of UC-activated photocatalysis utilizing TiO_2-coated visible-to-UV UCP.

Qin et. al. first demonstrated UCP sensitization of TiO_2 using YF_3:Yb,Tm/TiO_2 core-shell particles; the YF_3:Yb,Tm UCPs converted NIR to UVA, enabling the photodegradation of methylene blue dye under NIR excitation.[68] To demonstrate how TiO_2 can be sensitized by UCPs under visible excitation, we employed sol-gel $Y_2SiO_5:Pr^{3+}$ phosphors, which exhibit broad UC emission peaks at 276 nm (UVC) and 315 nm (UVB). While a few publications have described UC-activated photocatalysis using Er^{3+}- and Pr^{3+} doped phosphors, [69-72] it should be noted that these findings are not fully supported; these papers have either omitted upconversion spectra altogether or show spectra that contradict those found in preceding literature. In particular, we must stress that the work by Wang and coworkers reporting photocatalytic activity in these exact systems—$Y_2SiO_5:Pr^{3+},Li^+$ combined with TiO_2—present false UC emission spectra that are not characteristic of Pr^{3+} (these appear to be artifacts of the benchtop spectrophotometer used to measure UC, which in itself was atypical as advanced laser systems are the standard for UC measurement), and was published in a source of unknown reputability.[71, 72] To our knowledge, then, this represents the first true demonstration of visible-light activated photocatalysis using upconversion materials.

5.2. Experimental

Sol-gel phosphor synthesis. Powder Y_2SiO_5 doped with 1.2 mol.% Pr^{3+} and 10 mol.% Li^+ (i.e. phosphors prepared assuming the composition of $Y_{1.909}Pr_{0.024}Li_{0.2}SiO_5$, which will be referred to herein as $Y_2SiO_5:Pr^{3+}$) were prepared using a sol-gel decomposition synthesis, as described in our previous work.[1] In brief, aqueous solutions of $Y(NO_3)_3$, $Pr(NO_3)_3$, and $LiNO_3$ were combined, following the above stoichiometry. The

nitrates were dried and re-dissolved in water and ethanol before adding a stoichiometric (Si basis) amount of TEOS. This solution was heated to form a gel and then dried in an oven at 100 °C. The resulting pale-yellow xerogel was ground into a powder and calcined in a furnace at 1000 °C for 3 h in air. Powders were cooled at room temperature and ground before use.

Ultrasonic spray pyrolysis. Spherical $Y_2SiO_5:Pr^{3+}$ were synthesized using ultrasonic spray pyrolysis. Precursor solutions were prepared by mixing aqueous solutions of $Y(NO_3)_3$, $Pr(NO_3)_3$, $LiNO_3$, and TEOS following the stoichiometry $Y_{1.89}Pr_{0.01}Li_{0.10}SiO_{4.9}$, as used in previous work.[1] The solution was diluted to a concentration of 1 mmol/L and placed in an ultrasonic spray generator, with vapor outlet fitted to one end of a quartz tube furnace. After preheating the furnace to 600 ºC, vaporized particles were pumped through the tube, in air, and collected at the outlet on a 0.2 μm filter. Filters were dried to recover the reacted powders, which were then calcined at 1000 °C for 3 h in air. Powders were cooled at room temperature and ground before use.

Coating with TiO_2. Phosphors were coated with TiO_2 by mixing appropriate amounts of phosphor powders, PVP (Sigma Aldrich), and $TiCl_4$ (Sigma Aldrich) in ethanol and stirring for 24 h. The solutions were dried in a 60 °C oven for 5 h, then annealed at 500 °C for 2 h. The resulting coatings were confirmed to be anatase TiO_2, using XRD.

Film preparation. $Y_2SiO_5:Pr^{3+}$-P25 composite films were prepared by mixing Evonik Aeroxide P25 TiO_2 (Sigma Aldrich) with phosphor powders in various molar ratios, ranging from 10:1 to 1:1. Powders were ground in a mortar and pestle with a 1:1 (by weight) solution of PEG and DI water to form a viscous paste. The mixture was quickly deposited onto 12 mm silica slides using a cascading technique, whereby the mixture is

smoothed out across the surface using a straight-edge glass tube. The tube was guided along two spacers on either side of the sample rather than the sample itself, to keep film thicknesses consistent. The as-prepared films were approximately 0.5 mm thick. Films were dried at RT and annealed at 500 °C for 2 h, in air.

Platinum loading. Platinized $Y_2SiO_5:Pr^{3+}$ -P25 composite films were prepared by using a photodeposition method.[73, 74] Films were irradiated with a 13-W black light for 15 min in an aqueous solution containing H_2PtCl_6 (0.33g/L) and methanol (33v/v%). After irradiation, platinized $Y_2SiO_5:Pr^{3+}$-P25 composite films were washed with DI water.

Materials characterization. Photoluminescence spectroscopy (PLS) was conducted using a 447 nm diode-pumped solid-state laser (OEM Lasers) set at 100 mW. Powder samples were uniformly compacted into sample holders with a depth of 4 mm. The laser was focused onto the center of each sample at a 45º angle from the sample face and focusing lenses aligned normal to the sample face guided the upconverted emission through a 400 nm cutoff filter and to the detector. The emission signal was processed using phase-sensitive detection, as described previously.[1] High resolution TEM images and EDS measurements were obtained using an FEI Tecnai Osiris TEM equipped with a high-angle annular dark field (HAADF) detector. SEM was performed using a Hitachi SU-70 microscope.

Polyoxometalate reduction. Reduction of polyoxometalates (POMs) was used as a measure of photocatalysis by illuminated films. $Y_2SiO_5:Pr^{3+}$-P25 composite films (with and without Pt deposition) were irradiated in an aqueous solution containing PMo_{12}^{3-} (0.5 mM) and methanol (5% (v/v)) under blue LED irradiation (λ_{max} = 450 nm, with 420 nm UV cutoff filter). A depiction of this setup is shown in Fig. 5.4, showing films (placed in

individual wells) irradiated by an LED array below. Aliquots of solution were withdrawn from the reactor every 30 min during the irradiation period and filtered through a 0.45 μm PTFE syringe filter (PALL) to remove any composite particles that may have leached into solution. The reduced PMo_{12}^{3-} was detected spectrophotometrically (Shimadzu) by measuring absorbance at 700 nm which represents an intervalence charge transfer (IVCT, $Mo^{5+} \rightarrow Mo^{6+}$) band of reduced Keggin molecular species.[75]

Coumarin degradation. The degradation of coumarin by ·OH radicals and subsequent production of the intermediate product 7-hydroxycoumarn was also used to measure photocatalytic activity of TiO_2-UCP composites under visible light. However, due to the inconsistencies and long reaction times needed while using this method, we chose to focus solely on POM reduction for measuring photocatalytic activity. A full explanation and presentation of representative coumarin degradation data can be found in Appendix C.

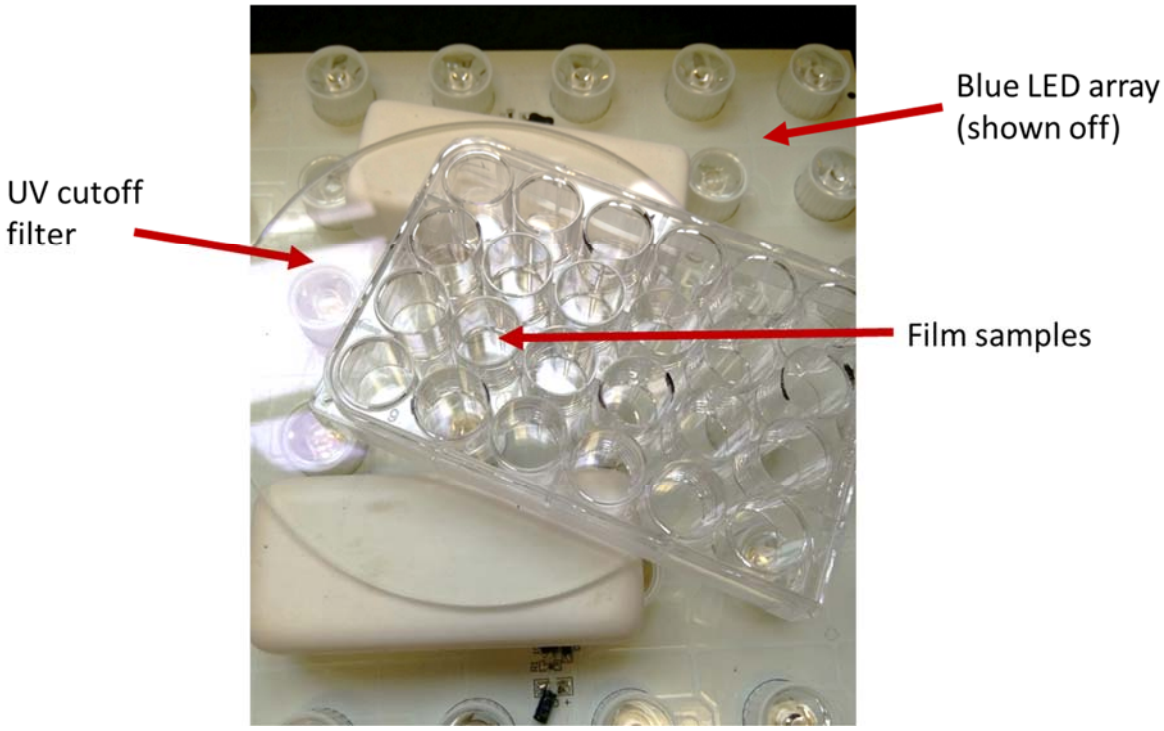

Figure 5.4: Experimental set-up for POM reduction experiments.

5.3. Results and discussion

Characterization of phosphors. Phosphors were synthesized using two methods. First, a sol-gel method was used, as in previous work,[1] which produced irregularly shaped particle aggregates with crystallite sizes ranging from 10 nm-2 μm. Second, an ultrasonic spray pyrolysis (USP) method was developed to achieve spherical particles, as described in the previous chapter. SEM micrographs of the two forms of $Y_2SiO_5:Pr^{3+}$ are depicted in Fig. 5.5. USP particle sizes ranged from 0.2-2 μm.

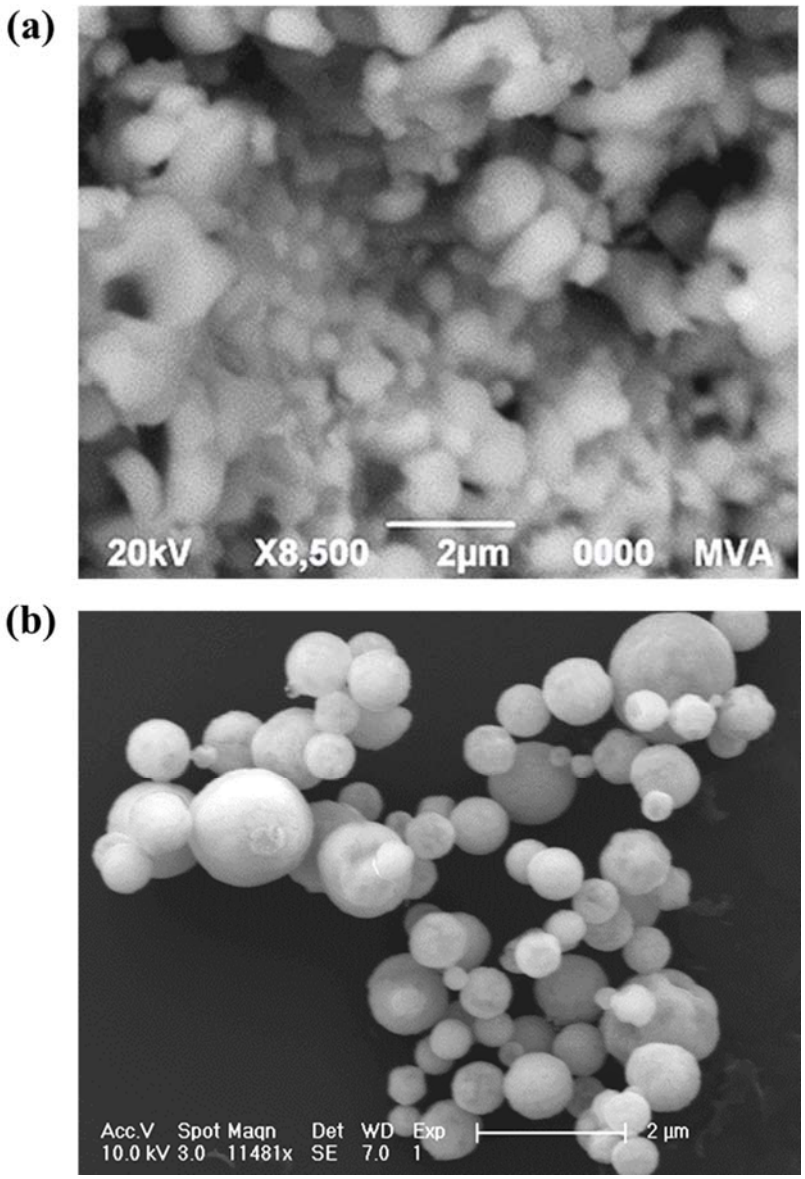

Figure 5.5: SEM micrographs showing (a) sol-gel derived $Y_2SiO_5:Pr^{3+}$, and (b) $Y_2SiO_5:Pr^{3+}$ from ultrasonic spray pyrolysis. Both were annealed at 1000 °C for 3 h.

The TEM images shown in Chapter 3, Fig. 4.7 indicate that USP particles had interior porosity, consistent with results reported in the literature for similar syntheses.[76] The white rims around the particles, however, indicate more dense material on the surface of the spheres. This suggests that the most pores do not extend to the surface, so this should not increase the surface area on which TiO_2 can be deposited. This was also suggested by the SEM images, in which there were only a few instances of apparent surface porosity. It is unclear if this porous interior network would be detrimental to the observed UC for USP particles, though we would expect less porous spheres to be more efficient simply due to a higher density of optically active material. A recent paper reported that hollow spheres of YAG:Ce^{3+} produced by a spray drying technique could be fully densified by ball-milling the hollow spheres, dispersing the ground nanopowders in solution, and putting this solution through the spray-drying process again.[77] The resulting particles, after annealing, were reportedly spherical with high density and crystallinity. This method could potentially be applied to the USP synthesis for Y_2SiO_5:Pr^{3+} to achieve similar results. Open porosity can, however, be beneficial for catalytic reactions, particularly if dispersing a TiO_2-coated phosphor in aqueous solution. If the pores are large enough to accommodate TiO_2 and the target organic material, the reaction surface area and consequently the photocatalytic efficiency could potentially be increased. For further discussion regarding intentionally porous USP particles, see the discussion in Chapter 6.

As discussed in Chapter 4, the USP method resulted in X1-Y_2SiO_5 phase phosphors when annealing at 1000 °C, confirmed by XRD. The particles assumed the X2 phase upon further heating at 1300 °C but had significantly reduced emission. While Pr^{3+} has been shown to have slightly higher ^3P_J intermediate state energies (a difference of ~125 cm^{-1})[29] when doped into X1-Y_2SiO_5 compared to X2-Y_2SiO_5, and thus could be less efficient at converting lower energy photons in this phase, a comparison of the UC luminescence shown in Fig. 5.6 shows that the USP (X1) and sol-gel (X2) phosphors had comparable emission intensity under 447 nm excitation. The emission peaks for X1-Y_2SiO_5:Pr^{3+} are red-shifted compared to X2 due its slightly lower 45fd band energy, making the X1 polymorph less desirable for applications requiring UVC emission. For the TiO_2 sensitizing application, however, the X1 particles should be suitable since 100% of the UV emitted can still be absorbed by TiO_2. For this reason, the USP particles used herein were X1-Y_2SiO_5:Pr^{3+} (i.e. annealed at 1000 °C).

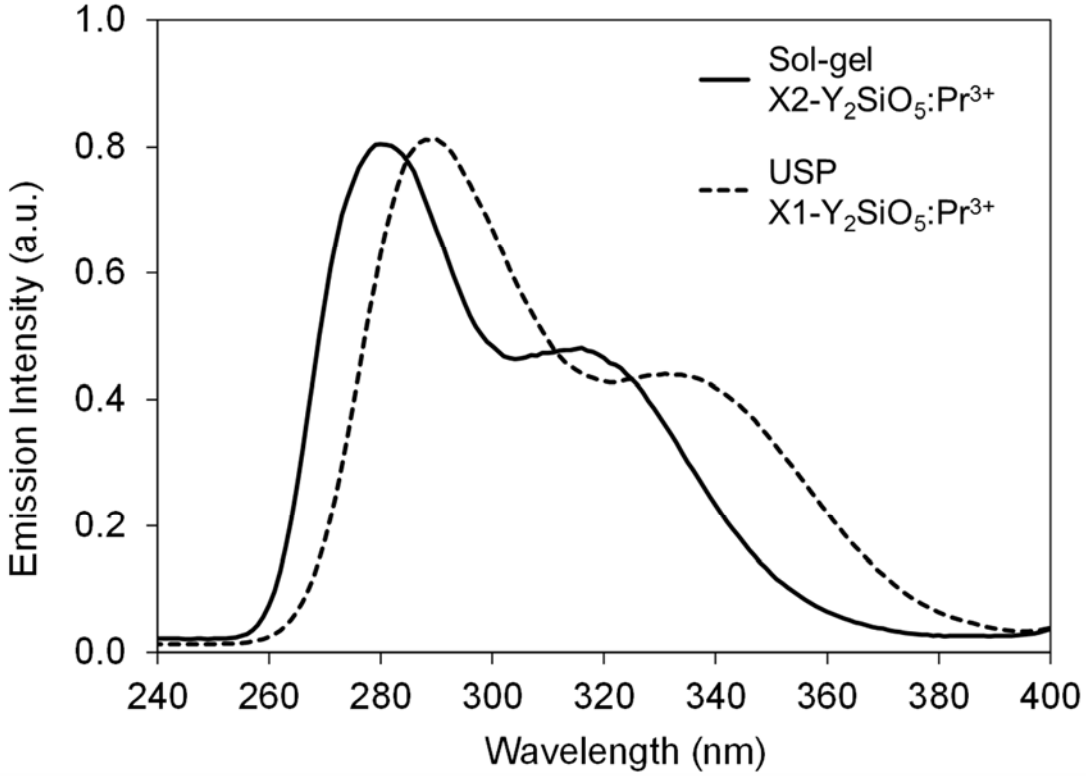

Figure 5.6: Photoluminescence spectra for $Y_2SiO_5:Pr^{3+}$ prepared using sol-gel synthesis (solid line) and ultrasonic spray pyrolysis (dotted line), under 447 nm excitation.

Phosphors were combined with TiO_2 either by mixing with P25 or by coating the phosphors using a $TiCl_4$ hydrolysis method. To confirm the transfer of UV emission from the phosphors to TiO_2, the emission of TiO_2-coated sol-gel $Y_2SiO_5:Pr^{3+}$ were measured using PLS. Though Stokes emission did decrease (Fig. 5.7a), possibly due to scattering of the laser light by the TiO_2, the upconverted UV emission completely diminished (Fig. 5.7b). Similar results were observed for P25-$Y_2SiO_5:Pr^{3+}$ composite materials. This observed decrease in UC emission is the result we would expect for efficient absorption of UV by the photocatalyst.

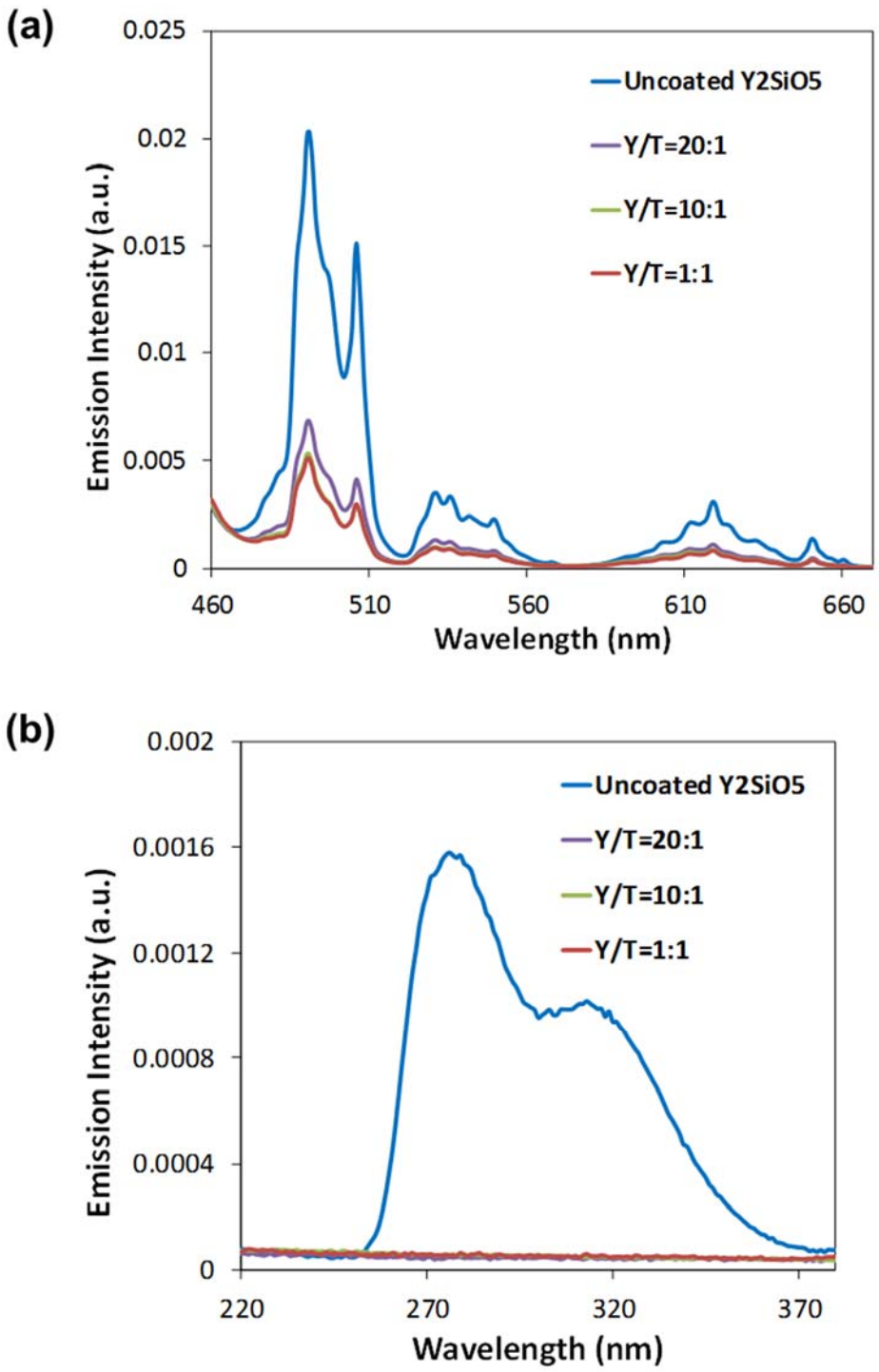

Figure 5.7: (a) Stokes emission spectra and (b) upconversion emission spectra for TiO_2 coated sol-gel $Y_2SiO_5:Pr^{3+}$ phosphors, under 447 nm laser excitation. "Y" = $Y_2SiO_5:Pr^{3+}$, "T" = TiO_2

Photocatalytic activity. To test the performance of UCPs as sensitizers for TiO_2 under visible light, thin films containing a mixture of photocatalysts and phosphors were prepared and irradiated with a low-intensity blue LED. Photoreduction of the polyoxometalate (POM) species phosphomolybdate (PMo_{12}^{3-}) was used as to assess the photocatalytic activity of each sample. POMs have been widely used as electron acceptors and carriers because they can be readily reduced and oxidized reversibly without undergoing structural decomposition. Thus, PMo_{12}^{3-} can be easily reduced by the conduction band electrons produced when TiO_2 becomes excited. The reduction product, PMo_{12}^{4-}, is visible to the eye (blue color) and can be quantitatively measured using UV-Vis spectroscopy. [75, 78-80] While POM can be excited by a UV lamp source to produce the reduced form, the amount of UV produced by our phosphors is not enough to induce this reaction, and it is visible from the phosphor-only control data that UVC from $Y_2SiO_5:Pr^{3+}$ does not cause any measureable reduction.

Due to the initially weak signals obtained when irradiating the P25-phosphor composites in POM solution, the films were also tested after loading with platinum (Pt). Platinum-doped TiO_2 is commonly used in photocatalytic studies due to its higher photoactivity compared to regular TiO_2. The enhancement arises because Pt, which adsorbs onto the surface of TiO_2, can act as a sink for electrons; when TiO_2 is excited, the conduction band electrons can flow to Pt, and the recombination of those electrons with the positively charged holes is discouraged. Platinization is thus able to prolong the time in which redox reactions can occur. As will be shown, the P25-UCP composite materials do not require Pt for UC-activated photocatalysis to occur, but Pt loading helps to enhance the observed spectra so that we may effectively compare and optimize each sample.

Figures 5.8 and 5.9 show the absorption spectra over 3 h of irradiation time for film samples and controls, respectively. The broad absorbance centered at 700 nm is characteristic of PMo_{12}^{4-}, and is proportional to the amount of POM reduced and the level

of TiO_2 sensitization by the UCPs. Control samples did not show any appreciable absorption in this range.

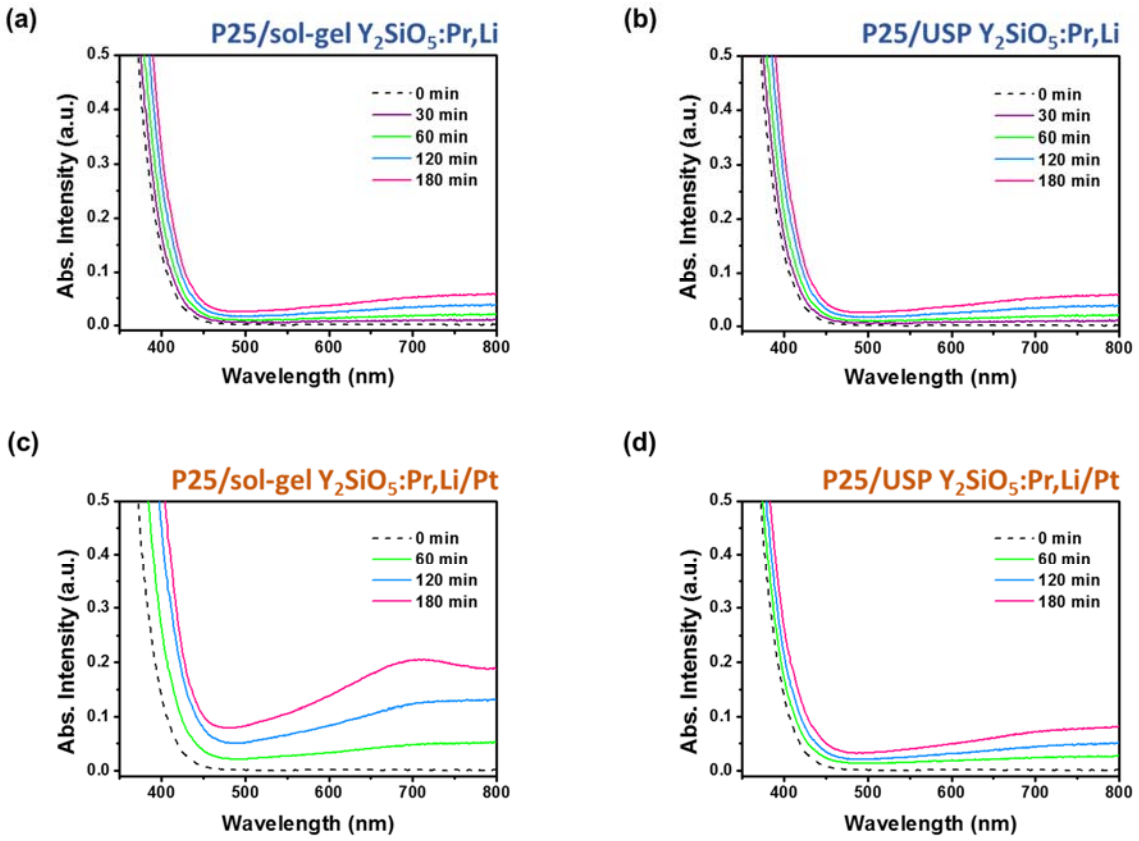

Figure 5.8: UV-Vis absorbance data for film samples over 180 min of blue LED irradiation, comparing (a) P25 mixed with sol-gel $Y_2SiO_5:Pr^{3+}$ in (1:1) molar ratio, (b) P25 mixed with USP $Y_2SiO_5:Pr^{3+}$ in (1:1) molar ratio, and (c and d) the platinized versions of each, respectively. The increase in absorbance centered ~700 nm (absorbance of the reduction product, PMO_{12}^{3-}) corresponds to an increase in POM reduction by photogenerated electrons.

As shown in Fig. 5.8, the films containing X2-$Y_2SiO_5:Pr^{3+}$ (from sol-gel synthesis) mixed with P25 were slightly more effective at TiO_2 sensitization than those containing spherical X1-$Y_2SiO_5:Pr^{3+}$ (from ultrasonic spray pyrolysis) mixed with P25. The absorbance for both samples was significantly increased upon platinization, with the P25/X2 phosphor films again having the highest level of electron production. Both film types were mixed using a (1:1) molar ratio of P25 to phosphor. While the cascade deposition technique can result in some thickness variation across each films, we expect that the differences seen here are more representative of the difference between the activity of the X1- and X2- phase materials, rather than differences in film thickness or surface area. As observed under laser excitation, the USP phosphors had red-shifted UC emission compared to sol-gel phosphors, and much smaller crystallites which typically mean lower UC efficiency (see Chapter 3, Section 3.3). Repeat tests for each sample type produced similar results, not shown here. We also tested both phosphor types using higher ratios of TiO_2 ((5:1) and (10:1) P25:Y_2SiO_5), but these samples all had lower photoreduction than the (1:1) films, decreasing with increasing P25 concentration. While a deficiency of TiO_2 would lead to inefficient absorption of the UV emitted by the phosphors, an excess of TiO_2 could cause unwanted scattering of excitation light, in addition to decreasing the concentration of UCPs per given area. It is possible that the optimal concentration of P25:$Y_2SiO_5:Pr^{3+}$ is less than (1:1), which has not yet been tested; if so, the resulting composite could yield even higher visible light photoactivity than observed here.

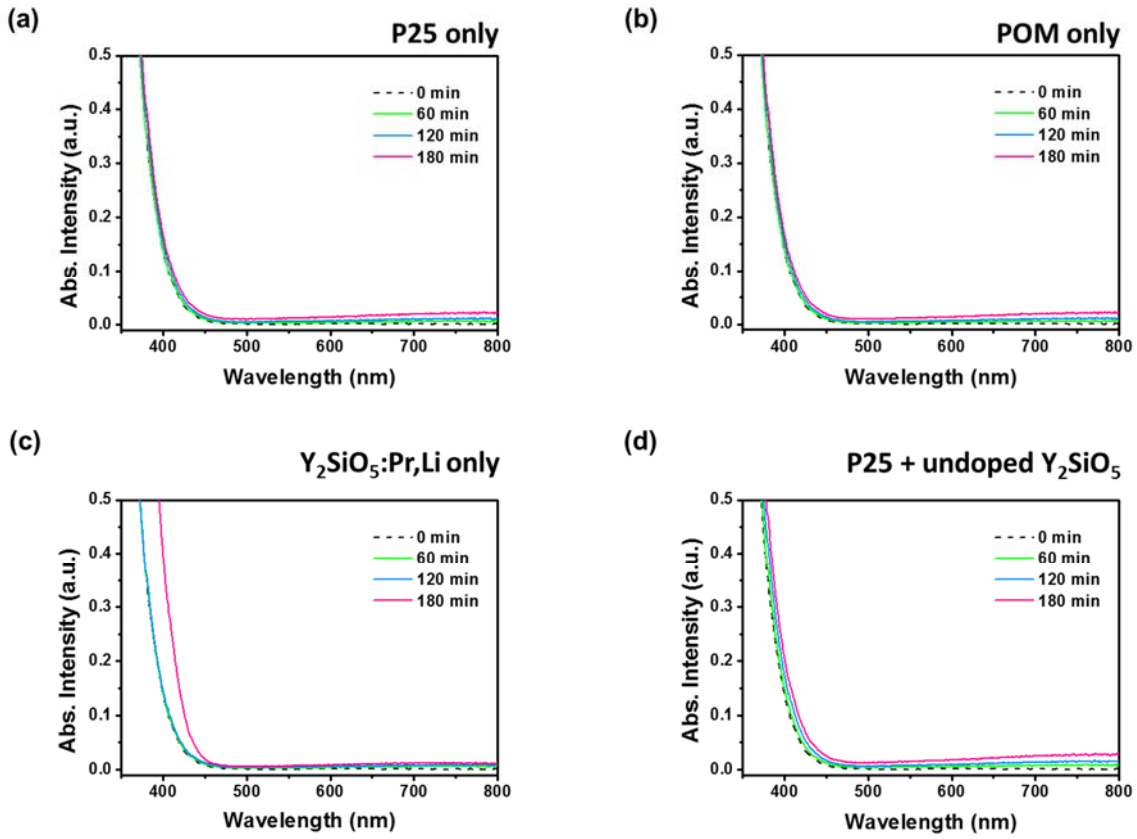

Figure 5.9: UV-Vis absorption data for control sets: (a) Aeroxide P25 film alone, (b) POM in solution without any film, (c) sol-gel $Y_2SiO_5:Pr^{3+}$ film alone, and (d) film of P25 mixed with undoped Y_2SiO_5 in (1:1) molar ratio. Each test showed negligible amount of POM reduction during 180 min of blue LED irradiation.

To determine if fixed TiO_2 coatings would be more efficient than the mixed-P25/UCP composites, due to a controlled positioning of photocatalysts at all optically active sites, films of TiO_2-coated X2-$Y_2SiO_5:Pr^{3+}$ were also made. These had the lowest POM reduction out of all samples, barely exceeding the activity of the control sets. The TiO_2 coatings were applied using a routine $TiCl_4$ hydrolysis method which was executed to achieve a TiO_2:Y_2SiO_5 ratio of 5:1. The photocatalytic activity of the TiO_2 coating was confirmed under UVA blacklight excitation, and other powders coated using the same method were confirmed to consist of anatase phase TiO_2 using x-ray diffraction analysis. The relatively low activity could arise from the lower photoactivity of anatase TiO_2 compared to P25, or it could be that P25/phosphor mixtures produce films with more dispersed reactants and higher TiO_2 surface area, to more effectively adsorb the Pt and POM. Since the UV emitted from the phosphors has been shown to travel a significant distance (on the order of mm), close contact between the phosphors and photocatalysts (as with TiO_2-coated phosphors) is not necessary, and could even be detrimental, as shown here. Though the TiO_2 coatings could not be distinctly imaged using TEM, due in part to the large, irregular shape of the sol-gel phosphors, it is likely that the TiO_2 surface was more compact and had lower surface area compared the P25/phosphor mixtures; the SEM image in Fig. 5.9 of a dry-mixed and annealed P25/X2-$Y_2SiO_5:Pr^{3+}$ mixture shows that the phosphor particles were covered with a thick, open network of adsorbed P25. We would expect similar arrangement of photocatalysts around the phosphors for film samples.

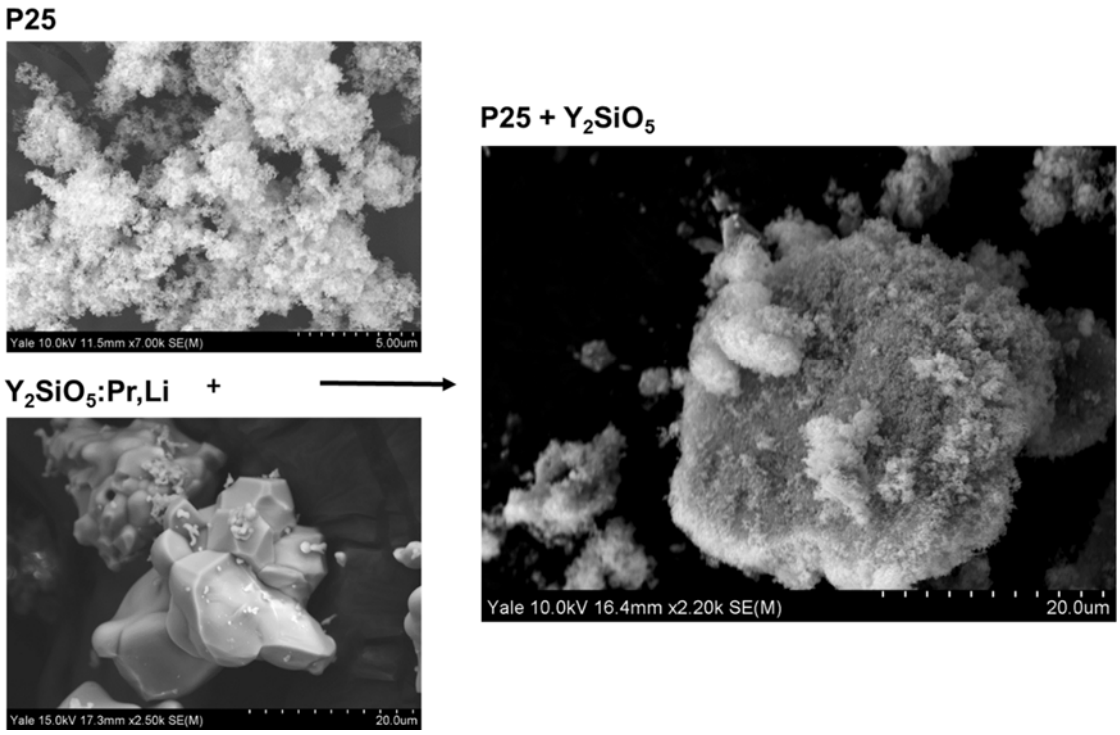

Figure 5.10: SEM micrographs depicting P25 TiO_2 and sol-gel X2-Y_2SiO_5:$Pr,^{3+}$ phosphors separately before mixing (left) and after being ground together and annealed (right).

5.4. Conclusion

Using inorganic upconversion phosphor materials that were previously optimized to convert visible light to UVC, we have demonstrated successful sensitization of commercial TiO_2 photocatalysts under visible light. Reduction of polyoxometalates was used as an indicator of the increased conduction band electron production by the TiO_2 over time, when mixed with the phosphors. This was the first study of its kind showing the conversion of low-intensity visible light to UV and the subsequent absorption of UV by TiO_2. These findings suggest that visible-to-UVC phosphors could enable photocatalysis by unmodified TiO_2 under broadband visible light, with implications for solar wastewater treatment.

CHAPTER 6

VISIBLE-TO-UVA/UVB UPCONVERSION PHOSPHORS

6.1. Introduction

The $Y_2SiO_5:Pr^{3+}$ system was initially studied by our group because it was the only visible-to-UVC UC material reported in the literature at the time.[30, 31] Of all lanthanide activator ions, Pr^{3+} appears to be the most suitable activator for this type of conversion, as it contains numerous energy levels capable of absorbing violet, blue, and cyan wavelengths with a significant energy gap between the intermediate states and the emitting 4f5d band (see energy level diagram in Fig. 3.1). However, it was expected that more optimal hosts existed other than Y_2SiO_5, due its large phonon cutoff energy of ~970 cm^{-1},[81] implying high non-radiative relaxation rates.[3] It was therefore of great interest to see if Pr^{3+} doped into other host crystals could have even higher UC efficiency. Unfortunately, the effective fluoride host materials commonly used in UC phosphors are not suitable for visible-to-UVC conversion by Pr^{3+}, since the host-dependent edge energy of the 4f5d band of Pr^{3+} doped in these materials is too high to allow ESA or ETU processes to occur in the presence of visible light.[82, 83] Visible-to-UVC UC by organic systems also seemed unlikely, since effective sensitizers and acceptor molecules–as well as the solvent–contain large numbers of double bonds, and thus are likely to have high UVC absorbance.

In our attempts to identify the optimal host crystal for Pr^{3+} UC, we came across a host material—yttrium aluminum garnet, commonly known as YAG ($Y_3Al_5O_{12}$)—that was not well suited for UVC emission from Pr^{3+} but exhibited very strong emission of UVB and UVA. While not germicidal, the conversion of low-intensity visible light to these UV

wavelengths could be useful for other environmental applications. Most notably, these could be used to sensitize photocatalysts such as TiO_2, as demonstrated with visible-to-UVC upconversion phosphors in the previous chapter. In fact, sensitization of TiO_2 by UVB and UVA should be more efficient than UVC since they are closer in energy to the TiO_2 band gap, meaning less upconverted energy will be wasted as heat. YAG was also appealing as a host because of its lower phonon cutoff energy (~850 cm^{-1} [84]) compared to Y_2SiO_5, which is beneficial for UC because this reduces nonradiative energy losses.[3]

YAG is a synthetic crystalline material historically used for solid state lasers, wherein laser crystals are formed by doping a YAG host with trivalent rare earth ions, such as Nd and Er.[85] Because YAG phosphors are known to exhibit good stability and high optical efficiency, they are being studied for a number of applications including LEDs and other optic displays.[86] These properties also make YAG suitable for UC applications, and indeed, UC in Pr^{3+}-doped YAG phosphors have been presented in the literature.[87-89]

Most of the existing work regarding UC in YAG:Pr^{3+} utilized single crystal YAG for laser applications.[87-89] One exception is work by Kolesov et al.,[5] who studied Pr^{3+}-doped YAG as a model candidate to image single rare earth ions within a crystal, for bioimaging or specialized material applications. The upconverted UV emissions from Pr^{3+} were necessary to detect the ions using microscopy, so the UC spectral properties and excited state dynamics of YAG:Pr^{3+} were analyzed. A proof of concept was also presented for the death of HeLa cells by the emitted UV under laser irradiation, for application to localized, site-specific cell degradation. The effects of varying Pr^{3+} concentration, synthesis methods, and annealing conditions were not included in the aforementioned works, nor was a discussion of how the properties of bulk powder or ceramic YAG:Pr^{3+} affect UC efficiency.

Here we present the development of Pr^{3+}-doped YAG phosphors optimized to emit UVB when excited by visible light. The UC efficiency of Pr^{3+} in YAG is discussed with regards to synthetic conditions and compared to the efficiency of Pr^{3+} in other host crystals. Finally, the potential for these materials to be used as sensitizers for TiO_2 in visible-light activated photocatalysis will be discussed, along with the presentation of preliminary data.

6.2. Experimental

Phosphor synthesis. YAG phosphors were first synthesized using the Pechini method.[90] An aqueous solution containing 5.22 mmol $Y(NO_3)_3$ (Rare Earth Products) and 0.5 mL acetic acid (reagent grade, Sigma Aldrich) was mixed with an aqueous solution of $Al(NO_3)_2 \bullet 9H_2O$ (Sigma Aldrich) before adding 0.5 mL ethylene glycol (Sigma Aldrich). The transparent solution was gently stirred and heated at 70 °C to form an off-white foam. The foam was dried fully at 105 °C, ground, and subsequently annealed at 1000 °C for 3 h in air. The resulting powders were bright white in color. Pr^{3+}-doped YAG were prepared in the same manner by substituting appropriate amounts of $Y(NO_3)_3$ with $Pr(NO_3)_3$ (Sigma Aldrich), following the stoichiometry $Y_{3-x}Pr_xAl_5O_{12}$. (with values of x ranging from 0.003 to 0.042, corresponding to 0.1 % to 1.4 % Pr doping, respectively). All phosphor powders were cooled naturally and ground before use.

For the citrate sol-gel synthesis of YAG:Pr^{3+}(0.5%), stoichiometric mixtures of $Y(NO_3)_3$, $Pr(NO_3)_3$, and $Al(NO_3)_3$ nonahydrate (all Sigma Aldrich) were dissolved in an aqueous solution of citric acid (Sigma Aldrich, 99%), such that the solution consisted of 2 M citric acid, 0.2 M $Al(NO_3)_3$, 0.1194 M $Y(NO_3)_3$, and 0.0006 M $Pr(NO_3)_3$. This mixture was heated at 80 °C in air until a gel formed, which was then dried at 105 °C for 24 h before

grinding and annealing at 1000 °C for 3 h, in air. Powders were cooled naturally and ground before use.

Film preparation. YAG:Pr^{3+}-P25 composite films were prepared by mixing Aeroxide P25 TiO_2 (Sigma Aldrich), using a (1:1) molar ratio of TiO_2 to phosphor. Powders were ground in a mortar and pestle with a 1:1 (by weight) solution of PEG and DI water to form a viscous paste. The mixture was quickly deposited onto 12 mm silica slides using a cascading technique, whereby the mixture is smoothed out across the surface using a straight-edge glass tube. The tube was guided along two spacers on either side of the sample rather than the sample itself, to keep film thicknesses consistent. The as-prepared films were approximately 0.5 mm thick. Films were dried at RT and annealed at 500 °C for 2 h, in air.

Platinum loading. Platinized YAG:Pr^{3+}-P25 composite films were prepared by using a photodeposition method.[73, 74] Films were irradiated with a 13-W black light for 15 min in an aqueous solution containing H_2PtCl_6 (0.33g/L) and methanol (33v/v%). After irradiation, platinized Y_2SiO_5:Pr^{3+}-P25 composite films were washed with DI water.

Polyoxometalate reduction. Reduction of polyoxometalates (POM) was used as a measure of photocatalysis by illuminated films. The composite films (with and without Pt deposition) were irradiated in an aqueous solution containing PMo_{12}^{3-} (0.5 mM), methanol (5% (v/v)) under blue LED irradiation (λ_{max} = 450 nm, with 420 nm UV cutoff filter). Aliquots of solution were withdrawn from the reactor every 30 min during the irradiation period and filtered through a 0.45 μm PTFE syringe filter (PALL) to remove any composite particles that may have leached into solution. The reduced PMo_{12}^{3-} was detected spectrophotometrically (Shimadzu) by measuring absorbance at 730 nm which represents

a intervalence charge transfer (IVCT, $Mo^{5+} \rightarrow Mo^{6+}$) band of reduced Keggin molecular species[75] (reduced PMo_{12}^{3-} with $\varepsilon_{730} = 2300\ M^{-1}\ cm^{-1}$ [91]).

Characterization. Photoluminescence spectroscopy (PLS) was conducted using a 447 nm diode-pumped solid-state laser (OEM Lasers) set at 100 mW. Powder samples were uniformly compacted into sample holders with a depth of 4 mm. The laser was focused onto the center of each sample at a 45º angle from the sample face and focusing lenses aligned normal to the sample face guided the upconverted emission through a 400 nm cutoff filter and to the detector. The emission signal was processed using phase-sensitive detection, as described previously.[1] SEM images were obtained using a Hitachi SU-70 microscope on chromium-sputtered samples. Phase purity was examined by powder x-ray diffraction (XRD) using a Panalytical X'pert Pro diffractometer with X'celerator detector.

Ultrasonic spray pyrolysis. Spherical YAG:Pr^{3+}(0.5%) were synthesized using ultrasonic spray pyrolysis. The precursor solution was prepared following the same initial steps as for Pechini synthesis, above. An aqueous solution containing 5.20 mmol $Y(NO_3)_3$, 0.026 mmol $Pr(NO_3)_3$, and 0.5 mL acetic acid was mixed with an aqueous solution of $Al(NO_3)_2 \bullet 9H_2O$ before adding 0.5 mL ethylene glycol (Sigma Aldrich). Rather than heating this solution until foam formation, this mixture was heated at 65 ºC for 2 h before cooling and diluting to 1 mmol/L with DI H_2O. The solution was diluted to a concentration of 1 mmol/L and placed in an ultrasonic spray generator, with vapor outlet fitted to one end of a quartz tube furnace. After preheating the furnace to 600 ºC, vaporized particles were pumped through the tube, in air, and collected at the outlet on a 0.2 μm filter. Filters were

dried to recover the reacted powders, which were then calcined at 1000 °C for 3 h in air. Powders were cooled at room temperature and ground before use.

6.3. Results and discussion

Phosphor synthesis and characterization. Polycrystalline YAG can be synthesized using a solid-state reaction, hydroxide coprecipitation, alkoxide method, citrate gel method,[86] or Pechini sol-gel synthesis.[90] The latter two methods involve similar reactions and can run at relatively low temperatures of 1000 °C or less. Using the Pechini method, YAG:Pr^{3+} phosphors were obtained that demonstrated stable, consistent emission of UVB-UVA radiation upon visible light irradiation. Energy level diagrams for Pr^{3+} ions in YAG are shown in Fig. 6.1 (for a more detailed representation of transitions in Pr^{3+}-doped YAG, we refer the reader to Fig. 1 of this reference[25]). Note that the bottom of the 4f5d band is lower than for Pr^{3+} in the Y_2SiO_5 host, which is the reason for lower energy upconverted emission. A citrate gel method was also used to make YAG:Pr^{3+}, but the resulting upconverted emission was approximately half the intensity of the sol-gel phosphors (data not shown). For this reason, the Pechini method was used for all subsequent YAG optimization.

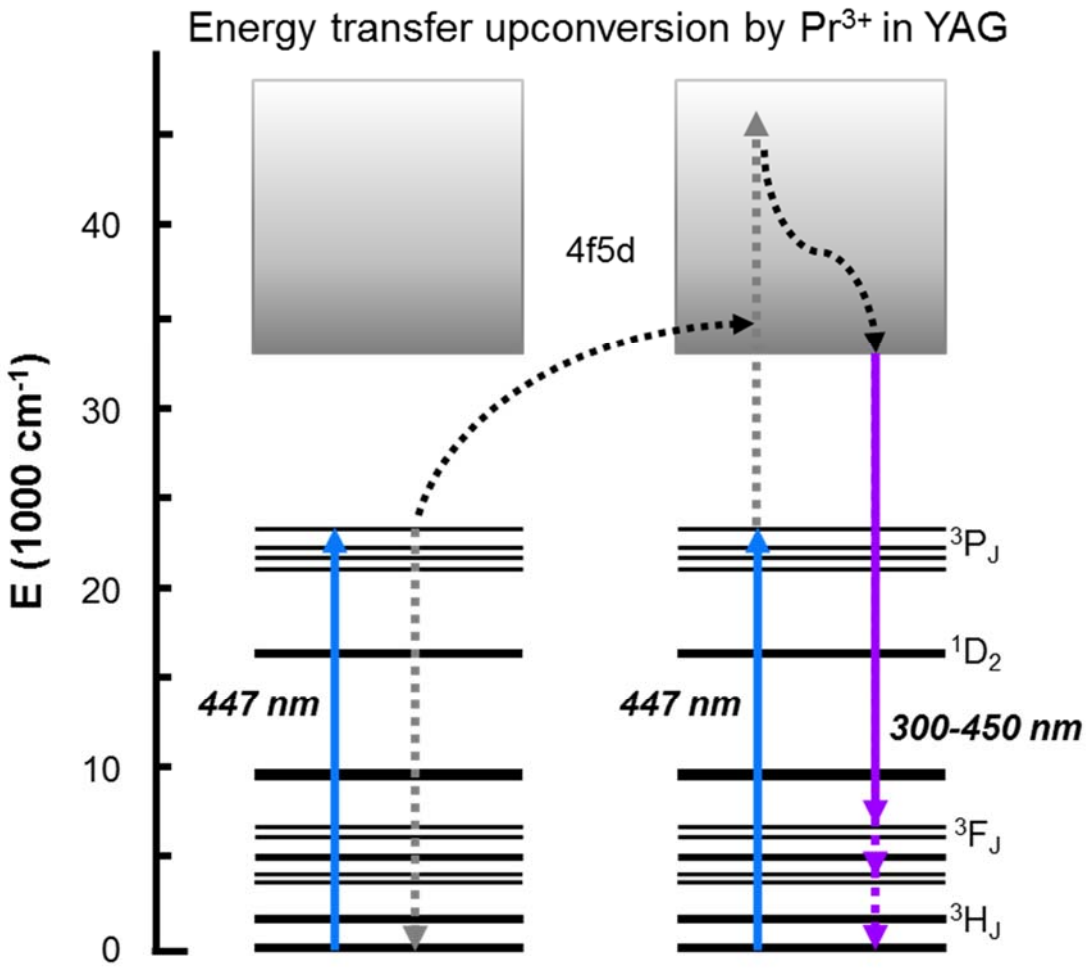

Figure 6.1: Energy diagram depicting ETU between neighboring Pr^{3+} ions in YAG. Note the shift of the 4f5d band to lower energies compared to the energy level diagrams for Pr^{3+} in Y_2SiO_5 (see Chapter 3).

Photoluminescence spectroscopy is shown in Fig. 6.2 for YAG:Pr^{3+} doped at 0.5 mol.%. Two characteristic UC emission peaks are seen, one in the UVB from ~300-360 nm (corresponding to the transitions from 4f5d → $^3H_{4,5,6}$) and another shoulder peak centered around 390 nm (4f5d → $^3F_{3,4}$); the latter cannot be fully visualized using our detection equipment, since a 400 nm shortpass filter is used to best measure the UV photons. The inset depicts the optimization of Pr^{3+} concentration in YAG, determined by the intensity of the highest energy (UVB) UC peak (centered at approximately 319 nm). The optimal concentration was found to be 0.5 mol.% Pr^{3+}, which is substituted for Y^{3+} in the YAG crystal lattice. Of note, the addition of Li^+ did not increase UC luminescence, as it had with Pr^{3+}-doped Y_2SiO_5, so the YAG phosphors described here are not doped with Li^+.

Comparing the upconverted emission of YAG:Pr^{3+} to that of the optimized Y_2SiO_5:Pr^{3+} sol-gel phosphor under the same 447 nm laser excitation (Fig. 6.2), it is clear that UC efficiency of the Pr^{3+} ion is higher in the YAG host. One can integrate these curves to estimate a 20-fold enhancement in the magnitude of overall UV photoluminescence by the YAG phosphors. Though YAG does have lower phonon energy than Y_2SiO_5, which would decrease nonradiative energy losses and potentially improve upon UC, this difference can also be attributed to the fact that YAG:Pr^{3+} has a lower 4f5d band edge and achieves greater spectral overlap between the $^3P_0$→$^3H_4$ and $^1D_2$→4f5d transitions. Because the $^1D_2$ state has a longer lifetime than $^3P_0$,[90] the $^3P_0$,$^1D_2$→$^3H_4$,4f5d UC will be more efficient than $^3P_0$,$^3P_0$→$^3H_4$,4f5d UC (i.e., the primary mechanism in Y_2SiO_5 host), given a comparable spectral overlap.

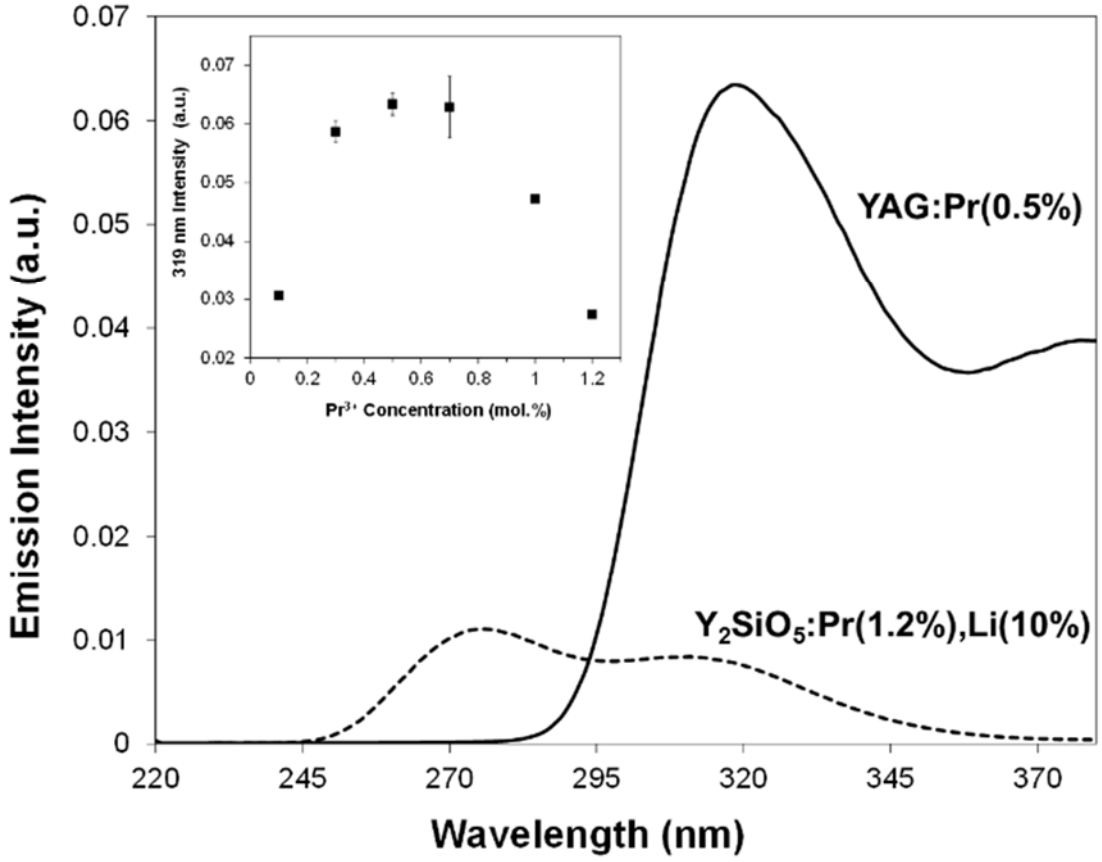

Figure 6.2: PLS comparing the UC emissions of YAG:Pr^{3+}(0.5) (solid line) and Y_2SiO_5:Pr^{3+}(1.2),Li^{+}(10) (dotted line). Inset depicts optimization of Pr^{3+} concentration in YAG, based on peak UV emission intensity (taken from 319 nm) under 447 nm laser excitation. Standard deviation is shown for median values only ([Pr^{3+}] = 0.3-0.7 mol.%).

Scanning electron microscopy images (see Fig. 6.3) show that the YAG:Pr^{3+} phosphor particles prepared using the Pechini sol-gel synthesis were spherical and subject to aggregation. The spherical particles ranged in size from 20 nm to 2 μm, and each consisted of smaller, nm-scale crystallites.

Figure 6.3: Scanning electron microscopy of annealed YAG:Pr^{3+} phosphors made using Pechini sol-gel synthesis.

An ultrasonic spray pyrolysis method was also used to make YAG:Pr^{3+}, but the upconverted emission of the prepared powders was significantly lower than the YAG synthesized using the sol-gel Pechini method. Still, the ability to produce spherical YAG:Pr^{3+} with controlled size and properties were of great interest to us, so we continued to pursue USP powders. Because these UVB-UVA emitting phosphors could potentially be used for TiO_2 sensitization, to photocatalytically degrade organic contaminants in water, we decided to experiment with porous materials. As mentioned in Chapter 5, the presence of open pores would provide a greater surface area upon which the photocatalysts and contaminants can adsorb and react. Inducing porosity could thus be a technique to enhance the photocatalytic activity of hybrid TiO_2/phosphor materials. To create pores, small polymer beads were added to the precursor solution for USP, and these were incorporated into the precursor spheres during the USP furnace reaction (silica beads are often used for this purpose, but were not suitable for this application due to its reactivity with yttrium). The polymer beads could be removed either by heat treatment or using a NaOH wash, leaving pores where the beads were originally. SEM of USP YAG:Pr^{3+} with and without a polystyrene (PS) additive are shown in Fig. 6.4. The dark circles in Fig. 6.4b are the pores left by the PS beads. Though the dispersion of pores amongst the USP particles were not homogeneous, the pores were a good size for the photocatalysis application and the spherical morphology and rigidity of the phosphor particles was maintained. Unfortunately, the UC emission from these porous YAG:Pr^{3+} particles was even weaker than the USP particles without PS; this was understandable due to the lower material density but was still a significant limitation for these materials. Given the possible advantages of spherical YAG:Pr^{3+}, particularly for controlled TiO_2 coating for visible-light

activated photocatalysis application, we feel that the optimization of UC for these porous, spherical YAG:Pr^{3+} would be worth pursuing. The method described above is recommended due to the ease of adjusting parameters (temperature, flow rate, precursor concentration) and reliably non-aggregated, spherical particles. That being said, sol-gel YAG:Pr^{3+} had significantly higher UC than USP products, and was used exclusively for the preliminary experiments herein.

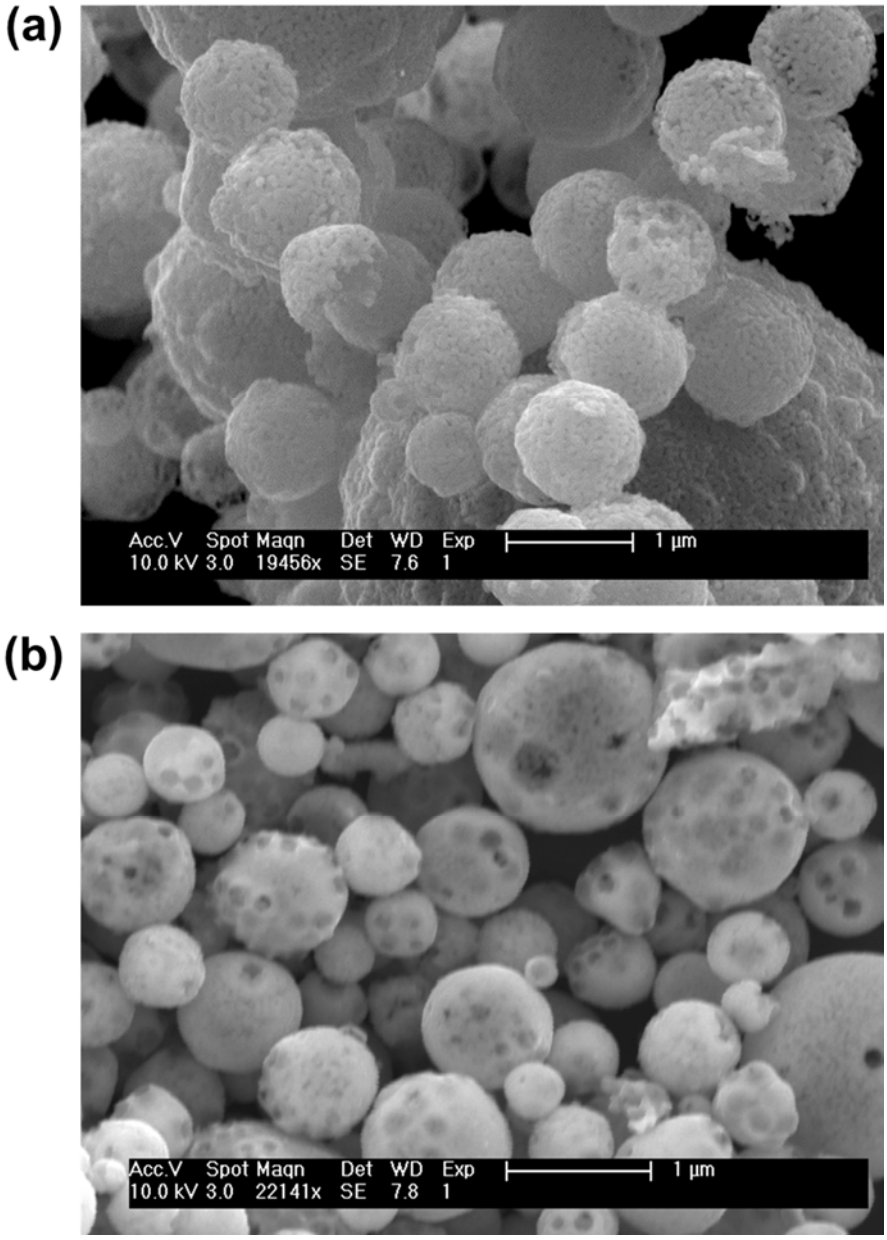

Figure 6.4: SEM images of (a) annealed YAG:Pr^{3+} from USP, and (b) annealed YAG:Pr^{3+} from USP with porosity from addition of polystyrene beads.

Photocatalytic activity. Given the high UVB-UVA emission of the YAG:Pr^{3+} phosphors and the absorption of these wavelengths by TiO_2, we expected even better results with UC-activated photocatalysis, compared to the Y_2SiO_5:Pr^{3+} materials in the previous chapter. Surprisingly, this was not the case, and YAG:Pr^{3+} phosphors performed quite poorly in comparison. The same photocatalytic activity experiments were conducted as in Chapter 5, wherein YAG:Pr^{3+}-P25 composite films were irradiated in solution by a blue LED, and the production of photoinduced conduction band electrons was measured by the reduction of POM. Both the as-prepared and platinized composite films failed to show any POM reduction.

Some insight as to why the YAG:Pr^{3+} phosphors were failing to excite TiO_2 could be seen when we switched to high power visible irradiation, in an attempt to amplify the UC response of the phosphors. After shining a laser onto YAG:Pr^{3+}-P25 samples, a brown-tinted spot became visible where the laser was hitting the sample. These spots were created consistently on YAG:Pr^{3+} samples but were never seen on Y_2SiO_5 Pr^{3+} samples, which were tested using the same laser intensity; nor did they appear when exciting YAG:Pr^{3+} without TiO_2. This brown coloring of YAG phosphors had actually been encountered earlier in this work, seen in "bad batches" (poor UC) while trying to determine the optimal synthesis for YAG:Pr^{3+}powders. Upon searching the literature for similar results, we found that the oxidized form of Pr^{3+}—Pr^{4+}—is known to appear brown. We had also seen strong evidence of the UV from the YAG:Pr^{3+} phosphors being absorbed by TiO_2 when exciting the mixtures during PLS, shown in Fig. 6.5, so the most likely explanation for the observed phenomena was the oxidation of Pr^{3+} by TiO_2–catalyzed ROS. Since Pr^{4+} does not have the optical properties of Pr^{3+}, oxidized material can no longer participate in UC. Thus, it

appears that our phosphor is being rendered inactive as soon as the reactions begin. To confirm these speculations, we have sent our samples to a lab that will perform x-ray photoelectron spectroscopy (XPS) to identify the oxidation state of the praseodymium ions in the tinted and non-tinted samples.

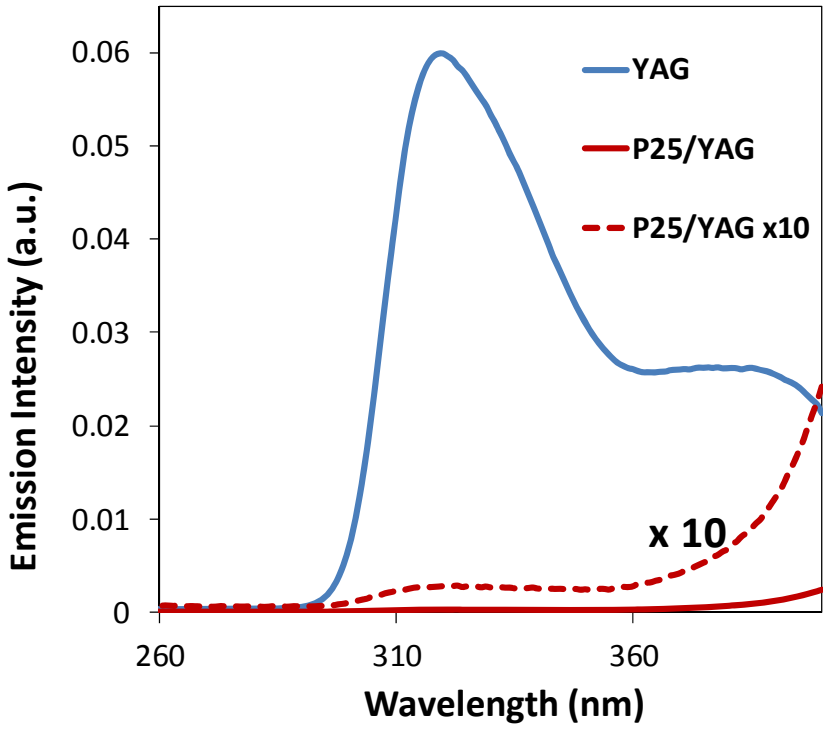

Figure 6.5: Evidence of UV sensitization of P25 by YAG:Pr^{3+} phosphors, using PLS (λ_{ex} = 447 nm). The emission from P25/YAG mixtures (red) has been magnified (red dotted) to show the resemblance to YAG emission. We observe higher emission for P25/YAG closer to 400 nm, corresponding to where the absorption by P25 is known to drop off.

To understand why oxidation would occur with YAG but not (or, to an unnoticeable extent) in Y_2SiO_5, we can also consider the radii of the two ions, particularly in relation to Y^{3+} (104 pm). The Y^{3+} sites in YAG have octahedral coordination, whereas the Y^{3+} in X2-Y_2SiO_5 are either 6- or 7-coordinated. The more flexible structure of X2-Y_2SiO_5 means the larger Pr^{3+} ions (113 pm) can occupy these sites more comfortably, while the more rigid YAG coordination may prefer the smaller Pr^{4+} ion (99 pm). If the Pr^{3+} is confirmed to undergo oxidation to Pr^{4+}, the oxidation could be potentially be prevented by shielding the phosphors from contact with ROS. This can be achieved by coating the phosphors with a transparent layer of SiO_2 or undoped YAG prior to mixing with TiO_2. Since this coating should not be thick enough to noticeably inhibit UVC transmission to the photocatalysts, we would expect this to result in higher activation of TiO_2 under visible light compared to Y_2SiO_5:Pr^{3+} systems.

Finally, to determine if the UC could be further improved using our prior modifications for Y_2SiO_5:Pr^{3+}, YAG:Pr^{3+} powders were used to make ceramics. The powders exhibited good pressability and produced solid, dense ceramics, similarly to Y_2SiO_5:Pr^{3+}. Additionally, the ceramics achieved significantly higher UC emission intensities, as shown in Fig. 6.6. Emission from YAG:Pr^{3+} ceramics were nearly 5x higher than powdered YAG samples and a remarkable 12x higher than Y_2SiO_5:Pr^{3+} ceramics. These results indicate both successful enhancement by ceramic formation and also the possible utility of YAG:Pr^{3+} surfaces for higher performance applications. TiO_2-coated ceramics, for example, might achieve even higher photocatalytic efficiencies than what is possible for composite films. Alternatively, YAG ceramics could be used as a fixed UVB

source under solar irradiation that could excite an aqueous TiO_2 slurry, for potentially enhanced degradation kinetics.

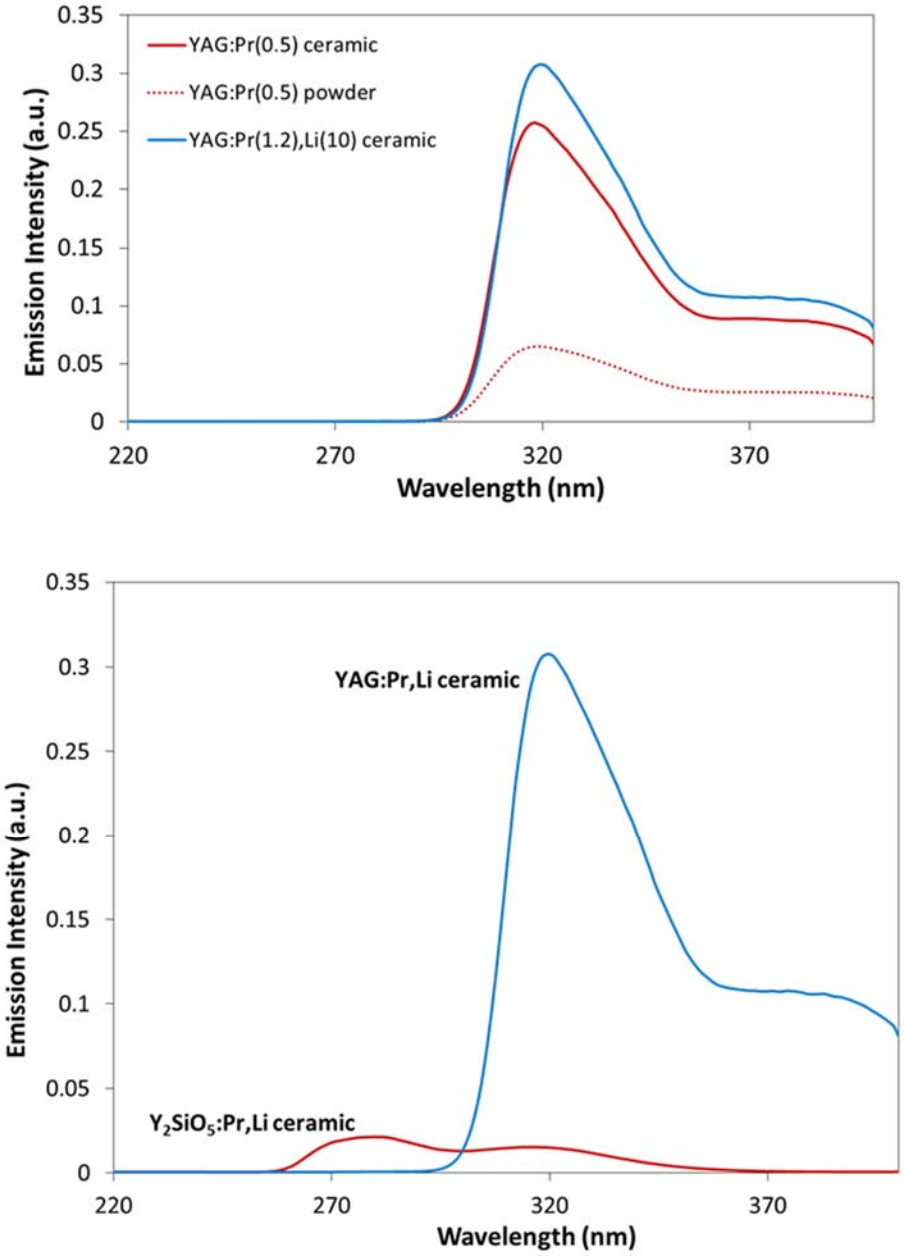

Figure 6.6: Photoluminescence spectroscopy showing upconverted emission from YAG:Pr^{3+} ceramics, compared to YAG:Pr^{3+} powders (top) and previously optimized Y_2SiO_5:Pr^{3+} ceramics (bottom). The addition of Li^+, which reduced UC emission for YAG powders, resulted in slightly greater UC efficiency for YAG ceramics.

6.4. Conclusion

YAG:Pr^{3+} phosphors exhibiting visible-to-UVB/UVA upconversion were synthesized using a sol-gel method. The Pr^{3+} doping concentration was optimized to 0.5 mol.%, resulting in the highest intensity UVB emission under 447 nm laser excitation. The significant increase (~20x) in upconverted UV emission compared to previously optimized Y_2SiO_5:Pr^{3+} phosphors suggested that these materials could likewise emit a measurable amount of UV under low-intensity excitation, such as solar irradiation, and could be even more effective for applications utilizing UVB or UVA. The main proposed application was for the phosphors to be used as sensitizers for TiO_2, to achieve photocatalysis under visible light. Preliminary experiments with P25, however, were unsuccessful, and the possibility of Pr^{3+} being oxidized to Pr^{4+} was postulated. Still, these issues might be easily fixed, and the synthetic methods described here could be further optimized to result in YAG:Pr^{3+} phosphors with better UV luminescence and photocatalyst activation. Finally, ceramic YAG:Pr^{3+} were seen to have significantly enhanced UC emission compared to powders, introducing the possibility of more efficient, YAG:Pr^{3+}-surface based technologies.

CHAPTER 7

CONCLUSION

7.1. Implications

This body of work describes a range of materials engineering techniques designed to enhance the efficiency of visible-to-UV upconversion (UC) phosphors, particularly under low-intensity excitation. The data presented demonstrate how alterations made to a bulk, polycrystalline material can affect the optical behavior of the luminescent ions, for better or for worse. By tailoring these strategies to suit individual phosphor types, significant advances were made in the development of UC antimicrobial surfaces, as well as UC/TiO_2 hybrid materials for visible-light activated photocatalysis.

Upconversion ceramics for antimicrobial surfaces. Upconversion ceramics exhibited significantly greater strength, durability, and UVC luminescence compared to first-generation phosphor powders and dip-coated films. Most importantly, forming ceramics from $Y_2SiO_5:Pr^{3+}$ was shown to improve their antimicrobial activity under low-power visible light, attributed to increased material density and crystallite size. The 3-fold enhancement in inactivation rate for *B. subtilis* spores was an encouraging benchmark for these materials, which remain the only upconversion phosphors designed for antimicrobial surfaces. Moreover, it is likely that the bulk ceramic form of other UC materials would exhibit similar optical and structural improvements. Indeed we have already seen this with $YAG:Pr^{3+}$ ceramics, which had significantly improved UVB emission compared to sol-gel $YAG:Pr^{3+}$ powders.

Dye sensitized upconversion. Dye sensitization is anticipated to be an important tool to achieve faster microbial inactivation on $Y_2SiO_5:Pr^{3+}$ surfaces. Our results suggest that FRET is occurring between coumarin 4 dye and the $Y_2SiO_5:Pr^{3+}$ phosphors, despite what would appear to be poor spectral overlap between the two. By finding a dye with optimal spectral overlap with our phosphors, we believe a significant enhancement (on the order of a magnitude or more) in UC efficiency can be achieved. Because weak absorption coefficients limit all inorganic phosphors, the dye sensitization methods described herein should also be applicable to other phosphors. This technique is expected to be especially helpful for applications that involve small phosphor particles and low-intensity excitation.

Upconversion phosphor-sensitized photocatalysis. This work was the first known account of photocatalyst sensitization by visible-to-UV UC phosphors. We saw that upconverted UVC from $Y_2SiO_5:Pr^{3+}$ could be effectively absorbed by TiO_2 and used for photocatalysis, as measured under low-power, visible light excitation. Visible-to-UVC phosphors can also be used to sensitize semiconductors with higher band gaps than TiO_2, which could result in even higher efficiency photocatalysis. This technology has potential implications for solar-powered water, wastewater, surface, and air treatment.

Development of visible-to-UVB/UVA phosphors. Since certain environmental applications can utilize lower UV energies, like the photocatalyst sensitization described above, Pr^{3+} was doped into a new host material that enabled UVB-UVA emission. The optimized $YAG:Pr^{3+}$ phosphors exhibited an estimated 20 times the emitted UV intensity of $Y_2SiO_5:Pr^{3+}$ powders, and the reasons for the higher intensity, red-shifted emission are explained. The unique challenges of implementing $YAG:Pr^{3+}$ for UC-sensitized photocatalysis are analyzed, but solutions were also proposed. $YAG:Pr^{3+}$ is yet another

material whose UC properties have not been thoroughly characterized and has not been studied for low-power irradiation applications. This work introduces YAG:Pr^{3+} as a potentially useful material for solar-activated environmental treatment.

7.2. Outlook

During the duration of this work alone, advances in upconversion materials research—including enhancements in upconversion efficiency, new host crystals and applications, and improved tools to analyze optical phenomena—have been reported at an accelerated rate. The enhancements in ultraviolet UC achieved here for Y_2SiO_5:Pr^{3+} ceramics and YAG:Pr^{3+} phosphors are indicative of both the potential for improvement and the ever-growing number of strategies that can be used to make better materials. As new modification techniques and new UC materials are introduced, we can more easily imagine inorganic UC phosphors achieving more practically relevant conversion efficiencies.

It is our hope that this work can build upon the growing interest in UC materials and especially encourage the exploitation of UC materials for environmental applications. Our group's focus on low-intensity excitation is specifically designed to assess the effectiveness of UC materials under solar or ambient indoor lighting, in an attempt to create sustainable, light-powered technologies. While this focus has presented a unique set of experimental challenges, including the sometimes frustrating efficiencies measured in this work, each of these challenges have contributed to our understanding of these materials and therefore brings us closer to real world application.

7.3. Future work

Since proofs of concept for UC antimicrobial surfaces and UC-activated photocatalysis have been successfully presented, suggestions for future work focus on the enhancement of UC efficiency for both $Y_2SiO_5:Pr^{3+}$ and $YAG:Pr^{3+}$. These include:

- The development of USP (i.e. spherical) particles with improved UC efficiency could potentially lead to further enhancements in UC. Many of the enhancement techniques described in literature, including dye-sensitized UC, utilized spherical particles to precisely control reactions, e.g. the degree of surface functionalization or dye loading. Even slight changes in dye concentration and separation distance between dye and phosphors were seen to affect whether or not an enhancement was achieved. The poor UC efficiency of USP particles limited their usefulness here, but better UC would be expected with more practice; the precursor concentration, furnace temperature, flow rate, and annealing schemes could all be optimized.
- The determination of a dye with optimal spectral overlap for sensitization of both phosphors; possible candidates include Sytox Blue and BO-PRO-1. The absorbance of the dyes should be measured after coating using diffuse reflectance spectroscopy. Once the appropriate dye is identified, the optimal concentration of dye on the phosphor surface should be experimentally determined. Spherical phosphors from ultrasonic spray pyrolysis are recommended for dye sensitization experiments.

- New host crystals with lower phonon cutoff energies should be explored for Pr^{3+}-doping, to see if higher UV emission (whether UVC, UVB, or UVA) can be achieved. Recently we developed a Sr_3AlO_4F host doped with Pr^{3+}, Na^+, and Ca^{2+} that had ~50% greater emission than YAG:Pr^{3+}(0.5), peaking at 316 nm. Though more synthetically complex, this and other host materials deserve further attention.
- Efficiency of UC-activated photocatalysis could also be increased choosing a photocatalyst with greater redox potential than TiO_2, such as ZnO, SnO_2, or a mixture of wider band gap photocatalysts. These could absorb the UVC emitted by Y_2SiO_5:Pr^{3+}. In addition to POM reduction to measure photoactivity, electron spin paramagnetic resonance (EPR) can be used *in situ* to measure the production of superoxide and hydroxyl radicals.
- For further application of visible-to-UVB YAG:Pr^{3+} phosphors, possible Pr^{3+} oxidation by ROS must be addressed. Strategies to eliminate this effect, such as core-shell coating of SiO_2 or undoped YAG, could lead to successful activation of photocatalysts under visible light.
- The enhanced UC exhibited by ceramics can be combined with the photocatalysis application. For example, photocatalyst-coated phosphor surfaces (e.g. upconversion ceramics dip-coated with TiO_2) could have higher photocatalytic efficiency than powder P25/phosphor films. TiO_2-coated or loaded ceramics could even be designed for self-cleaning surfaces that have the combined visible-light antimicrobial activity of the UCPs and photocatalyst.

Finally, an important requirement for applying these materials to environmental technologies is to test these materials under the actual conditions of target application, e.g. outdoors, in simulated sunlight, or under ambient indoor lighting (e.g. for hospital settings). The effects of light intensity fluctuations, temperature, extraneous debris or aqueous media, and/or broadband excitation could all provide useful insight when designing the UC materials for these applications.

APPENDIX A

PHOTOLUMINESCENCE SPECTROSCOPY SETUP AND COMPONENTS

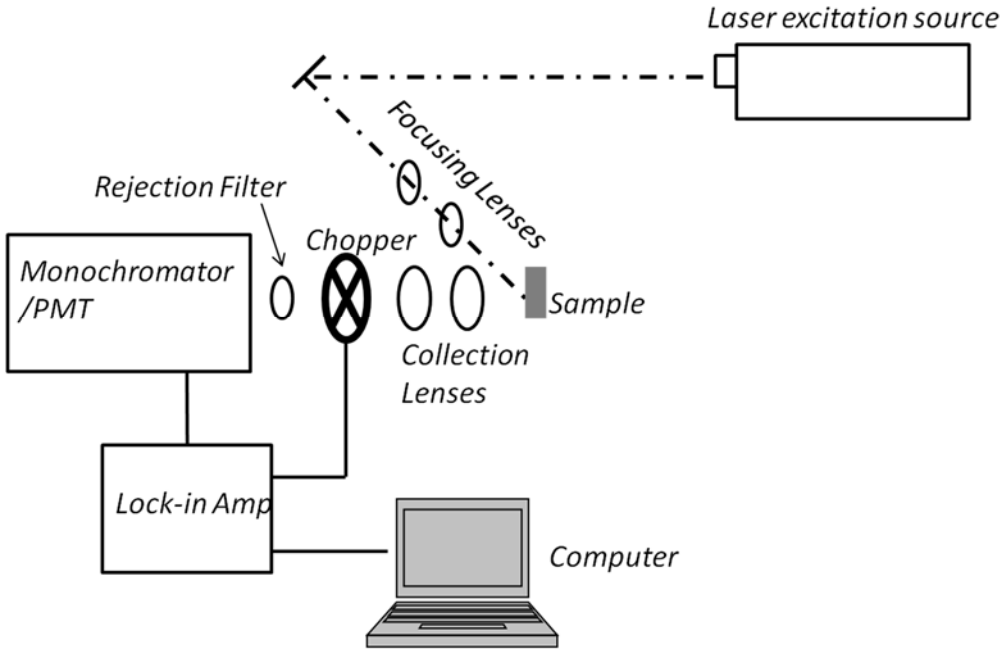

Schematic of photoluminescence spectroscopy (PLS) system setup used in this work.

COMPONENT	MAKE/MODEL	SPECIFICATIONS
Violet 447 nm DPSS Laser	OEM Lasers / BL-447-00100-CWM-SD-05-LED-0	Maximum Power (447±5 nm): 100 mW Beam Diameter: 5 mm Beam Divergence: 1.5 mrad
Concave Mirror	Newport/05DC200ER.1	Focal Length: 100 mm
Mirror Mounts	Newport/U50-A	
Plano-Convex Lens	Edmund Optics/48-664	Focal Length: 200 mm
UV-Antireflective Plano-convex Lens	Edmund Optics/48030	Focal Length: 30 mm
400 nm Shortpass	Edmund Optics/49816	
Monochromator	Newport Oriel/Cornerstone 260 1/4M	Dual Grating RS-232 Communication
Monochromator Grating	Newport Oriel /SP74161-4976	MgF2 Overcoat for high UV throughput Lines/mm: 2400 Blaze: 250 nm
Photomultiplier Tube	Newport Oriel/77348	Wavelength Range: 160-900 nm Maximum Voltage: 1000 V
PMT Housing	Newport Oriel/70107	Side-on configuration

PMT Power Supply	Newport Oriel/70705	
Current Preamplifier	Newport Oriel/70710	Amplification (V/A): 10^6 - 10^9
Digital Lock-in Amplifier	Newport Oriel/70100 Merlin Radiometer	Single Channel RS-232 Communication
Chopper Head	Newport Oriel/75154	
Chopper Wheel	Newport Oriel/75162	2-Aperture Maximum Chop: 160 Hz
Data Acquisition Software	Newport Oriel/TRACQ Basic	

APPENDIX B

CALCULATION OF UPCONVERSION EFFICIENCY FOR $Y_2SiO_5:Pr^{3+}$ CERAMICS

Values and equations used to solve for UC efficiency

- Blue light power density (measured by radiometer)

  1650 $\mu W/cm^2$

- Approx. UV dose (emitted by sample; calculated using linear portion of dose response curve depicted in Fig. 3.10)

  $y = -0.26\ x + 1.32$ (y = log inactivation, solve for x)

  Units: $mW \cdot s/cm^2$

- Time

  691,200 s (8 d)

- Avg. UV intensity

  $[(\text{UV dose})*1000/(\text{Time})]*10^{-6}$

  Units: $\mu W/cm^2$

- Hypothetical 100% UC (assume 2-photon UC)

  $1650/2 = 825\ \mu W/cm^2$

- UC efficiency (ratio of upward emission intensity to incident excitation)

  (Avg. UV intensity)/(Hypothetical 100% UC)

Calculated efficiencies for $Y_2SiO_5:Pr^{3+}$ antimicrobial materials

$Y_2SiO_5:Pr^{3+},Li^+$ ceramics (2013)[32]	0.0019%
Y_2SiO_5: Pr^{3+},Gd^{3+},Li^+, thin films (2011)[1]	0.0010%
Y_2SiO_5: Pr^{3+},Li^+ thin films (2011)[1]	0.0009%
Y_2SiO_5: Pr^{3+},Li^+ thin films (2013)[32]	0.0012%

Samples measured in 2013 were inoculated using a different procedure than the samples measured in 2011 (samples were inoculated using spore-laden spray, rather than by dropping spore solution onto each sample and air-drying) and irradiated with slightly lower intensity visible light (both used fluorescent bulbs). Though it was assumed that the differences in experimental setup would not cause significant variations in results, dose-response curves obtained by irradiating spores with a germicidal UVC lamp suggested that lower intensity UVC may actually be more effective at prolonged inactivation of spores (see discussion in Chapter 3). This could also explain the slightly higher calculated efficiency for 2013 $Y_2SiO_5:Pr^{3+},Li^+$ dip-coated films, which were prepared in the same manner as the films from 2011. That being said, slight disparities between different experiments are not surprising given the varying nature of microbial populations.

APPENDIX C

ADDITIONAL MEASUREMENTS OF VISIBLE LIGHT PHOTOCATALYTIC ACTIVITY FOR UCP-TiO_2 SYSTEMS

Coumarin Degradation

Coumarin ($C_9H_6O_2$) was used as a molecular probe for photogenerated radical species. As depicted below, coumarin is known to readily react with hydroxyl radicals (·OH) (one of the primary reactive oxygen species formed during TiO_2 photocatalysis, as shown in Chapter 5, Fig. 5.1) to form a fluorescent hydroxylated byproduct, 7-hydroxycoumarin.[92] It has thus been shown that the photoactivity of TiO_2 can be quantitatively assessed by irradiating TiO_2 in aqueous coumarin solution and measuring the fluorescence of the solution over time, using a spectrofluorophotometer.[92, 93] A fluorescence peak at 452 nm is characteristic of 7-hydroxycoumarin, indicating coumarin degradation by photocatalytic production of ·OH.

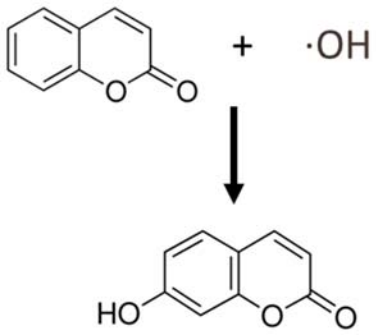

Coumarin reacts with photogenerated ·OH (top) to produce a fluorescent byproduct, 7-hydroxycoumarin (bottom).

The following fluorescence spectra show representative coumarin degradation results for a range of sample configurations. Both $Y_2SiO_5:Pr^{3+}$ and YAG:Pr^{3+} phosphors were tested using this method, coated or mixed with TiO_2 or Aeroxide P25, and synthesized using sol-gel decomposition (Chapter 3) or ultrasonic spray pyrolysis (USP; Chapter 4). The materials were tested as powders dispersed in solution and also as stationary composite films (similar to the films used in POM reduction experiments, described in Chapter 5). TiO_2 dip-coating was also tested using optimized $Y_2SiO_5:Pr^{3+}$ ceramics (synthesized as in Chapter 3). Some samples were irradiated with an LED array and others with a violet DPSS laser (447 nm), as labeled. Controls were also tested.

Unfortunately, certain inconsistencies in coumarin testing coupled with slow reaction times for our materials forced us to find an alternative method of photoactivity measurement, so coumarin testing was abandoned in favor of polyoxometalate (POM) reduction. One of the inconsistencies shown here was the sharp peak at 347 nm exhibited by some samples, each to a different extent; this peak width extended unknowingly far into the range of the target fluorescence peak (452 nm), thus complicating analysis. The 347 nm peak appeared to be caused by nano-sized particles remaining in test solutions during measurement, despite centrifugation and filtration of the samples through 0.22 μm syringe filters (the smallest available size); the samples which exhibited 347 nm peaks had even higher intensity peaks before filtration, indicating the role of suspended material. The most likely cause was thought to be scattering of excitation light, though this peak is slightly lower in energy than the excitation wavelength (332 nm). Samples were also sometimes variable during the measurement itself, i.e. measuring the same sample at a later time could affect the measured intensity. It is possible that there was enough residual TiO_2 in the

solutions (especially for samples containing P25, which is known to consist of many nanoscale particles < 0.22 μm) to absorb the spectrofluorophotometer excitation light (332 nm) and degrade coumarin *during* the measurement. Indeed, testing the same filtered sample from a mixture of P25 and coumarin over a period of 6 minutes resulted in a gradually increasing 452 nm fluorescence peak, confirming this suspicion, A repeat of the same experiment showed a peak almost immediately (within 10 seconds of placing the vial in the sample holder), though notably not as high as the 452 nm peaks for $Y_2SiO_5:Pr^{3+}$ samples shown here.

All samples were tested using aqueous coumarin solution (1 mg/mL H_2O), spectrofluorophotometer λ_{ex} = 332 nm.

Sample: (5:1) TiO_2-coated $Y_2SiO_5:Pr^{3+}$(1.2%),Li^+(10%) powder stirred in coumarin solution, lit from above.
Excitation: Blue LED (λ= 450 nm), with UV filter (cutoff 425 nm)

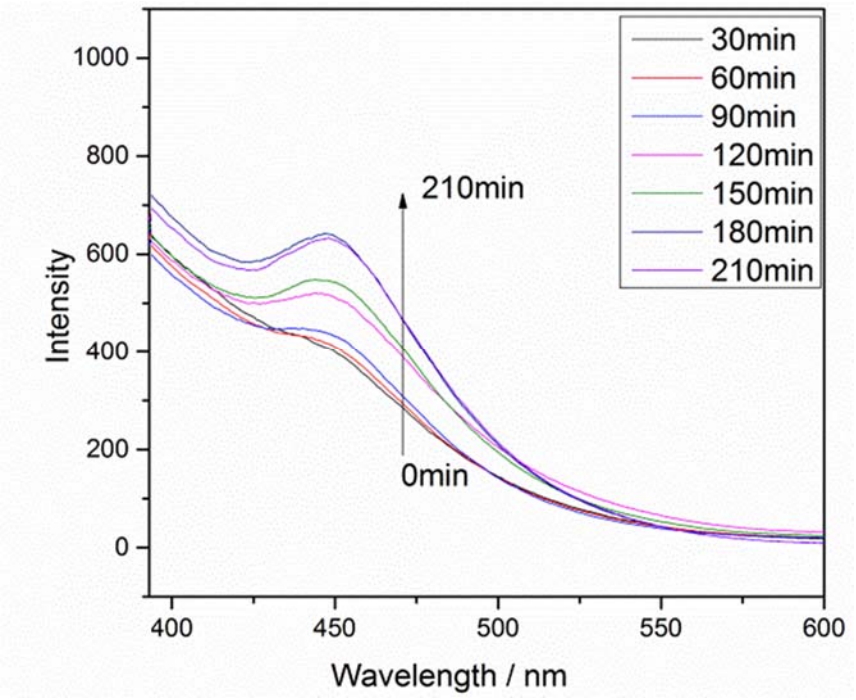

Samples: Powders dispersed in coumarin solution and allowed to settle in petri dish; irradiated without stirring. Lit from below. "YSO" = $Y_2SiO_5:Pr^{3+}(1.2\%),Li^{+}(10\%)$, "YAG" = $Y_3Al_5O_{12}:Pr^{3+}(0.5\%)$.
Excitation: Blue LED (λ= 450 nm), with UV filter (cutoff 425 nm)
Irradiation time: 16 h

*Note: Spetrofluorophotometer lamp overheated since the experiments shown above, and all subsequent measurements were much noisier (bumpy), despite changing the lamp.

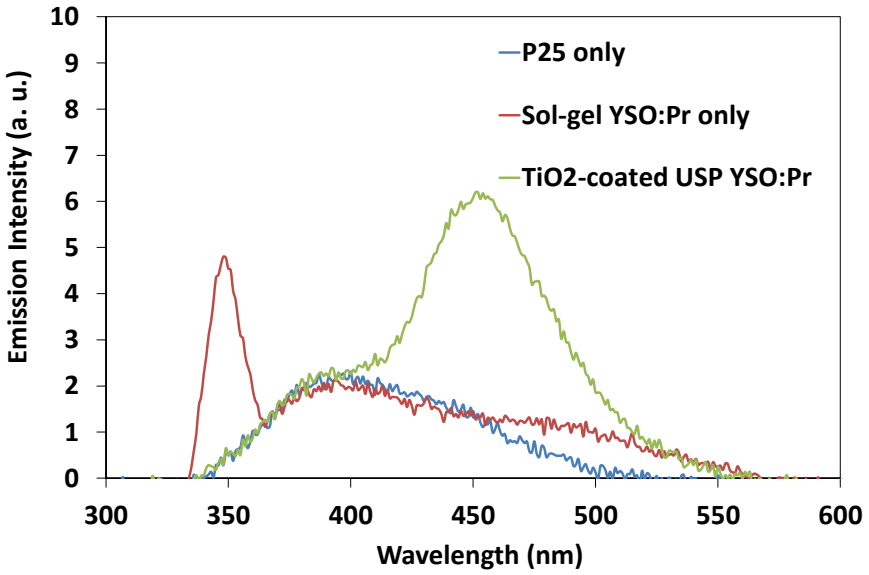

(Same specs as above)

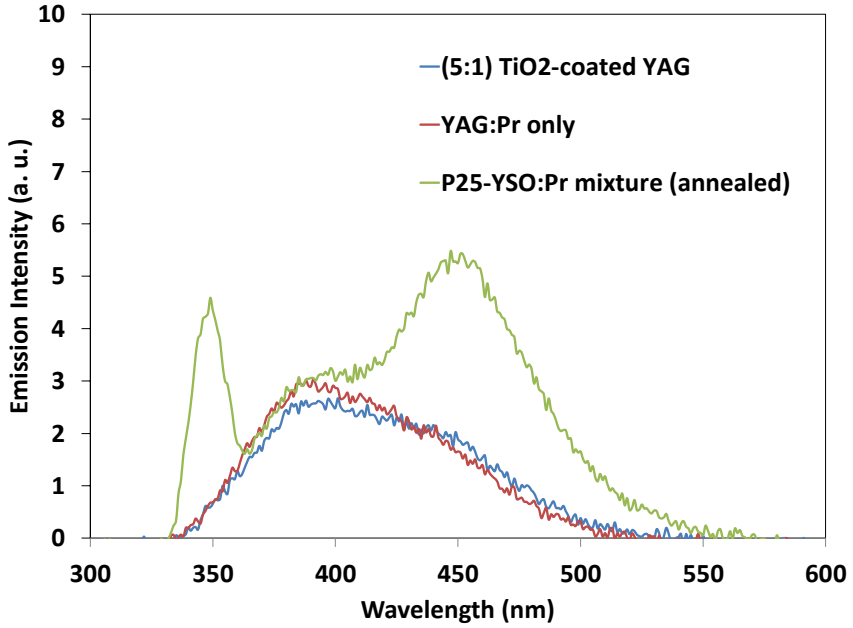

Samples: TiO_2-coated powder was dispersed in coumarin solution and allowed to settle in petri dish; irradiated without stirring. Thin films were prepared using cascade method (Chapter 5) and 2 of each were placed in petri dishes and covered with coumarin solution. Lit from below. "YSO" = $Y_2SiO_5:Pr^{3+}$(1.2%),Li^+(10%), "YAG" = $Y_3Al_5O_{12}:Pr^{3+}$(0.5%).
Excitation: Blue LED (λ= 450 nm), with UV filter (cutoff 425 nm)
Irradiation time: 16 h

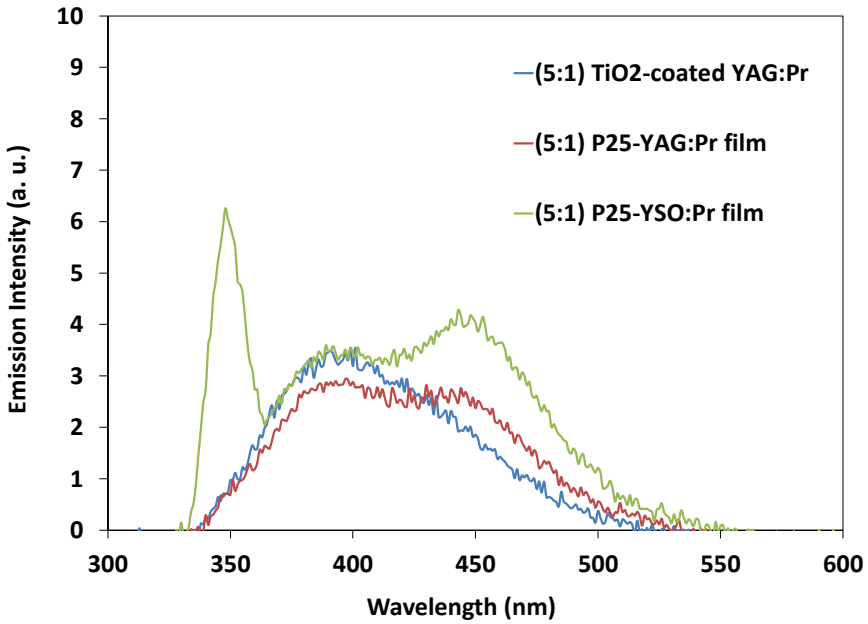

Samples: Ceramic was coated with TiO_2 using method above; first plot shows confirmation of TiO_2 activity under UVA from blacklight irradiation, second plot shows laser irradiation of a new sample, suspended in a stirring coumarin solution. "YSO" $=Y_2SiO_5:Pr^{3+}(1.2\%),Li^{+}(10\%)$.
Excitation: Violet DPSS laser (λ= 447 nm), power = 100 mW (intensity ≈ 30 W/cm^2, based on estimate of beam size at sample)

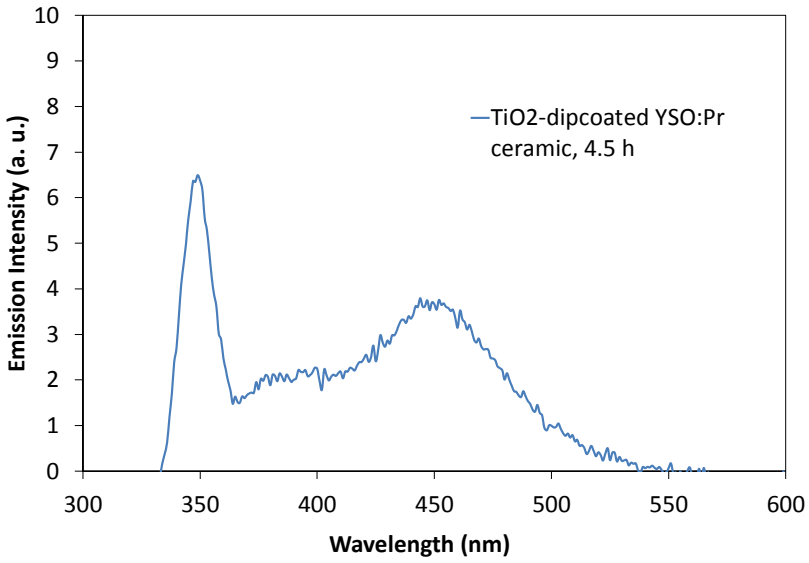

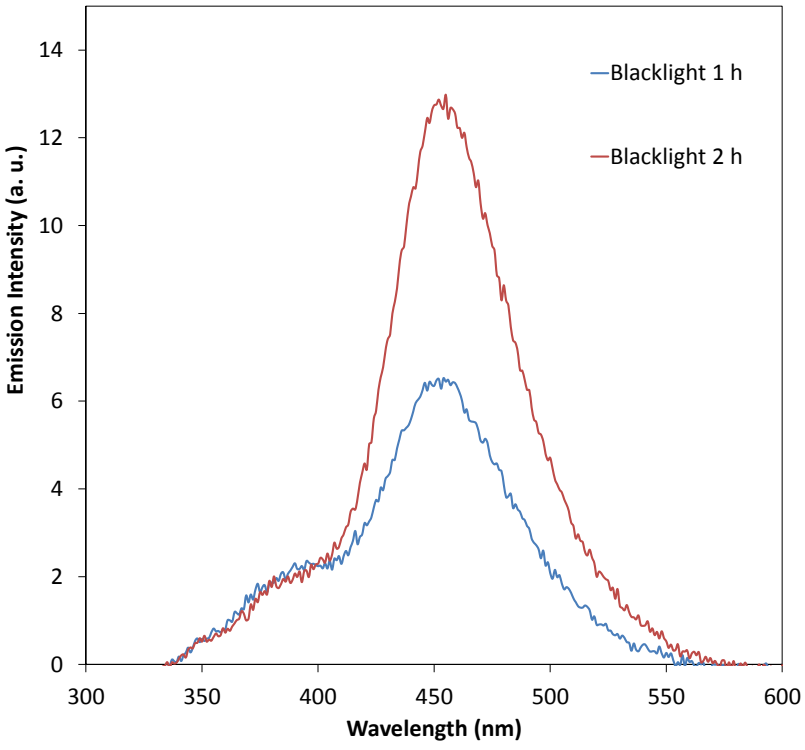

Samples: (5:1) TiO_2-coated YAG:Pr^{3+} film was tested under UVA (same sample measured at 45 min and then at 90 min) to confirm TiO_2 activity; compared to P25 dispersed in coumarin and control sample of coumarin alone. "YAG" = $Y_3Al_5O_{12}$:Pr^{3+}(0.5%).
Excitation: Blacklight (λ = 365 nm)

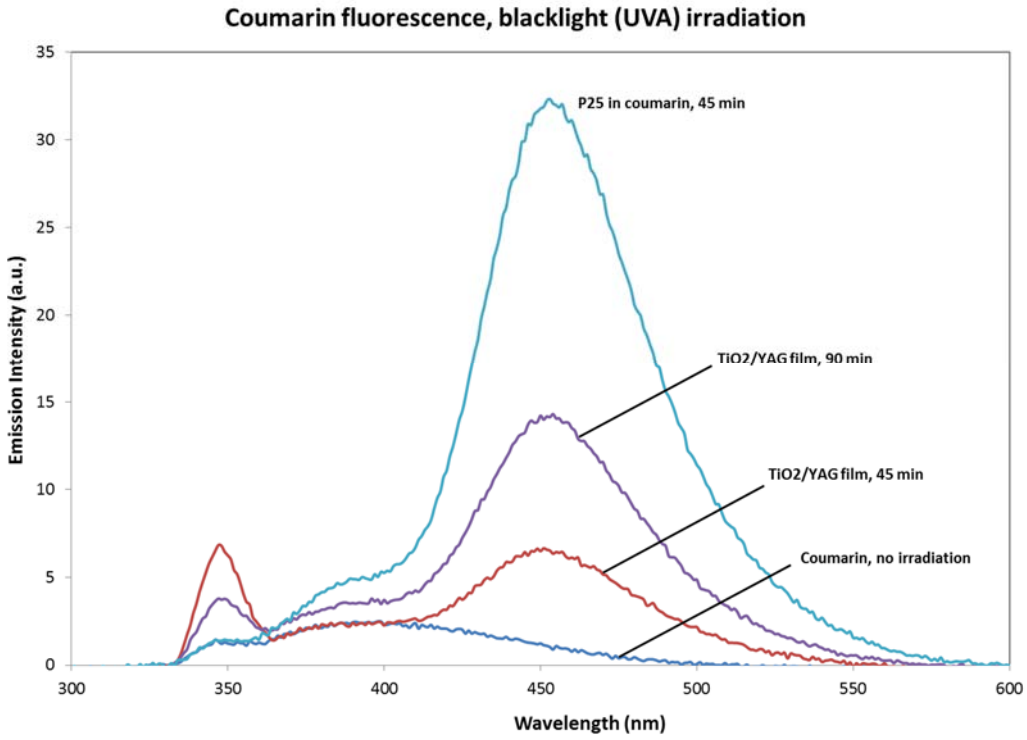

Sample: P25-$Y_2SiO_5:Pr^{3+}$ composite film on 12mm round cover glass, tested first without Pt (left), then a new sample loaded with Pt (right)
Light source: Blue LED (λ= 450 nm), with UV filter (cutoff 425 nm)
Pt loading: By photo-deposition for 15 min (with 0.33g/L H_2PtCl_6 in Methanol/DW mixture (33%))

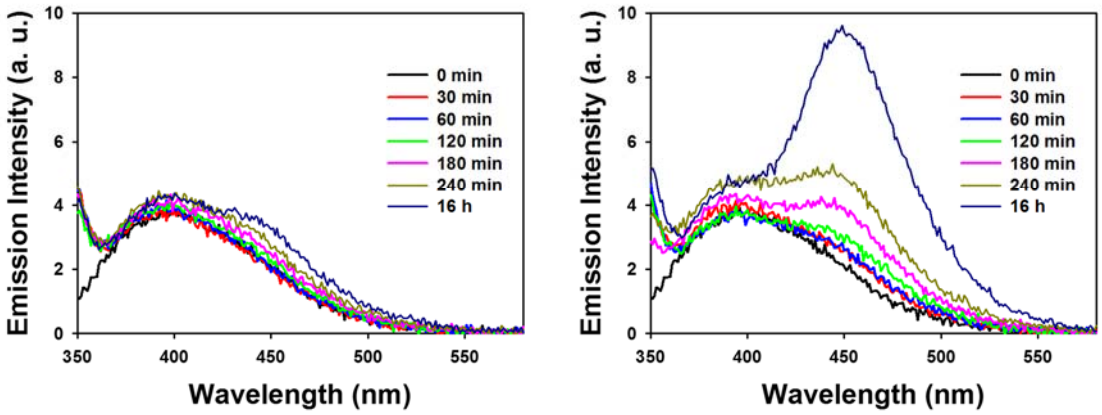

Sample: P25:YAG:Pr^{3+} composite film on 20 X 18 mm^2 rectangular cover glass, tested first without Pt (left), then a new sample loaded with Pt (right)
Light source: Blue LED (λ= 450 nm), with UV filter (cutoff 425 nm)
Pt loading: By photo-deposition for 15 min (with 0.33g/L H_2PtCl_6 in Methanol/DW mixture (33%))

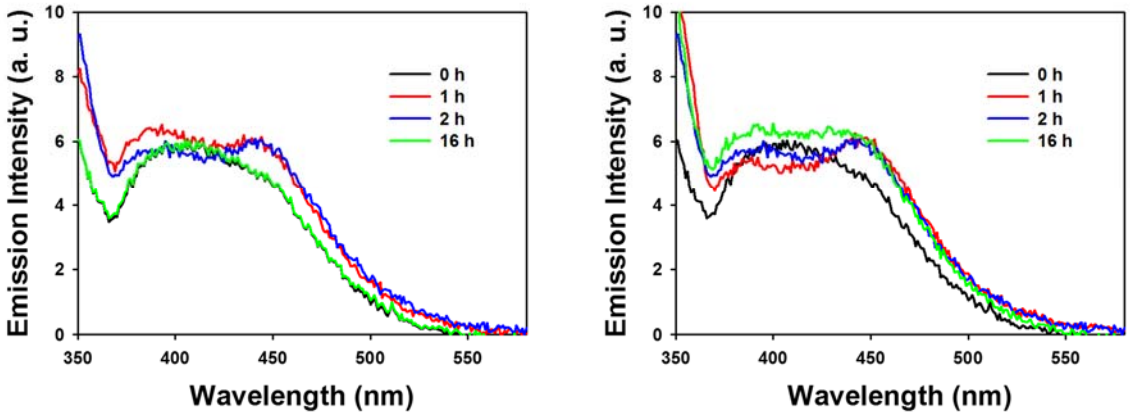

Coumarin Degradation Summary

From these results, we begin to see evidence of visible-light-induced photocatalysis with TiO_2-Y_2SiO_5:Pr^{3+} composite materials. While one P25-YAG:Pr^{3+} film had a small fluorescence peak after 16 h, all other YAG:Pr^{3+} samples appeared to have no activity (this is discussed further in Chapter 6). Blacklight controls confirm the presence and activity of TiO_2 on all coated and composite samples but also highlight the much higher activity of P25 in coumarin under UVA for just 45 minutes, compared to P25 mixed with phosphors under visible light for 4+ hours. Though the amount of material and surface area of the experiments did vary (some tests were done with dispersed powder whereas some on thin films, for example), they nonetheless offer a general comparison of candidate materials. This data was also used when deciding which materials to test with POM reduction (Chapter 5); as such, YAG materials were not used.

REFERENCES

1. Cates, E. L.; Cho, M.; Kim, J.-H., Converting visible light into UVC: Microbial inactivation by Pr^{3+}-activated upconversion materials. *Environmental Science & Technology* **2011,** *45*, (8), 3680-3686.
2. Auzel, F., Upconversion and anti-Stokes processes with f and d ions in solids. *Chem. Rev.* **2004,** *104*, (1), 139-174.
3. Wang, F.; Liu, X., Recent advances in the chemistry of lanthanide-doped upconversion nanocrystals. *Chemical Society Reviews* **2009,** *38*, (4), 976-989.
4. Kim, W. J.; Nyk, M.; Prasad, P. N., Color-coded multilayer photopatterned microstructures using lanthanide (III) ion co-doped $NaYF_4$ nanoparticles with upconversion luminescence for possible applications in security. *Nanotechnology* **2009,** *20*, (18), 185301.
5. Zou, W.; Visser, C.; Maduro, J. A.; Pshenichnikov, M. S.; Hummelen, J. C., Broadband dye-sensitized upconversion of near-infrared light. *Nat Photon* **2012,** *6*, (8), 560-564.
6. Fischer, S.; Goldschmidt, J. C.; Loper, P.; Bauer, G. H.; Bruggemann, R.; Kramer, K.; Biner, D.; Hermle, M.; Glunz, S. W., Enhancement of silicon solar cell efficiency by upconversion: Optical and electrical characterization. *Journal of Applied Physics 108*, (4), 044912-11.
7. Shan, G.-B.; Demopoulos, G. P., Near-infrared sunlight harvesting in dye-sensitized solar cells via the insertion of an upconverter-TiO_2 nanocomposite layer. *Advanced Materials* **2010,** *22*, (39), 4373-4377.
8. Trupke, T.; Green, M. A.; Wurfel, P., Improving solar cell efficiencies by up-conversion of sub-band-gap light. *Journal of Applied Physics* **2002,** *92*, (7), 4117-4122.
9. Cates, E. L.; Chinnapongse, S. L.; Kim, J.-H.; Kim, J.-H., Engineering light: Advances in wavelength conversion materials for energy and environmental technologies. *Environmental Science & Technology* **2012,** *46*, (22), 12316-12328.
10. Liu, Q.; Sun, Y.; Yang, T.; Feng, W.; Li, C.; Li, F., Sub-10 nm hexagonal lanthanide-doped $NaLuF_4$ upconversion nanocrystals for sensitive bioimaging in vivo. *Journal of the American Chemical Society* **2011,** *133*, (43), 17122-17125.
11. Chatterjee, D. K.; Rufaihah, A. J.; Zhang, Y., Upconversion fluorescence imaging of cells and small animals using lanthanide doped nanocrystals. *Biomaterials* **2008,** *29*, (7), 937-943.
12. Zhang, P.; Steelant, W.; Kumar, M.; Scholfield, M., Versatile photosensitizers for photodynamic therapy at infrared excitation. *J. Am. Chem. Soc.* **2007,** *129*, (15), 4526-4527.
13. Qian, H. S.; Guo, H. C.; Ho, P. C.-L.; Mahendran, R.; Zhang, Y., Mesoporous-silica-coated up-conversion fluorescent nanoparticles for photodynamic therapy. *Small* **2009,** *5*, (20), 2285-2290.
14. Islangulov, R. R.; Castellano, F. N., Photochemical Upconversion: Anthracene Dimerization Sensitized to Visible Light by a RuII Chromophore. *Angewandte Chemie International Edition* **2006,** *45*, (36), 5957-5959.
15. Singh-Rachford, T. N.; Castellano, F. N., Photon upconversion based on sensitized triplet–triplet annihilation. *Coordination Chemistry Reviews* **2010,** *254*, (21–22), 2560-2573.
16. Ropp, R. C., *Luminescence and the Solid State*. Second ed.; Elsevier: Amsterdam, The Netherlands, 2004.
17. The Top Ten Causes of Death. http://www.who.int/mediacentre/factsheets/fs310/en/index.html
18. Graves, N., Economics of preventing hospital infection. *Emerg Infect Dis* **2004**.

19. Page, K.; Wilson, M.; Parkin, I. P., Antimicrobial surfaces and their potential in reducing the role of the inanimate environment in the incidence of hospital-acquired infections. *Journal of Materials Chemistry* **2009,** *19*, (23), 3819-3831.
20. Weber, D. J.; Rutala, W. A.; Miller, M. B.; Huslage, K.; Sickbert-Bennett, E., Role of hospital surfaces in the transmission of emerging health care-associated pathogens: Norovirus, Clostridium difficile, and Acinetobacter species. *American Journal of Infection Control* **2010,** *38*, (5, Supplement), S25-S33.
21. Grass, G.; Rensing, C.; Solioz, M., Metallic Copper as an Antimicrobial Surface. *Applied and Environmental Microbiology* **2011,** *77*, (5), 1541-1547.
22. Ferreira, L.; Zumbuehl, A., Non-leaching surfaces capable of killing microorganisms on contact. *Journal of Materials Chemistry* **2009,** *19*, (42), 7796-7806.
23. Sommer, B. M., A.; Solarte, Y.; Salas, L.; Dierolf, C.; Valiente, C.; Mora, D.; Rechsteiner, R.; Setter, P.; Wirojanagud, W.; Ajarmeh, H.; Al-Hassan, A.; Wegelin, M., SODIS--an emerging water treatment process. *J Water SRT* **1997,** *46*, (3), 127-137.
24. Sommer, R.; Cabaj, A.; Hirschmann, G.; Haider, T., Disinfection of Drinking Water by UV Irradiation: Basic Principles - Specific Requirements - International Implementations. *Ozone: Science & Engineering* **2008,** *30*, (1), 43-48.
25. Kolesov, R.; Xia, K.; Reuter, R.; Stöhr, R.; Zappe, A.; Meijer, J.; Hemmer, P. R.; Wrachtrup, J., Optical detection of a single rare-earth ion in a crystal. *Nat Commun* **2012,** *3*, 1029.
26. Page, R. H.; Schaffers, K. I.; Waide, P. A.; Tassano, J. B.; Payne, S. A.; Krupke, W. F.; Bischel, W. K., Upconversion-pumped luminescence efficiency of rare-earth-doped hosts sensitized with trivalent ytterbium. *J. Opt. Soc. Am. B* **1998,** *15*, (3), 996-1008.
27. de Wild, J.; Rath, J. K.; Meijerink, A.; van Sark, W. G. J. H. M.; Schropp, R. E. I., Enhanced near-infrared response of a-Si:H solar cells with β-NaYF4:Yb3+ (18%), Er3+ (2%) upconversion phosphors. *Solar Energy Materials and Solar Cells* **2010,** *94*, (12), 2395-2398.
28. Cates, E. L.; Kim, J.-H., Upconversion under polychromatic excitation: $Y_2SiO_5:Pr^{3+}$, Li^+ converts violet, cyan, green, and yellow light into UVC. *Optical Materials* **2013,** *35*, (12), 2347-2351.
29. Cates, E. L.; Wilkinson, A. P.; Kim, J.-H., Delineating mechanisms of upconversion enhancement by Li^+ codoping in $Y_2SiO_5:Pr^{3+}$. *The Journal of Physical Chemistry C* **2012,** *116*, (23), 12772-12778.
30. Sun, C. L.; Li, J. F.; Hu, C. H.; Jiang, H. M.; Jiang, Z. K., Ultraviolet upconversion in $Pr^{3+}:Y_2SiO_5$ crystal by Ar^+ laser (488 nm) excitation. *The European Physical Journal D - Atomic, Molecular, Optical and Plasma Physics* **2006,** *39*, (2), 303-306.
31. Hu, C.; Sun, C.; Li, J.; Li, Z.; Zhang, H.; Jiang, Z., Visible-to-ultraviolet upconversion in $Pr^{3+}:Y_2SiO_5$ crystals. *Chemical Physics* **2006,** *325*, (2-3), 563-566.
32. Cates, S. L.; Cates, E. L.; Cho, M.; Kim, J.-H., Synthesis and Characterization of Visible-to-UVC Upconversion Antimicrobial Ceramics. *Environmental Science & Technology* **2014,** *48*, (4), 2290-2297.
33. Qin, F.; Zheng, Y.; Yu, Y.; Zheng, C.; Tayebi, P. S.; Zhang, Z.; Cao, W., Ultraviolet upconversion luminescence of Gd^{3+} from Ho^{3+} and Gd^{3+} codoped oxide ceramic induced by 532-nm CW laser excitation. *Optics Communications* **2011,** *284*, (12), 3114-3117.
34. Zhang, J.; Wang, S.; An, L.; Liu, M.; Chen, L., Infrared to visible upconversion luminescence in $Er^{3+}:Y_2O_3$ transparent ceramics. *Journal of Luminescence 122-123*, (0), 8-10.
35. Sun, Z.; Zhou, Y.; Li, M., Effect of $LiYO_2$ on the synthesis and pressureless sintering of Y_2SiO_5. *Journal of Materials Research* **2008,** *23*, (03), 732-736.

36. Cho, M.; Chung, H.; Yoon, J., Disinfection of water containing natural organic matter by using ozone-initiated radical reactions. *Applied and Environmental Microbiology* **2003,** *69*, (4), 2284-2291.
37. ASTM G173–03 standard tables of reference solar spectral irradiances: Direct normal and hemispherical on a 37° tilted surface. In *Annual Book of ASTM Standards*, American Society for Testing and Materials: Philadelphia, PA, USA, Vol. 14.04.
38. Wang, J.; Tian, S.; Li, G.; Liao, F.; Jing, X., Preparation and X-ray characterization of low-temperature phases of R_2SiO_5 (R = rare earth elements). *Materials Research Bulletin* **2001,** *36*, (10), 1855-1861.
39. Rahaman, M. N., *Ceramic Processing and Sintering*. Taylor & Francis: 2003.
40. Langsrud, S.; Sidhu, M. S.; Heir, E.; Holck, A. L., Bacterial disinfectant resistance--a challenge for the food industry. *International Biodeterioration & Biodegradation* **2003,** *51*, (4), 283-290.
41. Landi, E.; Tampieri, A.; Celotti, G.; Sprio, S., Densification behaviour and mechanisms of synthetic hydroxyapatites. *Journal of the European Ceramic Society* **2000,** *20*, (14–15), 2377-2387.
42. Chen, R. Z.; Craik, S. A.; Bolton, J. R., Comparison of the action spectra and relative DNA absorbance spectra of microorganisms: Information important for the determination of germicidal fluence (UV dose) in an ultraviolet disinfection of water. *Water Research* **2009,** *43*, (20), 5087-5096.
43. De, G.; Qin, W.; Zhang, J.; Zhang, J.; Wang, Y.; Cao, C.; Cui, Y., Effect of OH^- on the upconversion luminescent efficiency of Y_2O_3:Yb^{3+}, Er^{3+} nanostructures. *Solid State Communications* **2006,** *137*, (9), 483-487.
44. Zhmurin, P. N.; Znamenskii, N. V.; Yukina, T. G.; Malyukin, Y. V., Strong quenching of Y_2SiO_5:Pr^{3+} nanocrystal luminescence by praseodymium nonuniform distribution. *physica status solidi (b)* **2007,** *244*, (9), 3325-3332.
45. Malyukin, Y. V.; Masalov, A. A.; Zhmurin, P. N.; Znamenskii, N. V.; Petrenko, E. A.; Yukina, T. G., Two mechanisms of $^1D_2$ fluorescence quenching of Pr^{3+}-doped Y_2SiO_5 crystal. *physica status solidi (b)* **2003,** *240*, (3), 655-662.
46. Hegarty, J.; Huber, D. L.; Yen, W. M., Fluorescence quenching by cross relaxation in LaF_3:Pr^{3+}. *Physical Review B* **1982,** *25*, (9), 5638-5645.
47. Seminko, V. V.; Masalov, A. A.; Boyko, Y. I.; Malyukin, Y. V., Strong segregation of doped ions in Y_2SiO_5:Pr^{3+} nanocrystals. *Journal of Luminescence* **2012,** *132*, (9), 2443-2446.
48. Chen, G.; Liu, H.; Liang, H.; Somesfalean, G.; Zhang, Z., Upconversion emission enhancement in Yb^{3+}/Er^{3+}-codoped Y_2O_3 nanocrystals by tridoping with Li+ ions. *The Journal of Physical Chemistry C* **2008,** *112*, (31), 12030-12036.
49. Yang, M.; Sui, Y.; Wang, S.; Wang, X.; Sheng, Y.; Zhang, Z.; Lü, T.; Liu, W., Enhancement of upconversion emission in $Y_3Al_5O_{12}$:Er^{3+} induced by Li^+ doping at interstitial sites. *Chemical Physics Letters* **2010,** *492*, (1–3), 40-43.
50. Lin, J.; Su, Q.; Zhang, H.; Wang, S., Crystal structure dependence of the luminescence of rare earth ions (Ce^{3+}, Tb^{3+}, Sm^{3+}) in Y_2SiO_5. *Materials Research Bulletin* **1996,** *31*, (2), 189-196.
51. Chang, J. C.; Ossoff, S. F.; Lobe, D. C.; Dorfman, M. H.; Dumais, C. M.; Qualls, R. G.; Johnson, J. D., UV inactivation of pathogenic and indicator microorganisms. *Applied and Environmental Microbiology* **1985,** *49*, (6), 1361-1365.
52. Mamane-Gravetz, H.; Linden, K. G., Relationship between physiochemical properties, aggregation and UV inactivation of isolated indigenous spores in water. *Journal of Applied Microbiology* **2005,** *98*, (2), 351-363.

53. Coohill, T. P.; Sagripanti, J.-L., Overview of the inactivation by 254 nm ultraviolet radiation of bacteria with particular relevance to biodefense. *Photochemistry and Photobiology* **2008,** *84*, (5), 1084-1090.
54. Rose, L. J.; O'Connell, H., UV light inactivation of bacterial biothreat agents. *Applied and Environmental Microbiology* **2009,** *75*, (9), 2987-2990.
55. Nicholson, W. L.; Galeano, B., UV resistance of Bacillus anthracis spores revisited: Validation of Bacillus subtilis spores as UV surrogates for spores of B. anthracis Sterne. *Applied and Environmental Microbiology* **2003,** *69*, (2), 1327-1330.
56. Sun, Z.; Wang, J.; Li, M.; Zhou, Y., Mechanical properties and damage tolerance of Y_2SiO_5. *Journal of the European Ceramic Society* **2008,** *28*, (15), 2895-2901.
57. Aparicio, M.; Durán, A., Yttrium silicate coatings for oxidation protection of carbon–silicon carbide composites. *Journal of the American Ceramic Society* **2000,** *83*, (6), 1351-1355.
58. Mechnich, P., Y_2SiO_5 coatings fabricated by RF magnetron sputtering. *Surface and Coatings Technology*, (0).
59. Shannon, R., Revised effective ionic radii and systematic studies of interatomic distances in halides and chalcogenides. *Acta Crystallographica Section A* **1976,** *32*, (5), 751-767.
60. Kang, Y. C.; Lenggoro, I. W.; Okuyama, K.; Park, S. B., Luminescence Characteristics of Y 2SiO5 : Tb Phosphor Particles Directly Prepared by the Spray Pyrolysis Method. *Journal of The Electrochemical Society* **1999,** *146*, (3), 1227-1230.
61. Xie, X.; Liu, X., Photonics: Upconversion goes broadband. *Nat Mater* **2012,** *11*, (10), 842-843.
62. Dipole-dipole interactions and energy transfer. http://research.physics.berkeley.edu/yildiz/Teaching/PHYS250/SupplementaryFiles/Dipole%20dipole%20interactions%20and%20FRET.pdf
63. Förster, T., Zwischenmolekulare Energiewanderung und Fluoreszenz. *Annalen der Physik* **1948,** *437*, (1-2), 55-75.
64. Fujishima, A.; Rao, T. N.; Tryk, D. A., Titanium dioxide photocatalysis. *Journal of Photochemistry and Photobiology C: Photochemistry Reviews* **2000,** *1*, (1), 1-21.
65. Hashimoto, K.; Irie, H.; Fujishima, A., TiO 2 Photocatalysis: A Historical Overview and Future Prospects. *Japanese Journal of Applied Physics* **2005,** *44*, (12R), 8269.
66. López, R.; Gómez, R., Band-gap energy estimation from diffuse reflectance measurements on sol–gel and commercial TiO2: a comparative study. *Journal of Sol-Gel Science and Technology* **2012,** *61*, (1), 1-7.
67. Levinson, R.; Akbari, H.; Berdahl, P., Measuring solar reflectance—Part I: Defining a metric that accurately predicts solar heat gain. *Solar Energy* **2010,** *84*, (9), 1717-1744.
68. Qin, W.; Zhang, D.; Zhao, D.; Wang, L.; Zheng, K., Near-infrared photocatalysis based on YF3 : Yb3+,Tm3+/TiO2 core/shell nanoparticles. *Chemical Communications* **2010,** *46*, (13).
69. Wang, J.; Zhang, G.; Zhang, Z.; Zhang, X.; Zhao, G.; Wen, F.; Pan, Z.; Li, Y.; Zhang, P.; Kang, P., Investigation on photocatalytic degradation of ethyl violet dyestuff using visible light in the presence of ordinary rutile TiO2 catalyst doped with upconversion luminescence agent. *Water Research* **2006,** *40*, (11), 2143-2150.
70. Feng, G.; Liu, S.; Xiu, Z.; Zhang, Y.; Yu, J.; Chen, Y.; Wang, P.; Yu, X., Visible Light Photocatalytic Activities of TiO2 Nanocrystals Doped with Upconversion Luminescence Agent. *The Journal of Physical Chemistry C* **2008,** *112*, (35), 13692-13699.
71. Yi Yang, 2 Guang-Zhi Xia,1 Cheng Liu,1 Jin-Hua Zhang,1,2 and Lian-Jun Wang1,2, Effect of Li(I) and TiO2 on the Upconversion Luminance of Pr:Y2SiO5 and Its Photodegradation on Nitrobenzene Wastewater. *Journal of Chemistry* **2014,** *2015*.

72. Yi Yang, 2 Cheng Liu,1 Ping Mao,1,2 and Lian-Jun Wang1,2, Upconversion Luminescence and Photodegradation Performances of Pr Doped Y2SiO5 Nanomaterials. *Journal of Nanomaterials* **2013,** *2013*.
73. Hwang, S.; Lee, M. C.; Choi, W., Highly enhanced photocatalytic oxidation of CO on titania deposited with Pt nanoparticles: kinetics and mechanism. *Applied Catalysis B: Environmental* **2003,** *46*, (1), 49-63.
74. Bae, E.; Choi, W., Highly Enhanced Photoreductive Degradation of Perchlorinated Compounds on Dye-Sensitized Metal/TiO2 under Visible Light. *Environmental Science & Technology* **2003,** *37*, (1), 147-152.
75. Zhang, T. R.; Feng, W.; Fu, Y. Q.; Lu, R.; Bao, C. Y.; Zhang, X. T.; Zhao, B.; Sun, C. Q.; Li, T. J.; Zhao, Y. Y.; Yao, J. N., Self-assembled organic-inorganic composite superlattice thin films incorporating photo- and electro-chemically active phosphomolybdate anion. *Journal of Materials Chemistry* **2002,** *12*, (5), 1453-1458.
76. Bang, J.; Didenko, Y.; Helmich, R.; Suslick, K., Nanostructured materials through ultrasonic spray pyrolysis. *Material Matters* **2012,** *7*, (2).
77. Cho, J. S.; Jung, K. Y.; Chan Kang, Y., Two-step spray-drying synthesis of dense and highly luminescent YAG:Ce3+ phosphor powders with spherical shape. *RSC Advances* **2015,** *5*, (11), 8345-8350.
78. Kim, H.-i.; Kim, J.; Kim, W.; Choi, W., Enhanced Photocatalytic and Photoelectrochemical Activity in the Ternary Hybrid of CdS/TiO2/WO3 through the Cascadal Electron Transfer. *The Journal of Physical Chemistry C* **2011,** *115*, (19), 9797-9805.
79. Xu, M.; Li, Y.; Li, W.; Sun, C.; Wu, L., Structure, photochromic, and electrochemical properties of dioctadecylamine/H3PMo12O40 Langmuir–Blodgett film. *Journal of Colloid and Interface Science* **2007,** *315*, (2), 753-760.
80. Lee, J.; Kim, J.; Choi, W., Oxidation on Zerovalent Iron Promoted by Polyoxometalate as an Electron Shuttle. *Environmental Science & Technology* **2007,** *41*, (9), 3335-3340.
81. Kaminskii, A. A.; Bagayev, S. N.; Ueda, K.; Dong, J.; Eichler, H. J., New passively Q-switched LD-pumped self-Raman laser with single-step cascade SE → SRS wavelength conversion on the base of monoclinic Nd3+:Y2SiO5 crystal. *Laser Physics Letters* **2010,** *7*, (4), 270-279.
82. Laroche, M.; Braud, A.; Girard, S.; Doualan, J. L.; Moncorge, R.; Thuau, M.; Merkle, L. D., Spectroscopic investigations of the 4?5d energy levels of Pr3+ in fluoride crystals by excited-state absorption and two-step excitation measurements. *J. Opt. Soc. Am. B* **1999,** *16*, (12), 2269-2277.
83. Le Masson, N. J. M.; Vink, A. P.; Dorenbos, P.; Bos, A. J. J.; VanEijk, C. W. E.; Chaminade, J. P., Ce3+ and Pr3+5d-energy levels in the (pseudo) perovskites KMgF3 and NaMgF3. *Journal of Luminescence* **2003,** *101*, (3), 175-183.
84. Qin, G.; Lu, J.; Bisson, J. F.; Feng, Y.; Ueda, K.-i.; Yagi, H.; Yanagitani, T., Upconversion luminescence of Er3+ in highly transparent YAG ceramics. *Solid State Communications* **2004,** *132*, (2), 103-106.
85. Gruber, J. B.; Hills, M. E.; MacFarlane, R. M.; Morrison, C. A.; Turner, G. A., Symmetry, selection rules, and energy levels of Pr3+:Y3Al5O12. *Chemical Physics* **1989,** *134*, (2–3), 241-257.
86. Vaqueiro, P.; Arturo Lopez-quintela, M., Synthesis of yttrium aluminium garnet by the citrate gel process. *Journal of Materials Chemistry* **1998,** *8*, (1), 161-163.
87. Malta, O. L.; Antic-Fidancev, E.; Lemaitre-Blaise, M.; Dexpert-Ghys, J.; Piriou, B., Up-conversion in YAG:Pr3+: Evidence for a stepwise photon absorption process. *Chemical Physics Letters* **1986,** *129*, (6), 557-561.
88. Anker, D. S.; Merkle, L. D., Ion–ion upconversion excitation of the 4f5d configuration in Pr:Y3Al5O12 Experiments and Förster theory-based rate equation model. *Journal of Applied Physics* **1999,** *86*, (6), 2933-2940.

89. Özen, G.; Forte, O.; Di Bartolo, B., Downconversion and upconversion dynamics in Pr-doped Y3Al5O12 crystals. *Journal of Applied Physics* **2005,** *97*, (1), -.
90. Hassanzadeh-Tabrizi, S. A., Synthesis and luminescence properties of YAG:Ce nanopowder prepared by the Pechini method. *Advanced Powder Technology* **2012,** *23*, (3), 324-327.
91. Koshiishi, I.; Imanari, T., Study of the coloured substances in molybdenum blue using high-performance liquid chromatography. *Journal of Chromatography A* **1986,** *358*, (0), 195-200.
92. Ishibashi, K. I.; Fujishima, A.; Watanabe, T.; Hashimoto, K., Detection of active oxidative species in TiO2 photocatalysis using the fluorescence technique. *Electrochemistry Communications* **2000,** *2*, (3), 207-210.
93. Louit, G.; Hanedanian, M.; Taran, F.; Coffigny, H.; Renault, J. P.; Pin, S., Determination of hydroxyl rate constants by a high-throughput fluorimetric assay: towards a unified reactivity scale for antioxidants. *Analyst* **2009,** *134*, (2), 250-255.